Wind effects on the performance of solar collectors on roofs

Dimitrios I. Ladas

A Thesis

in

the Department

of

Building, Civil and Environmental Engineering

Presented in Partial Fulfillment of the Requirements

For the Degree of Master of Applied Science (Building Engineering) at

Concordia University

Montreal, Quebec, Canada

February 2014

CONCORDIA UNIVERSITY

School of Graduate Studies

This is to certify that the thesis prepared

By: *Dimitrios I. Ladas*

Entitled: *Wind Effects on the Performance of Solar Collectors on Roofs*

and submitted in partial fulfillment of the requirements for the degree of

M.A.Sc. Building Engineering

complies with the regulations of the University and meets the accepted standards with respect to originality and quality.

Signed by the final examining committee:

_____*Dr. R. Zmeureanu*_____Chair

_____*Dr. A. Athienitis*_____Examiner

_____*Dr. S. Williamson*_____Examiner

_____*Dr. T. Stathopoulos*_____Supervisor

Approved by _____

Chair of Department or Graduate Program Director

_____

Dean of Faculty

Date _____

ABSTRACT

Wind effects on the performance of solar collectors on roofs

by Dimitrios I. Ladas

Concordia University, 2014

A solar thermal collector collects heat by absorbing sunlight and transforms it into useful heat. Among the various parameters affecting the energy performance of solar collectors, convective heat losses depend greatly on the effect of wind and its cooling effects. Knowledge of wind heat transfer coefficient h_w, is required for the estimation of upward losses from the outer surface of flat-plate solar collectors. Furthermore, the wind speed at the location of the collector should be known.

A series of velocity measurements have been conducted at the Concordia University Building Aerodynamics Laboratory to assess the most appropriate location of a flat-plate solar collector on the roof of a building model. Wind velocity measurements were performed at nine different locations above the roof and for three different wind directions (0°, 45°, and 90°). The building was assumed to be on an open country simulated upstream terrain. A series of additional cases with the model surrounded by different adjacent structures of variable height were also tested. The forced convective heat transfer coefficient h_w was correlated

against the measured local wind speed V_{loc} and direction. The study found that local velocities on different roof locations can vary up to 62% for the same wind direction.

An analytical approach of a performance simulation model has been used to calculate the efficiency and the useful heat gain of a flat-plate single-glazed collector. The analysis has been conducted for hypothetical days with constant wind velocities and directions but also for an example actual day, typical of random wind velocity values. The wind impact on a flat-plate solar collector's performance characteristics when placed on different locations of the roof of a building model was assessed. It was estimated that for a typical sunny day, thermal energy gains can be 17% higher on windward than leeward locations.

ACKNOWLEDGEMENT

I must offer my profoundest gratitude to my thesis supervisor, Professor Ted Stathopoulos whose guidance and patience from the beginning of my studies was the greatest drive towards my graduation.

I am grateful to my good friend, roommate and colleague Costa Kapsis for his constant encouragement and help these last years.

I am also indebted to my friends and colleagues, Dr. Ioannis Zisis, Dr. Panagiota Karava, Dr. YuXiang Chen, Neetha Vasan, Mohamed Elsharawy, Mauricio Chavez and Daniel Candelario Suarez who found time in their already very busy schedule to always give me assistance and advice for my research work.

I would also like to acknowledge the support of all my friends and loved ones in Canada and Greece who provided me with continuous motivation and encouragement.

Finally, I would like to thank my family. My father John, my mother Ioanna and my sister Natalia. I am forever grateful. Their love, their continuous support and their understanding have been the greatest inspiration during this "marathon".

Στην Ναταλία, στην Ιωάννα, στον Γιάννη

Table of Contents

List of Figures

List of Tables

Nomenclature

A_c	Solar collector area (m^2)
C	Collector tilt factor (degrees)
C_b	Bond conductance (W/m*K)
C_p	Specific heat of water (kJ/kg*K)
C_t	Solar collector thickness (m)
D_p	Tube inside diameter (m)
e	Mean-plate temperature factor (K)
e_t	Edge-insulation thickness (m)

f	Wind factor (W/m^2K)
F_c	Fin efficiency factor
F'_c	Collector efficiency factor
F''_c	Collector flow factor
F_R	Collector heat removal factor
H	Model height (m)
h_w	Wind-induced convective heat-transfer coefficient (W/m^2K)
h_{fi}	Heat-transfer coefficient inside the tubes (W/m^2K)
I_T	Total incident solar radiation (W/m^2)
I_d	Diffuse solar radiation (W/m^2)
I_b	Beam solar radiation (W/m^2)

I_g	Ground-reflected solar radiation (W/m^2)
k_i	Insulation thermal conductivity (W/m*K)
k_p	Plate thermal conductivity (W/m*K)
L	[4 * plate area] / [plate circumference] (m)
L_t	Insulation thickness (m)
m_w	Water flow rate (kg/s)
N	Number of solar collector glass covers
Nu	Nusselt number
P	Solar collector perimeter (m)
Pr	Prandtl number
q_u	Useful thermal energy gain (W/m^2)

Re	Reynolds number
S	Solar radiation absorbed by the collector plate (W/m^2)
T_a	Ambient temperature (K)
T_i	Inlet fluid temperature (K)
T_{pm}	Mean-plate temperature (K)
U_b	Bottom-loss coefficient
U_e	Edge-loss coefficient
U_L	Overall collector loss coefficient
V_g	Mean wind speed (m/s), measured at the gradient height Z_g (or gradient velocity)
V_{loc}	Local velocity (m/s)
V_z	Mean wind speed (m/s), measured at the height Z

W_p	Tube spacing (m)
Z	Height (m)
Z_g	Gradient height (m)

Greek Letters

α	Alpha exponent (power law)
β_w	Collector tilt (degrees)
δ_p	Plate thickness (m)
ε_g	Glass emittance
ε_p	Plate emittance
η	Solar collector efficiency
$(\tau\alpha)$	Transmittance – absorptance product

Chapter 1 - INTRODUCTION

1.1. *Overview*

Throughout history humans have discovered ways to take various energy sources and use them to their advantage. From the simple task of burning wood to produce heat, to the immense amount of energy created by nuclear sources, the human race has travelled a long way into finding the most efficient and economical ways to produce energy.

During the second half of the 20th century though, the impacts of careless use of energy resources like fossil fuels (coal, gas, oil) and nuclear power appeared in the form of climate change, global warming, pollution and the greenhouse effect via ozone depletion. As a result, the necessity to develop sustainable sources that produce clean energy was created. Since then, renewable energy sources have gained enormous importance. Based on reports from the Renewable Policy Network for the 21st century (REN21, 2012) the 16.7% of the global energy consumption comes from renewable sources - Figure 1.1 shows the breakdown of the worldwide use of energy based on different sources -. Renewable sources vary from biomass, which is the most widespread today, to others less popular like biofuels and geothermal.

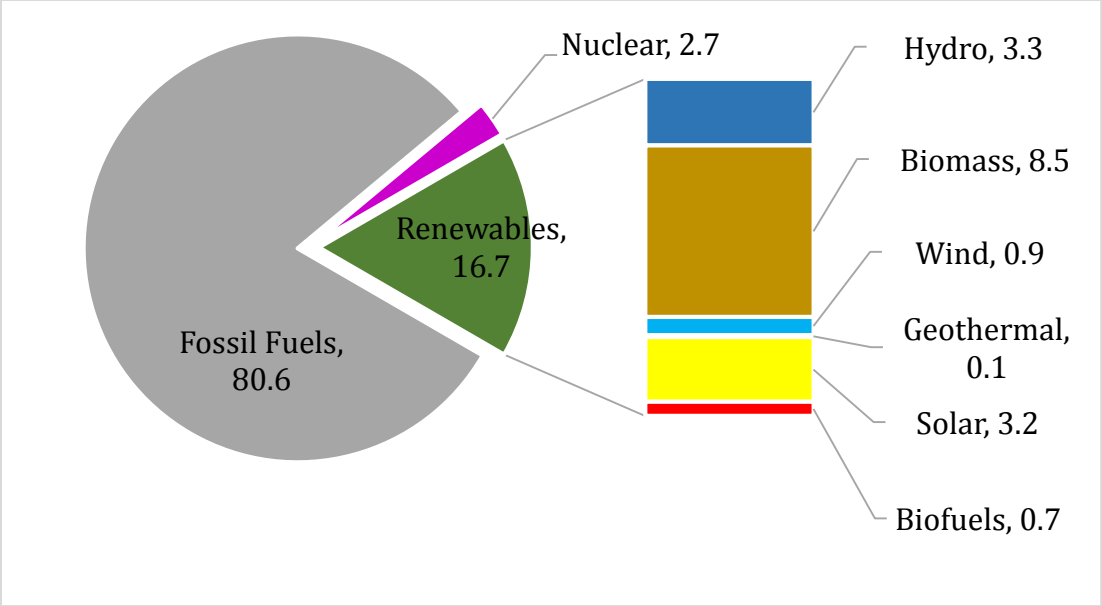

Figure 1.1: World energy consumption (%) (REN21, 2012)

In 2012, out of the total use of renewable sources, 20% is solar power (3.2% of total global energy use), whose usage has risen over the last years drastically. This can be attributed to the significant improvement of the collection and conversion of efficiencies, the decrease of the initial and maintenance costs and finally the increase of its reliability and applicability (NRCan, 2013).

Solar technologies have quickly evolved and become highly successful due to the parallel research that is conducted to enhance all characteristics of their performance; one of them is the study of the thermal effect of wind on solar collectors. Flat-plate solar-thermal collectors are highly susceptible to heat losses. One of the most significant heat loss paths is via forced convection from the upper cover plate of the collector to the wind which passes over the collector. Consequently, extensive wind studies and simulations are crucial so as to arrive

to the best possible design guidelines for this equipment. Figure 1.2 displays the typical structure of a single-glazed collector and shows the basic heat transfer processes that take place while the collector is hit by solar radiation.

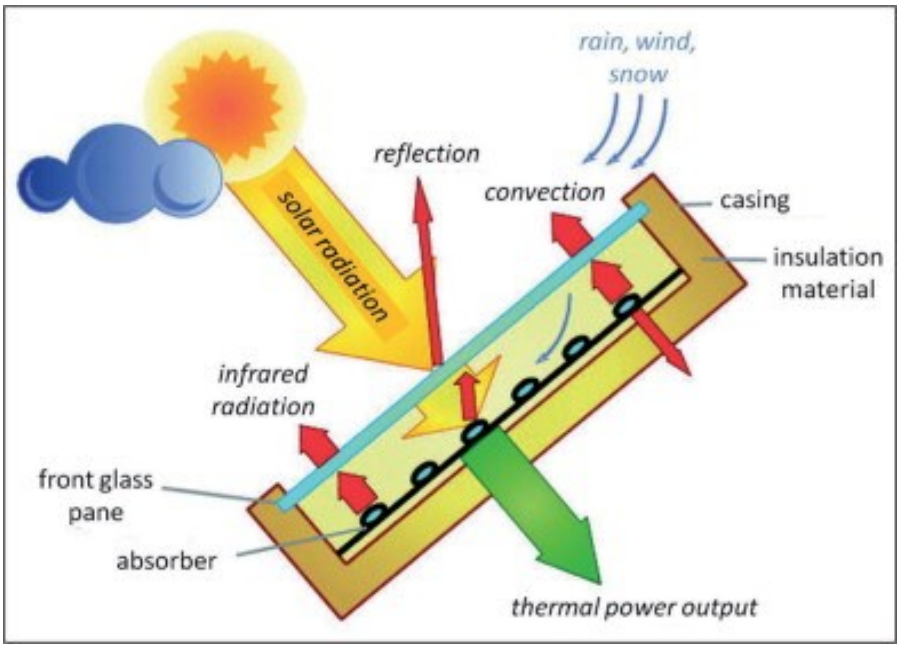

Figure 1.2: Typical structure of a single-glazed flat-plate solar collector (Rommel, et al., 2010)

1.2. *Flat-Plate Solar-Thermal Collectors*

Solar collectors mounted on roofs are a special category of heat exchangers that transform solar radiation energy to internal energy of the transport medium. In mechanical terms, there is a distinction between flat-plate collectors, evacuated

tube collectors, air collectors, unglazed collectors etc., yet the basic arrangement and main components of any collector are typically the same.

Flat-plate collectors are fixed to a position on roofs of buildings and other structures towards the equator and are typically facing south in the northern hemisphere and north in the southern hemisphere. Their tilt angle is ideally equal to the latitude of the location. The collector is the link between the sun and the hot water user.

1.2.1 Glazed flat-plate collectors

Glazed flat-plate collectors are composed of a dark absorber plate that absorbs most of the incoming solar radiation (a small portion is reflected), converts it into heat, and conducts this heat to a fluid (usually air, water, or different types of oils like anti-freezing glycol) flowing through the collector in tubes – Figure 1.3 depicts a single-glazed solar collector mounted on the roof of a residential building -. This is the most commonly used type of solar collector worldwide (Kalogirou, 2004).

Figure 1.3: Single glazed solar-thermal collector on top of a domestic roof (Jetson Green, 2011)

The solar energy collected is carried from the circulating fluid either straight to the domestic hot water, or to a storage tank, from which it can be drawn for use at a later time. The back side of the absorber plate and casing are well insulated to diminish conduction losses. The liquid tubes are either welded to the absorbing plate, or they are part of the absorber itself. The absorber and insulation of the collector are fitted in a box and sheltered on the top with one or two tempered glass covers (single or double glazed solar collectors) or even occasionally plastic material for protection. The transparent cover must have low reflection and protect the collector from the wind and moisture.

1.2.2 Unglazed flat-plate collectors

The simplest kind of solar collectors are unglazed solar collectors, consisting solely of an absorber. Even though in the past they were used in several applications, nowadays they are used exclusively for heating swimming pool water, as shown in Figure 1.4. This type of collectors have generally lower performance than a glazed flat-plate solar collector (at the same operating temperatures) because of the high thermal losses to the environment that occur mainly from forced wind convection.

Figure 1.4: Unglazed flat-plate solar collectors used to heat a large outdoor pool (Solarworks, 2007)

1.2.3 Evacuated tube collectors (ETC)

The purpose of the evacuated tubes technology is to minimize the thermal losses caused by convection especially when operated at high temperatures. For this reason glass cylinders, each containing an absorber plate, are evacuated to a minimum of 1 kPa. Thermal losses due to conduction are also moderated by further enlarging the vacuum inside the tubes. This leaves re-radiation as the only major loss mechanism. Minimizing these losses makes this specific type of collector achieve greater efficiencies than glazed flat-plate collectors, especially in colder climates. Figure 1.5 demonstrates a typical setup of an evacuated tube solar water heater on the roof of a building.

The absorber is usually installed either flat inside the tube or fused at the top side of the evacuated glass tube. All evacuated tubes are linked at the top by an insulated heat exchanger box called a “manifold”. There are two categories of evacuated tube collectors: The direct flow and heat-pipe type. The direct flow ETCs, that are most popular in China, use a U-shaped tube inside the glass bulb to travel the fluid that collects the heat from the absorber. In the heat-pipe ETCs a selectively coated absorber bonded to a heat pipe is inserted into the evacuated tube. A schematic of a typical heat-pipe ETC is shown in Figure 1.6.

Figure 1.5: Evacuated tube solar water heater at the roof of a building of the University of South Wales (Morrison, et al., 2005)

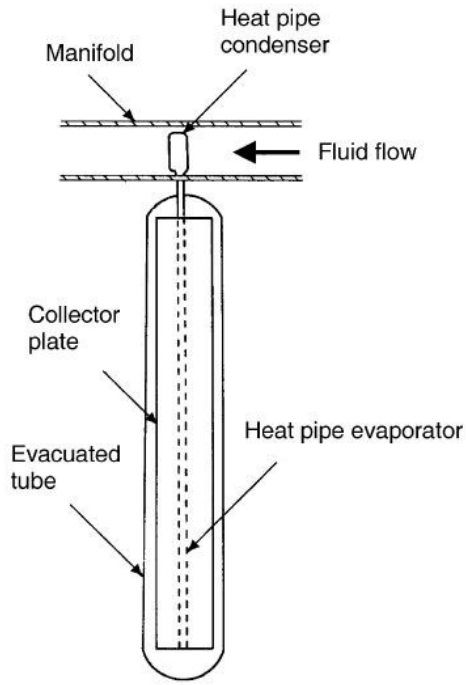

Figure 1.6: Schematic of a heat pipe ETC (Kalogirou, 2004)

1.3. *Research Objective*

The main scope of this thesis is to address the thermal performance-related effects of wind on solar collectors placed on the roofs of buildings. It is typical in the analysis of flat-plate solar collectors to assume a wind velocity measured at a representative location on the roof. However, wind does not affect uniformly all locations on large areas. The velocity distribution on different parts of the roof depends on the shape of the building, wind direction and surroundings of the concerned region. Such factors would be expected to have an effect on the convective heat losses from flat-plate solar collectors and, therefore, on their thermal performance.

The present study demonstrates the importance of using actual velocity distributions corresponding to different locations on the roof, as opposed to single velocity value measured at a reference location. The latter is achieved through an experimental investigation of the wind velocity distribution for different wind directions and on different locations of a building roof. The study also attempts the assessment of the wind impact on a flat-plate solar collector's performance characteristics when placed on different locations of the roof of a building model.

1.4. *Thesis Outline*

This thesis is organized into the next six chapters as follows:

- *Chapter 2:* Basic Wind Engineering concepts on flow phenomena around and on top of buildings and their simulation in wind tunnels.
- *Chapter 3:* Detailed literature review of previous wind tunnel and full-scale studies relevant to the present study.
- *Chapter 4:* Presentation of the wind tunnel facilities and experimental equipment. Description of parameters for wind tunnel tests and experimental procedure.
- *Chapter 5:* Presentation of results of the experiments and discussion of their practical consequences.
- Chapter 6: Description of the thermal model and results of the thermal performance of the solar collector.
- *Chapter 7:* Conclusions and recommendations for further research based on the results of this study.

Finally a list of references as well as two Appendices presenting the contour plots of wind velocity coefficients for the Cases that are not described analytically in the main body of this study (APPENDIX A1) and a sample evaluation of thermal energy gains (APPENDIX A2), are provided.

Chapter 2 – WIND ENGINEERING BASICS

2.1. *Wind Flow around Buildings*

Natural wind flow is very complex. Its flow patterns are always erratic due to the fact that most points in the flow path have different velocities. The closer we get to the ground surface, the more the wind velocity is reduced, as wind flow is constantly blocked by ground obstacles (i.e. buildings, trees, mountains etc.).

When wind flow over an open area approaches the boundaries of an urban area, it confronts a high level of roughness from the surface, primarily created by the buildings. As a result, the mean wind flow decreases. In general, wind velocities vary depending on the height they are measured at and the topography they are flowing over. For example if we measure a velocity at an open area like an airport or a field the value found will be higher than what would be measured, at the same height over a dense terrain like a town or a forest. This decrease in wind velocity as influenced by variable terrain roughness is illustrated in Figure 2.1.

The variation of mean wind speed with height in the atmospheric boundary layer is approximated by the well-known power law equation:

$$\frac{V_Z}{V_G} = (\frac{Z}{Z_G})^{\alpha} \qquad \textbf{(2-1)}$$

Where V_Z is the mean wind speed at height Z in the study site, V_G is the mean wind speed at the "gradient" height Z_G (top of the boundary layer of the study site, above which the speed is assumed to be constant) and α is an empirical exponent which

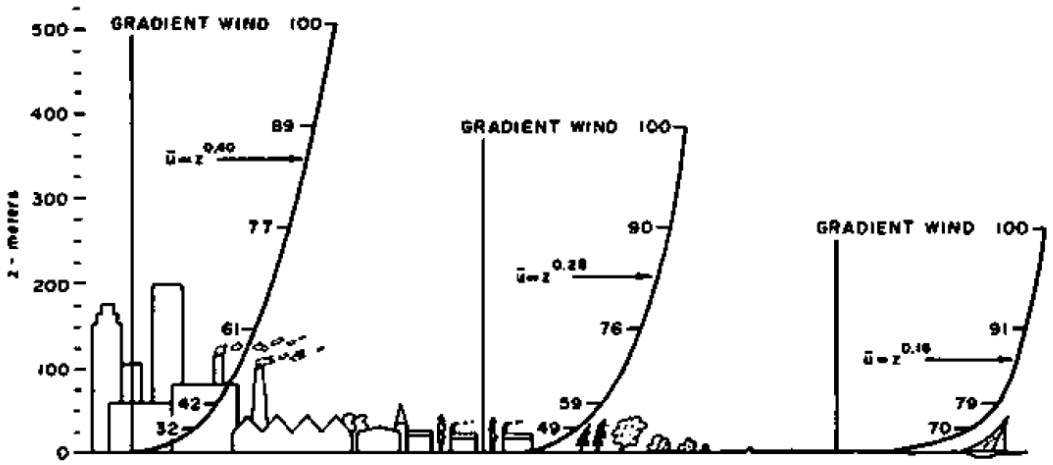

Figure 2.1: Mean wind velocity profiles for flow over terrains of different roughness (Davenport, 1967)

depends on the surface roughness, stability and temperature gradient). Table 2.1 shows typical values of Z_G and α for mean wind speeds over several types of

terrain. The values and terrain categories in Table 2.1 are consistent with those suggested in other engineering applications and codes.

The flows in flat open areas like above the sea, are relatively easy to model because they remain attached due to lack of obstructions. However, the flow around a non-aerodynamic body, such as a building, is more difficult to predict because of phenomena that develop around sharp building corners, resulting in complex turbulence.

Table 2.1: Gradient heights and power law exponents for different terrain types (Stathopoulos T. & Baniotopoulos C. (Eds), (2007))

Terrain Category	Terrain Description	Exponent α	Gradient Height Z_G (m)
1	*Very Flat Terrain:* Open sea, ice, tundra dessert	0.11	250
2	*Open Terrain:* Open country with low scrub or scattered trees	0.15	300
3	*Suburban Terrain:* Small towns and wooded areas and generally other areas with closely spaced obstructions	0.25	400
4	*Urban Terrain:* Numerous tall buildings, city centers, well developed industrial areas	0.36	500

2.2. *Flow Separation and Reattachment*

A typical wind vortex formation on the roof of a rectangular building can be seen in Figure 2.2. For the case of perpendicular wind approaching a basic isolated "bluff" body such as a rectangular building. As the wind hits against the upwind side of the building, it immediately comes to a rest at the "stagnation point" and the flow direction is completely altered from its standard path. The air flows along the building façade until it reaches the edges. Areas of high pressure and increased wind speed are created along the upper edge and sides of the building before it rushes over the top and sides. Eddy currents or small vortices are produced immediately after these windward edges.

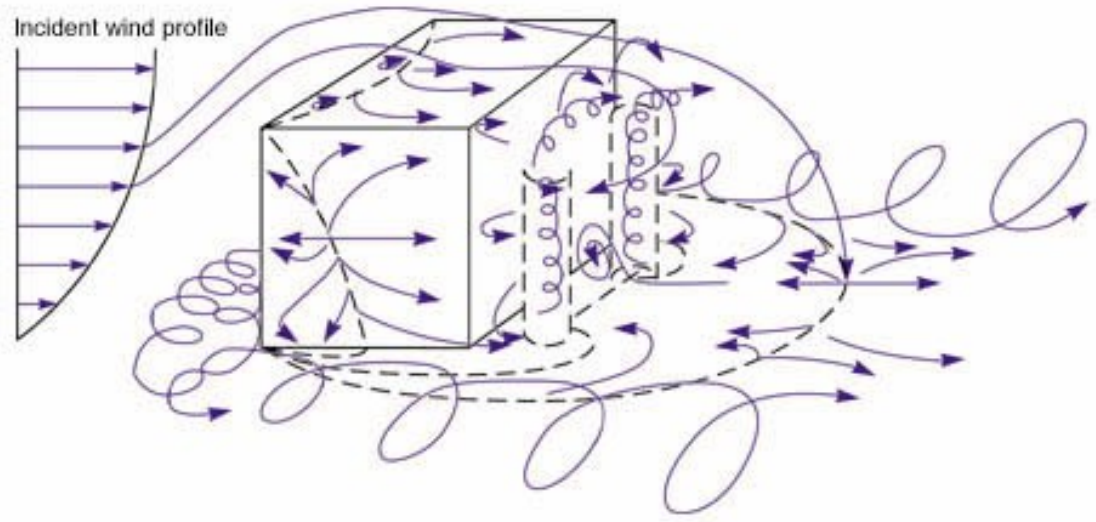

Figure 2.2: Three dimensional wind flow around a rectangular body (Woo, et al., 1977); modified

A minor increase of pressure and consequently wind speed along the downwind portion of the roof and sides are typically monitored. The wind then moves past the back of the building and forms a turbulent wake region and also downward the leeward façade where a large low pressure area is created that causes the wind to curl in to fill the void. For urban terrains, like densely constructed cities, these phenomena are a lot more complicated and challenging to assess analytically. In those terrains, where buildings are so close to each other, the flow patterns of the wind are extremely hard to predict. Generally, wind tunnel experimentation and simulations are the safest and most widely used procedures to examine the effects of such convoluted flows.

2.3. *Down-Washing Effect*

This type of flow occurs either when buildings of considerably different heights are located close to each other, or in the cases of podiums of tall towers. Wind is intercepted by the taller structure and washed downwards onto the roofs of the shorter structures, as shown in Figure 2.3. This condition, if severe, may make it uncomfortable to have an occupiable outdoor space on the lower roofs.

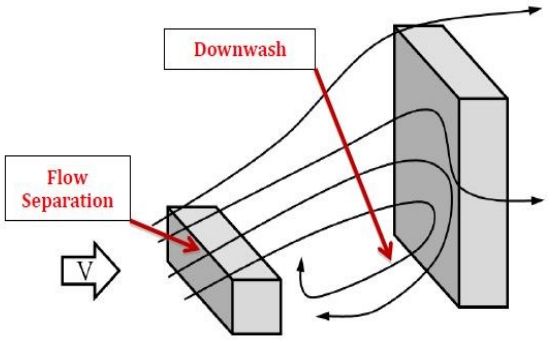

Figure 2.3: Flow separation and downwash effect (IBPSA-USA, 2012)

2.4. *Wind Channelling*

Buildings situated side by side cause wind to channel and accelerate in the small gap between them thereby inducing high suction on the leeward building edges and uncomfortable wind environment in the channel. In urban settings there is very little space between adjacent buildings; this leads to interaction between the flow fields around individual buildings and makes the net wind flow field even more complex, similar to Figure 2.4. The wind flow patterns around buildings have effects on a number of building performance aspects.

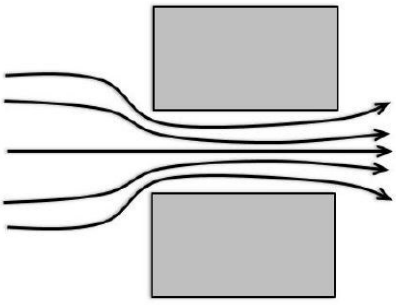

Figure 2.4: Wind channeling effect

Chapter 3 – LITERATURE REVIEW

3.1. *Wind Velocity Distributions above Flat Roofs*

A large number of studies have been conducted in the past concerning the analysis of wind flow around rectangular objects. On the other hand, not many of them, focus specifically on the distribution of wind velocities above the upper surface (roof) of the body.

The flow around a rectangular three-dimensional object was investigated by Kim, et al. (2003) with the use of the Particle Image Velocimetry Technique (PIV) in the atmospheric boundary layer wind tunnel at Pusan National University. The model was immersed in a thick turbulent boundary layer. Detailed structures and characteristics of the flow were obtained by averaging over numerous instantaneous velocity maps. The prismatic model (140 mm × 95 mm × 40 mm), made of glass, was located 18 m downstream from the entrance of the wind tunnel. To investigate the 3-D flow structures around the model, three measurement planes were used. The planes were set to be parallel to the flow

direction and located at y/H equal to $0.0H$, $0.5H$, and $1.0H$, where H is the height of the model, as shown in Figure 3.1.

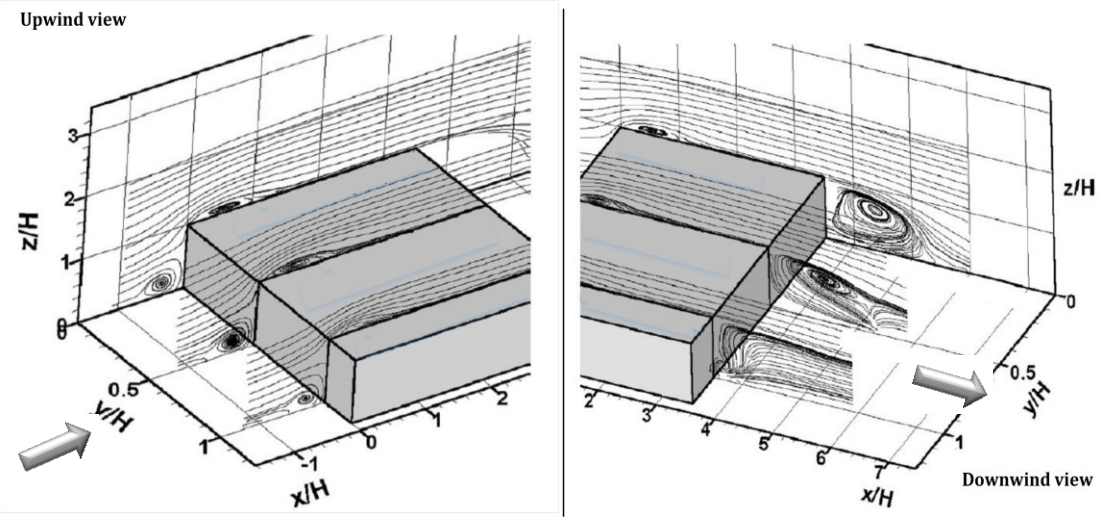

Figure 3.1: Upwind and downwind view of the 3-D flow structure around the model (Kim, et al., 2003)

Measurements were conducted at all three planes. The authors reported high velocities closer to the windward areas above the roof and lower at the leeward areas. Figure 3.1 shows that the upward flow separates at the upwind roof edge and the downward flow forms a frontal eddy. The separated layer at the upwind roof part re-attaches on the roof and forms a turbulent recirculation zone close to the windward areas. This flow goes then downstream along the surface of the roof and separates again at the leeward roof edge, creating an area of high turbulence at the back side of the model.

Similar results were obtained with the calculation of the turbulent kinetic energy (TKE), which is proportional of the square of the local velocity V_{loc}. Figure 3.2 compares TKE of the three measurements at several locations around the model.

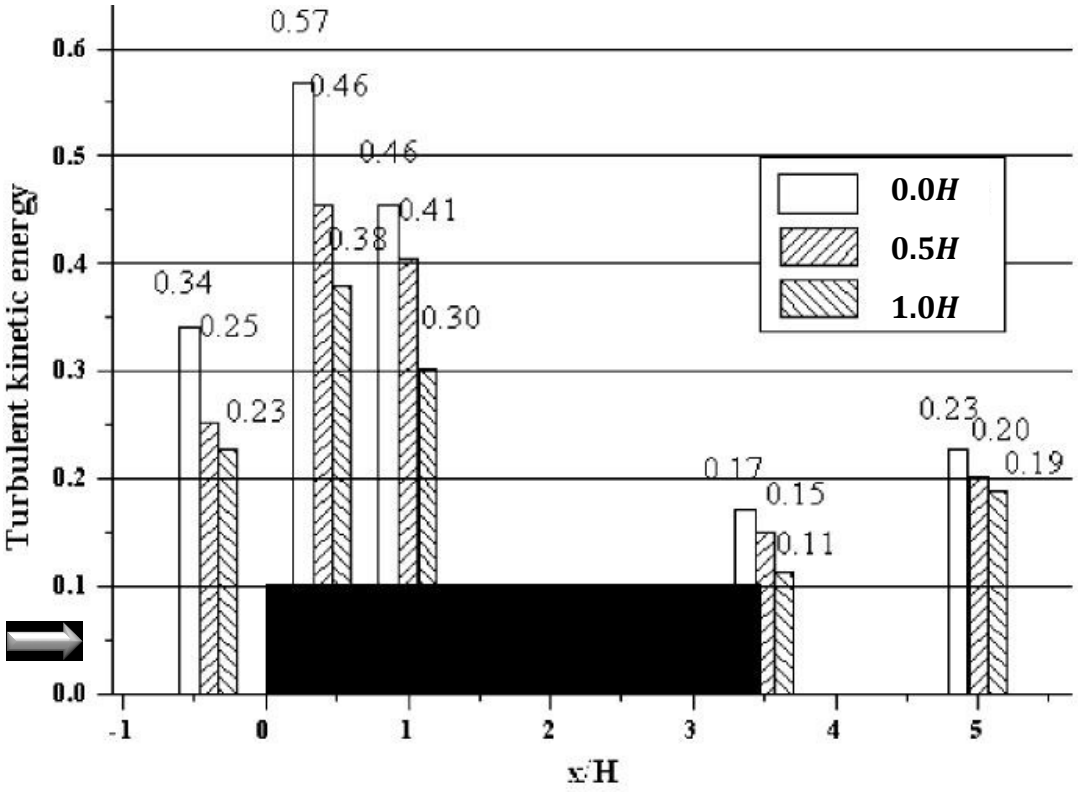

Figure 3.2: Maximum TKE at the three different measurement planes (Kim, et al., 2003); modified

Once again, TKE is higher at the upwind areas, where the wind separates and accelerates at the edges. It is however noticeable, that TKE is higher at 0.0*H* plane rather than the edges.

Comparable results regarding the distribution of velocity and TKE above the upper surface of a rectangular cube were reported by Yakhot, et al. (2006). The study employed an immersed-boundary method to perform a direct numerical simulation (DNS) of flow around a wall-mounted cube in a fully developed turbulent channel, based on the velocity and the channel height. The velocity streamlines as well as the contour plot of the turbulent kinetic energy in the xz-plane are shown in Figure 3.3.

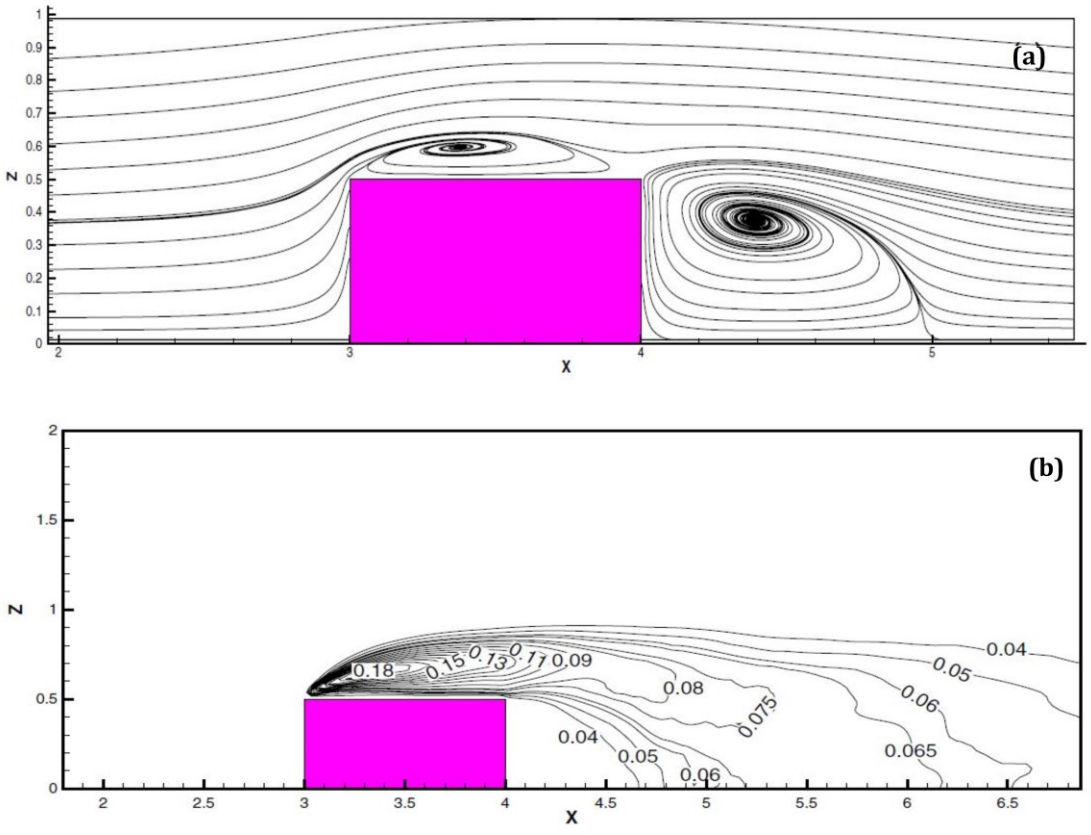

Figure 3.3: (a) V_{loc} streamlines and (b) TKE contour plot in the xz-plane (Yakhot, et al., 2006)

Lim & Castro (2009) presented a numerical simulation of flow around a surface mounted cube placed in a turbulent boundary layer. Mean velocity data within the boundary layer at the cube location and around the cube itself were obtained using appropriate combinations of Hot Wire Anemometer (HWA), Laser Doppler Anemometer (LDA) and Particle Image Velocimetry systems (PIV). Figure 3.4 presents the vertical profiles of the mean velocity above the axial centerline of the cube, comparing the computational data with those measured in the wind tunnel. The vertical gridlines along the x-axis are equally spaced to delineate the spatial growth of the wind flow over the cube.

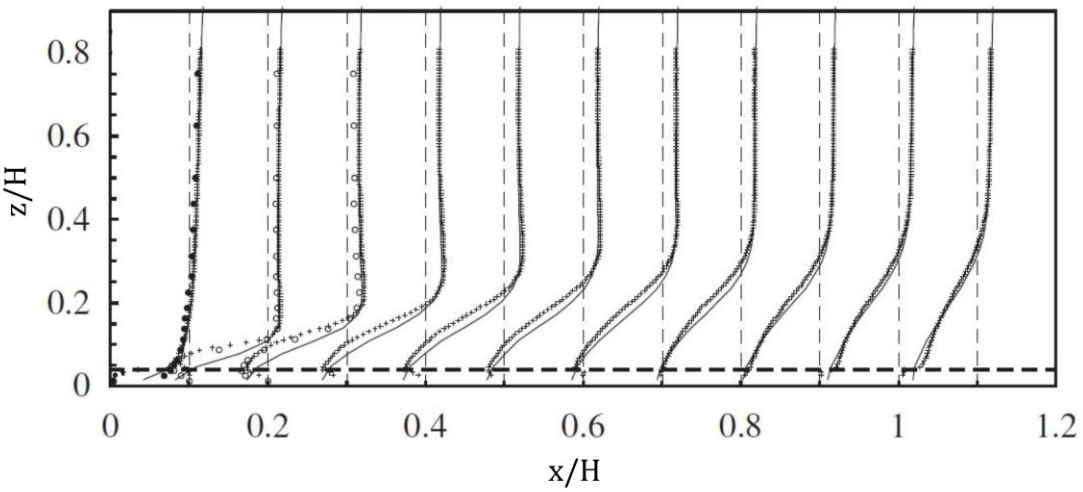

Figure 3.4: Stream wise velocity profiles over the cube. LES simulation (Solid line), PIV (+) and LDA (o) (Lim & Castro, 2009)

The flow exhibits a typical separation at the leading edge (x/H = 0) and accelerates instantaneously at the front part above the roof (x/H = 0.2). The wind velocity tends to become smaller towards the back area of the roof. It is clear from

the aforementioned studies that there is a specific pattern of the wind velocity distribution above flat roofs, i.e. velocities are higher above the upwind and lower above the downwind locations.

However, these studies have several drawbacks, particularly in the context of the study of performance of solar collectors on roofs. For instance, the effect of wind direction is not taken into account. Furthermore, solar collectors are usually installed in residential or commercial buildings that exist in urban areas. Therefore, the wind behavior above the roof is constantly changing based on the surroundings of the building.

3.2. *Wind-Induced Convective Heat-Transfer Coefficients*

It is common that the upper surface of a flat-plate solar collector is exposed to the natural environment so that solar energy can be absorbed. The front surface can be the absorber itself, in the case of unglazed collectors, or one or two sheets of glass in the case of single or double glazed collectors. Regarding glazed collectors, heat losses occur as the glass temperature is commonly higher than the ambient temperature. Usually, during low wind velocities, heat-transfer takes place by free convection whereas forced convection takes over at medium and high wind velocities.

Usually free of obstructions, with good exposure to the sun, rooftop solar installations represent an efficient use of space. However, many factors must be

considered before deciding whether a roof is a suitable candidate. The most critical effect that wind may cause on solar-thermal devices is convectional cooling. The distribution of wind velocity impinging on a horizontal surface is, in most cases, non-uniform depending on the direction of the approach wind and position of surrounding structures. Knowing the actual wind velocity distribution on a building roof enables accurate calculation of possible convection losses that the collector would be subjected to and this in turn aids in improving its performance.

It is very important for an engineer to be able to calculate the wind-induced heat losses in solar collectors as they play a significant role in their efficiency and more specifically in colder environments that surface-to-ambient temperature variances are way higher. It has been calculated that for a typical single-glazed collector functioning at 40% efficiency with no air movement, its efficiency would drop to 30% if the wind velocity had been 3 m/s (National Bureau of Standards, 1978).

Wind induced convective heat transfer coefficients for building surfaces, are normally determined experimentally because of their dependence on a variety of parameters like the building geometry, wind speed and direction, local topography, turbulence intensity etc. (Karava, et al., 2011). It is essential that solar-thermal devices be positioned such that convection cooling due to wind is minimal. A field study by Sparrow, et al. (1981) showed that wind-induced convection on roof mounted flat plates was higher in the case of separated flows

than non-separated flows incident on the plate-surface. Numerous studies have been performed in the past to establish a relationship between the convective heat transfer coefficient and the reference air velocity for flat-plate solar collectors.

3.2.1 Wind Tunnel Studies

(Jürges, 1924)

The earliest experimental work that has been documented regarding forced convective heat transfer was by Jürges (1924). As it was described by McAdams (1954), a 0.5 m^2 copper plate attached vertically and flush with the side of a wind tunnel, was heated. A correlation was yielded for smooth surfaces after the air speed was measured at the center of the tunnel:

$$h_w = 3.95V_{loc} + 5.8 \qquad \textbf{(3-1)}$$

Jurges's results were widely considered as the best way to calculate h_w for many years. Duffie and Beckman (2006), who cite Jürges (1924), also stated that this equation probably includes both free convection and radiation effects, thus overestimating the value of h_w. According to Duffie and Beckman (2006), it is not reasonable to adopt (3-1) for plate area higher than 0.5 m^2. However, this

equation has often been applied to flat-plate solar collectors with area greater than 0.5 m^2, due to the lack of an equivalent dependable equation.

(Watmuff, et al., 1977)

The overestimation of h_w by (3-1) was addressed by Watmuff (1977) who managed to exclude the radiation term, leaving only the convective parameter and resulting with the following equation:

$$h_w = 3.0V_{loc} + 2.8 \qquad \textbf{(3-2)}$$

(Sparrow, et al., 1979)

The purpose of the study was to investigate the nature of heat transfer and the fluid flow characteristics for two flat plates, one wide and one narrow, inclined at an angle of attack to an air stream. The wind tunnel experiments were performed for angles between 25° and 90° (Figure 3.5), using the "naphthalene sublimation method", for different air velocities against smooth, rectangular-shaped surfaces. Based on the experimental data, an h_w correlation was obtained in order to describe sufficiently the wind incidence angles and Reynolds numbers that were used during the experimental procedures. For example, for mean plate-air temperature of 313 K the wind-induced convective heat transfer coefficient is given by:

$$h_w = 5.1{V_{loc}}^{0.5}L^{-0.5} \qquad \textbf{(3-3)}$$

for $L = (4 * plate\ area)/(plate\ circumference)$. Although this study was experimentally extensive, it did not simulate a realistic situation of a solar collector on a roof of a real building.

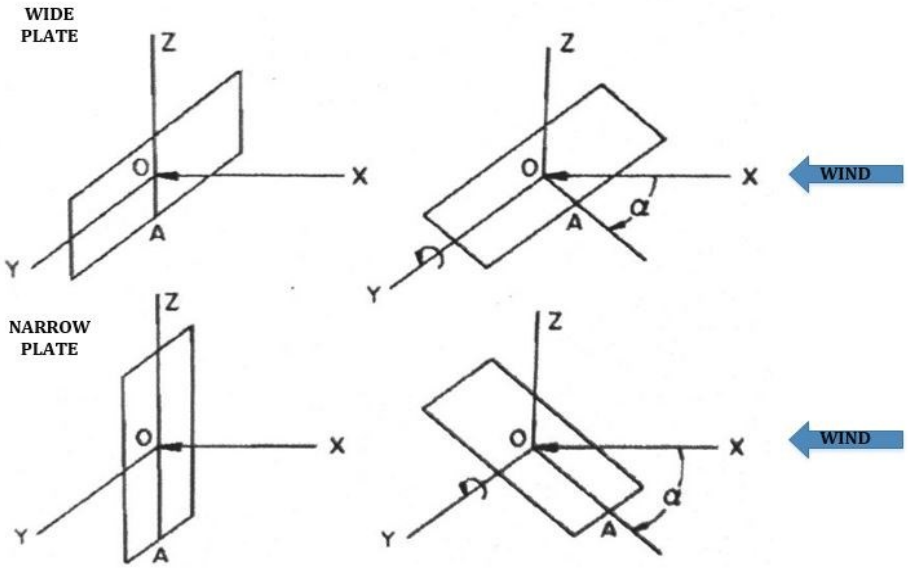

Figure 3.5: Schematic view of the two plates (Sparrow, et al., 1979)

(Kind, et al., 1983)

A 1:32-scaled model of a single family residence was used in a wind tunnel to calculate convective heat-transfer coefficients on the surface of a flat-plate solar collector (1.2 m × 2.4 m) that was mounted on the roof of the model. A schematic of the model used can be seen in Figure 3.6.

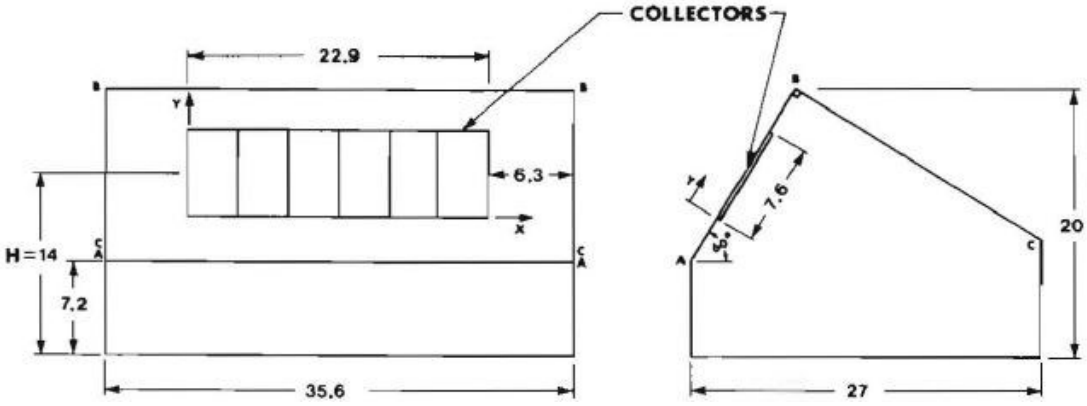

Figure 3.6: Diagram of model; dimensions in cm (Kind, et al., 1983)

Results showed that h_w values extrapolated from full-scale Reynolds numbers are 2-3 times smaller than those predicted by a wind tunnel experiment similar to that of Jürges (1924). Also, the sensitivity of h_w to turbulence and building details was small. It was noted that at φ=90°, where the plane of the collector is aligned with the wind direction (see Figure 3.7), the heat-transfer

coefficients are at their highest values, whereas at φ=135° or 180° (collector at the leeward side) h_w is minimum.

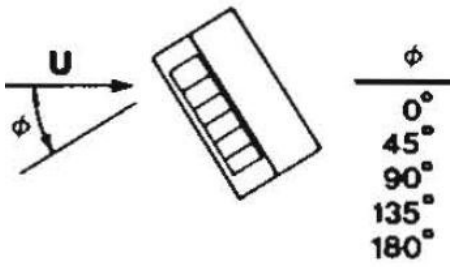

Figure 3.7: Wind angles of attack (Kind, et al., 1983)

(Shakerin, 1987)

The purpose of these wind tunnel experiments was to measure the convective heat-transfer coefficient h_w, on a rectangular aluminum flat-plate (30.2 cm × 29.2 cm × 1 cm) flush mounted on a wooden model of a roof of a building. The experiment was similar to Kind, et al. (1983) with the difference that in this case the roof pitches of the models were variable between 0°-90°. The experimental setup can be seen at Figure 3.8. The aluminum plate was insulated at the back with a Styrofoam block to minimize unwanted thermal losses. Thermocouples were also placed next to the surface of the plate to measure the surface temperature.

Convective heat-transfer coefficients were found to be higher for 0° and 30° roof pitch due to the formation of a separation bubble at the leading edge of the roof. Overall, it was found that below the critical angle of 40°, h_w values were higher than those calculated by equation (3-3). For α>40° the flow was found to be laminar above the model and the wind induced convective heat transfer coefficient was independent of the angle of attack and values would agree with equation (3-3).

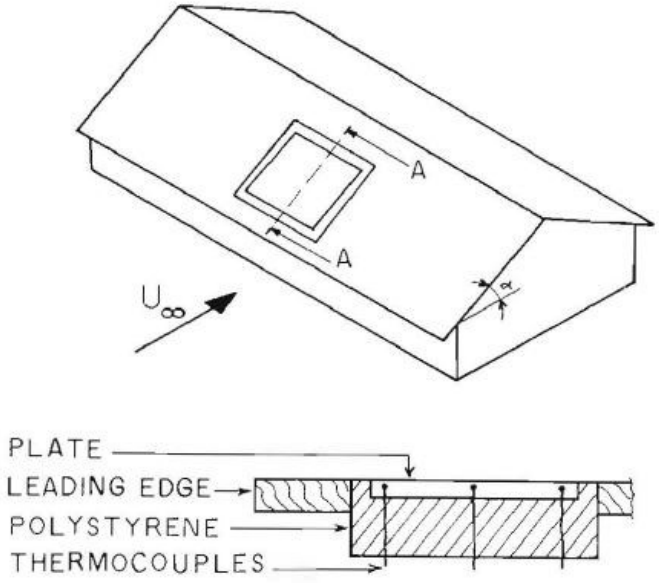

Figure 3.8: Model schematics (Shakerin, 1987)

3.2.2 Full Scale Studies

(Sturrock, 1971)

The study included extended nocturnal measurements of the wind-induced convection coefficient at a small number of points on the external surface of a tower block under natural conditions. The results confirmed the importance of wind direction on the magnitude of the wind-induced convection coefficient. The author suggested equation (3-4) for the calculation of the coefficient:

$$h_w = 11.4 + 5.7 * V_{loc} \quad \textbf{(3-4)}$$

(Test, et al., 1981)

The effort of the investigation was to explore wind-induced convective heat transfer from surfaces that were open to real wind. For the experiments, a heated plate (1.22 m × 0.813 m) was positioned in an external location and the wind speed was logged 1 m above the plate. Special side attachments were made in order to preserve roughly two-dimensional flow over the plate when exposed to alternating wind directions. For wind measurements a Gill (*uvw*) anemometer was used; it is a triaxial array of helicoid propellers each driving a small DC generator (NovaLynx, 2013). The setup of the experiment can be seen in Figure

3.9. All runs of the experiment were at an angle of attack of 40° (except one at 50°) and were all compared with wind-tunnel results.

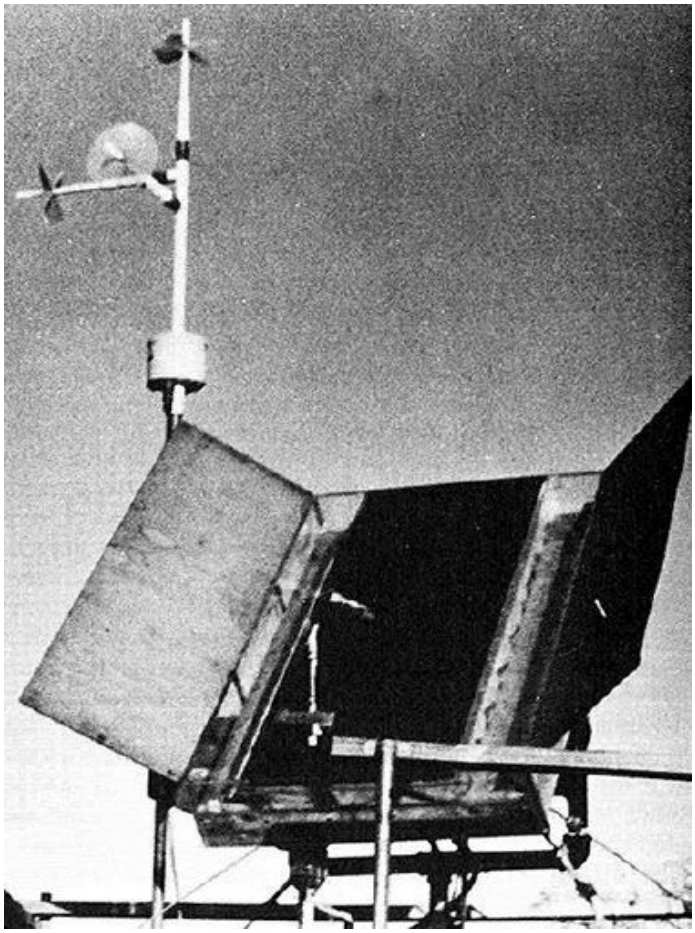

Figure 3.9: Test plate with sides and Gill anemometer (Test, et al., 1981)

Finally, a linear relationship between wind velocity and wind-induced convective heat transfer coefficient was established:

$$h_w = 8.55 + 2.56V_{loc} \quad \textbf{(3-5)}$$

(Kumar, et al., 1997)

Indoor experiments were conducted to evaluate the thermal performance of a box type solar cooker. In order to calculate the h_w, a heated square plate of size equal to the aperture area of the solar cooker was employed. A fan was used to produce airflow of different speeds over the surface of the solar cooker and the heated plate.

A correlation was derived from the experimental data connecting the wind-induced heat-transfer coefficient and wind velocity:

$$h_w = 10.03 + 4.687V_{loc} \quad \textbf{(3-6)}$$

(Sharples & Charlesworth, 1998)

Full-scale measurements were performed in the real environment to determine the magnitude and flexibility of the wind-induced convective heat-transfer from an elevated heated surface (1.81 m × 0.89 m) attached directly onto the pitched roof (35˚) of a domestic size building (9.6 m × 5.03 m × 4.59 m) as seen in Figure 3.10.

Figure 3.10: Single Storey building used (Sharples & Charlesworth, 1998)

Wind velocity V_{loc} was measured with a traditional lightweight three-cup vane anemometer which was mounted on a mast 1.5 m above the ridge line of the roof at the west end of the building – or 6.1 m above the ground – which made the experiment similar to Test, et al. (1981). The experimental setup can be seen in Figure 3.11. The forced convective heat transfer coefficient h_w was correlated against the measured wind speed and direction, as seen in Table 3.1 and plotted in Figure 3.12.

Figure 3.11: Heat transfer equipment in position on roof (Sharples & Charlesworth, 1998)

Table 3.1: Regression equations of h_w on V_{loc} by wind incidence angle (Sharples & Charlesworth, 1998)

Wind Incidence Angle (deg)	Regression Equations for h_w $(\frac{W}{m^2K})$	
0	$2.2V_{loc} + 8.3$	**(3-7)**
45	$2.6V_{loc} + 7.9$	**(3-8)**
90	$3.3V_{loc} + 6.5$	**(3-9)**
135	$2.2V_{loc} + 7.9$	**(3-10)**
180	$1.3V_{loc} + 8.3$	**(3-11)**
-135	$2.3V_{loc} + 7.8$	**(3-12)**
-90	$2.2V_{loc} + 11.9$	**(3-13)**
-45	$3.9V_{loc} + 6.0$	**(3-14)**

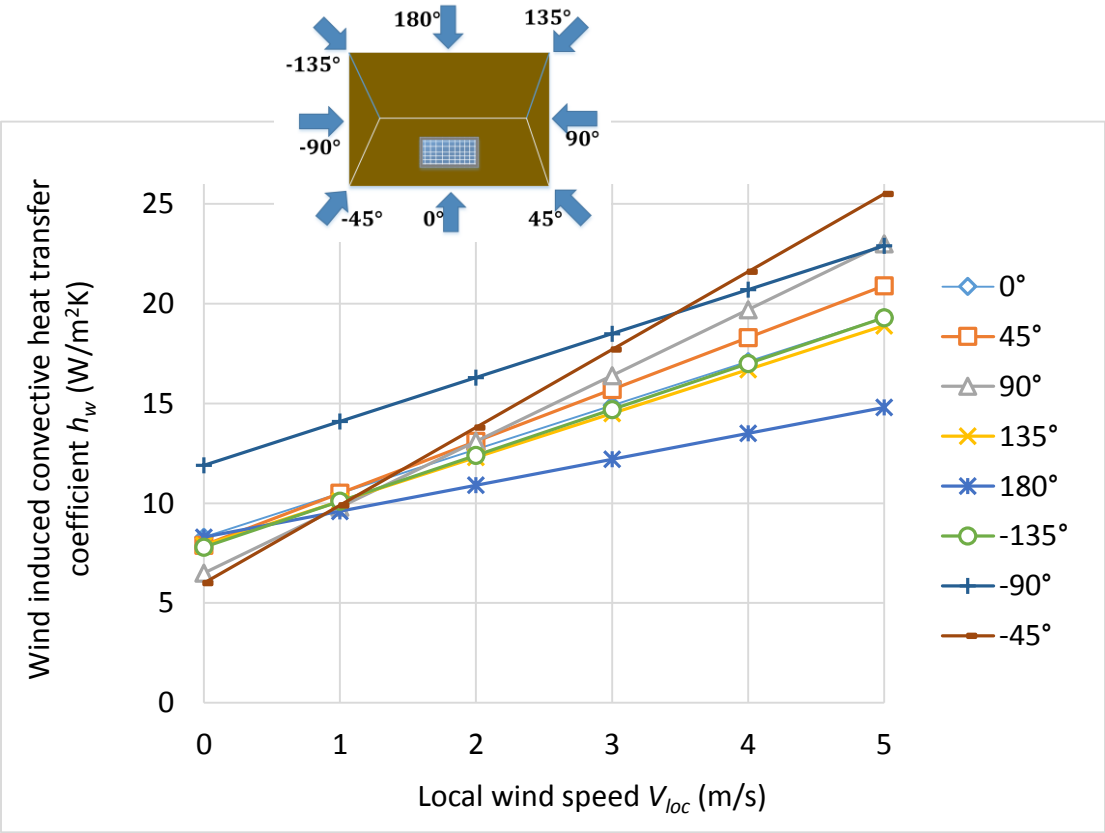

Figure 3.12: Plot diagram of regression equations from Table 3.1

(Hagishima & Tanimoto, 2003)

For this study, the tree-dimensional wind velocity was measured with an ultrasonic anemometer at four points on the roof of an actual two-storey building (22.5 m × 15.3 m). Figure 3.13 presents a photograph of the slab used during the study, situated next to a higher four-storey slab. The anemometer was located 13 cm above the roof surface. The wind direction was also logged during the same time period. The wind-induced convective heat-transfer coefficient and the wind

Figure 3.13: Horizontal roof slab (Hagishima & Tanimoto, 2003)

velocity were plotted in Figure 3.14 and equation (3-15) was finally proposed:

$$h_w = 3.95V_{loc} + 5.8 \qquad \textbf{(3-15)}$$

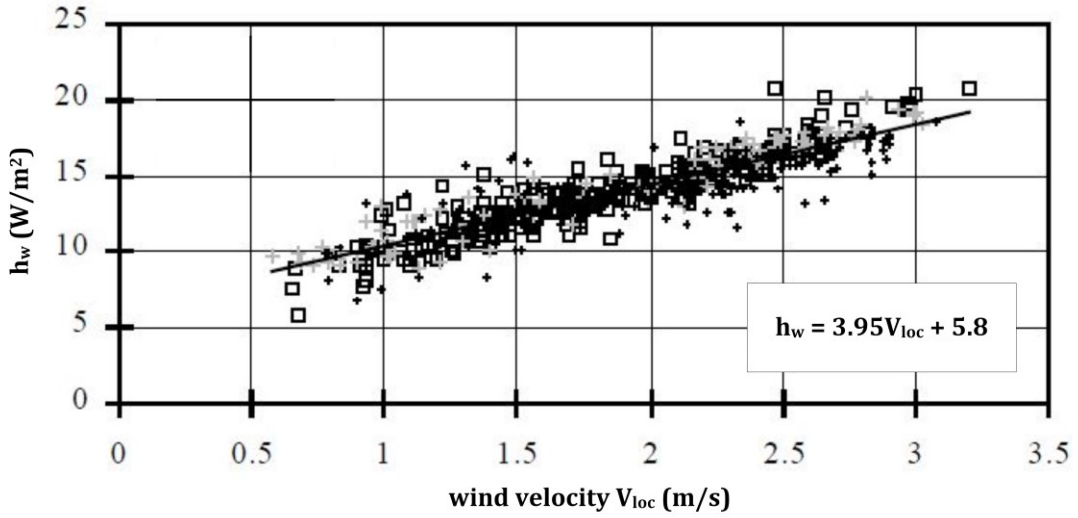

Figure 3.14: Relationship between local wind speed V_{loc} and h_w (Hagishima & Tanimoto, 2003)

(Kumar & Mullick, 2010)

Full-scale experiments were conducted to evaluate the wind-induced convective heat transfer coefficient from the top surface of an unglazed solar collector (0.925 m × 0.865 m × 0.002 m). The aluminum plate, which was coated with black board paint, was positioned on the rooftop of an 8.33 m building in the Indian Institute of Technology in Delhi, India. In order to reduce heat losses from the sides and the back of the plate, thermocole slabs were placed securely around it. Wind velocity measurements were performed with a Lufft three-cup

anemometer that was positioned next to the plate and 0.15 m above it. Figure 3.15 presents the setup of this experiment.

Figure 3.15: Experimental setup (Kumar & Mullick, 2010)

The wind-induced heat transfer coefficient was found by the use of heat-balance equations for the test plate. The data used for its calculation were those taken for about one-and-a-half hour around solar noon (steady state conditions) for the months of February - May for 2 years. The value of h_w was calculated with the methods of linear and power regression with respect to V_{loc} (Table 3.2):

Table 3.2: Regression equations of h_w on V_{loc} (Kumar & Mullick, 2010)

Regression	Correlation	
Linear	$h_w = 6.9 + 3.87V_{loc}$	**(3-16)**
Power	$h_w = 6.63 + 3.87V_{loc}^{0.8}L^{-0.2}$	**(3-17)**

3.2.3 Analytical Studies

(Sartori, 2006)

Analytical work was performed, aiming to compare the equations introduced around the time of the study, for the calculation of the heat transfer coefficient by forced convection over plane surfaces and particularly over flat-plate solar collectors. Incropera & deWitt (1985) introduced theoretical laminar and turbulent boundary layer correlations for wind-induced convective heat transfer and expressed those using dimensionless Nusselt, Reynolds and Prandtl numbers:

$$Nu = 0.664 Re_L^{0.5} Pr^{0.33} \quad laminar\ flow \tag{3-18}$$

$$Nu = 0.037 Re_L^{0.8} Pr^{0.33} \quad turbulent\ flow \tag{3-19}$$

where L is the surface length in the wind direction (m). Using equations (3-18), (3-19) and the boundary layer theory, new equations for the calculation of h_w were obtained:

$$h_w = 3.83 V_{loc}^{0.5} L^{-0.5} \quad for\ laminar\ flow \tag{3-20}$$

$$h_w = 5.74 V_{loc}^{0.8} L^{-0.2} \quad for\ turbulent\ flow \tag{3-21}$$

$$h_w = 5.74 V_{loc}^{0.8} L^{-0.2} - 16.46 L^{-1} \quad for\ mixed\ flows \tag{3-22}$$

3.2.4 Computational Fluid Dynamics (CFD) Studies

(Emmel, et al., 2007)

Computational fluid dynamics (CFD) analyses were performed to measure the convective heat-transfer coefficient at all external surfaces (façade & roof) of a simple shape low-rise building (8.0 m × 6.0 m × 2.7 m). Four different wind velocities (1 m/s, 5 m/s, 10 m/s, 15 m/s) and three different directions (0˚, 45˚, 90˚) were considered:

A three-dimensional steady-state incompressible flow, based on Reynolds-averaged approach was used. The research concluded on different correlations of convective heat-transfer coefficient for walls and roofs based on surface-to-wind angle (Table 3.3):

Table 3.3: Convective heat-transfer coefficient correlations for roofs; modified (Emmel, et al., 2007)

Surface-to-wind angle (deg)	h_w $(\frac{W}{m^2 K})$	
0	$5.11V_{loc}^{0.78}$	**(3-23)**
±45	$4.60V_{loc}^{0.79}$	**(3-24)**
±90	$3.67V_{loc}^{0.85}$	**(3-25)**

3.3. *Discussion*

Figure 3.16 presents the equations that were discussed in section 3.2 for the wind-induced convective heat-transfer coefficient (for 0° wind). Based on this illustrative comparison, a common trend is obvious in the variation of h_w with wind velocity. Nevertheless, the results of most of the studies are clearly separated from each other. It is important to indicate three sets of trend lines in Figure 3.16:

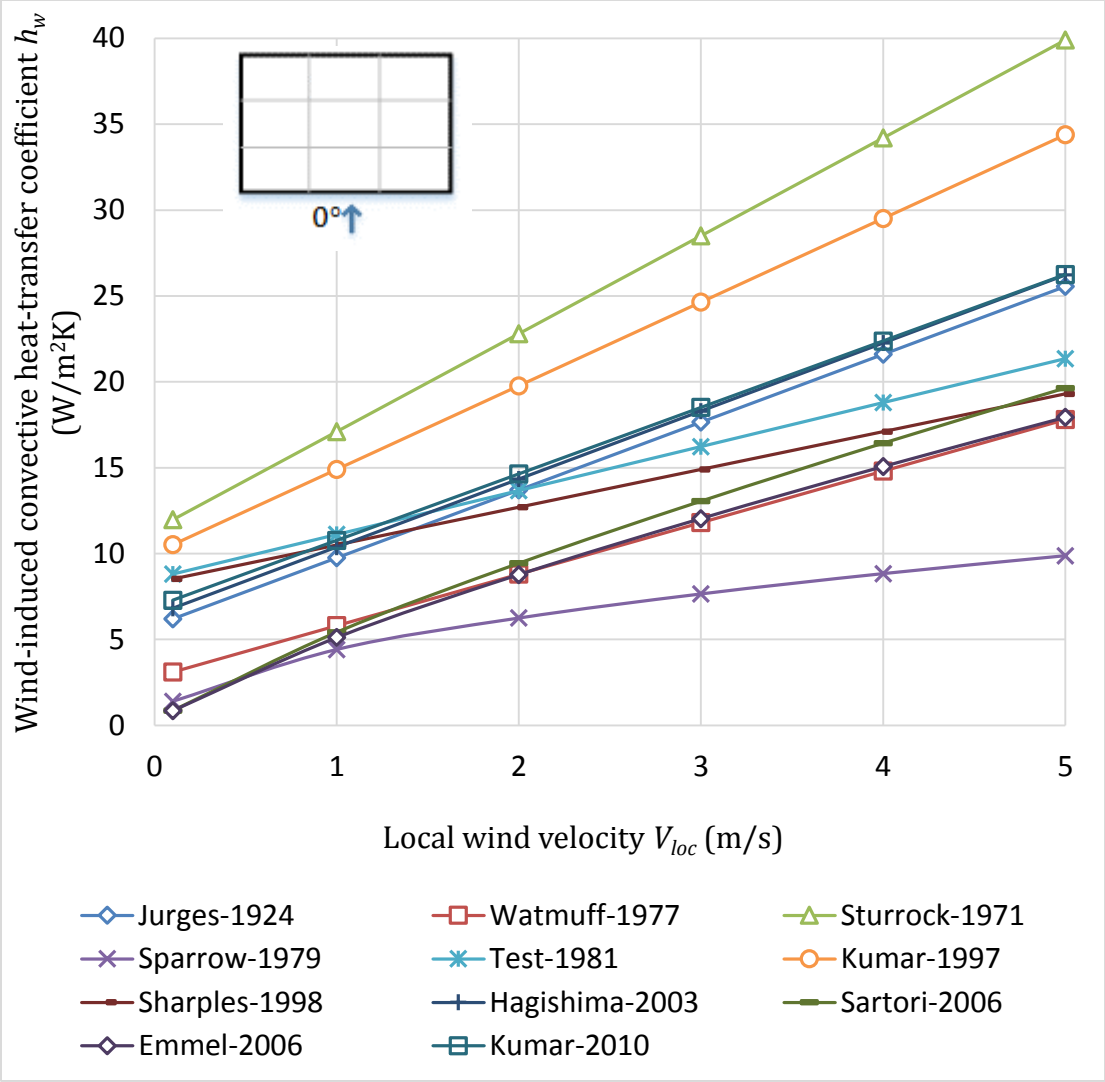

Figure 3.16: Comparison of h_w correlations of cited studies for 0° wind

1. The equations that produce the lowest results: The CFD study from Emmel, et al. (2007), the analytical study by Sartori (2006) and the wind tunnel study by Sparrow, et al. (1979). These studies clearly underestimate the wind-induced convective heat transfer coefficient.
2. The equations that produce the highest results: The full scale studies from Sturrock (1971) and Kumar, et al. (1997). These studies produce very high

values. Regarding the study of Kumar, et al. (1997) an explanation might be the additional turbulence that is caused by the industrial fan which was used during the indoor experiments.

3. The remaining equations are situated in the middle of the graph and produce relatively similar results. They are full-scale or wind tunnel studies.

Test, et al. (1981) suggested that in the natural environment, the free stream disturbances are at an order of magnitude higher than those in the wind tunnel for the same wind speed. As a result, higher heat transfer is to be expected during full-scale experiments. A similar notion was given by Sharples and Charlesworth (1998), mentioning that during low wind speed conditions, natural convection phenomena take place in the natural environment. Therefore, there are notable differences in wind tunnel and full-scale experiments.

The present study deals with applying experimental data into defined relations for flat-plate solar collector performance parameters, like thermal energy heat gains and efficiency. It is apparent then, that the equations that would be adopted, would be the ones that were developed for configurations similar to those used in the present study.

Chapter 4 – EXPERIMENTAL WORK

The purpose of this study is to quantify the potential thermal energy gains differences between solar collectors installed above different locations of flat roofs. In Chapter 3 it was shown that the wind-induced convective heat transfer coefficient h_w is a function of the local wind velocity V_{loc}. Therefore, it is imperative to understand the behavior of wind velocity distributions above roofs in several circumstances, such as different incidence angles and local surroundings. Furthermore, as explained in Chapter 3, past studies did not examine different cases of wind velocity distributions for use in solar collector thermal modelling. This chapter is about the wind tunnel study that was conducted at the Building Aerodynamics laboratory at Concordia University. It involved a series of measurements on the roof of a small scale flat-roof model of a rectangular building for different configurations and wind directions. The wind tunnel facility, the boundary layer simulation and the equipment used during this analysis are described in detail, herein.

4.1. *Boundary Layer Wind Tunnel*

A wind tunnel is a tool used in aerodynamic research to study the effects of air moving past structures and other solid objects by simulating the natural

characteristics of wind at a suitable scale. The experiments described in this chapter took place at the Building Aerodynamic Laboratory located at the EV building of the Sir George Williams Campus (SGW) of Concordia University.

The wind tunnel of Concordia University is an open circuit wind tunnel, 12.2 m in length and 1.8 m in width, with a suspended roof that allows the height to be adjusted between 1.4 m and 1.8 m. Figure 4.1 shows a schematic of the wind tunnel, construction details of which were presented by Stathopoulos (1984).

Models are customarily placed into the downstream section on a turntable of 1.21 m diameter which can revolve manually or electrically and allows them to be rotated in order to be tested for different wind directions. Models can also be tested for different heights as they can move up and down, thus changing their corresponding building height. The wind tunnel's centrifugal blower can produce wind speeds that range from 3 m/s to 14 m/s.

The floor of the tunnel section is covered with a specific type of carpet which is used to mimic the open country terrain roughness. For different terrain types to be simulated, roughness elements like egg-boxes or Styrofoam cubes can be inserted on the wind tunnel test section.

It is of paramount importance to accurately replicate the atmospheric boundary layer wind velocity profile while performing wind tunnel experiments on small-scale models.

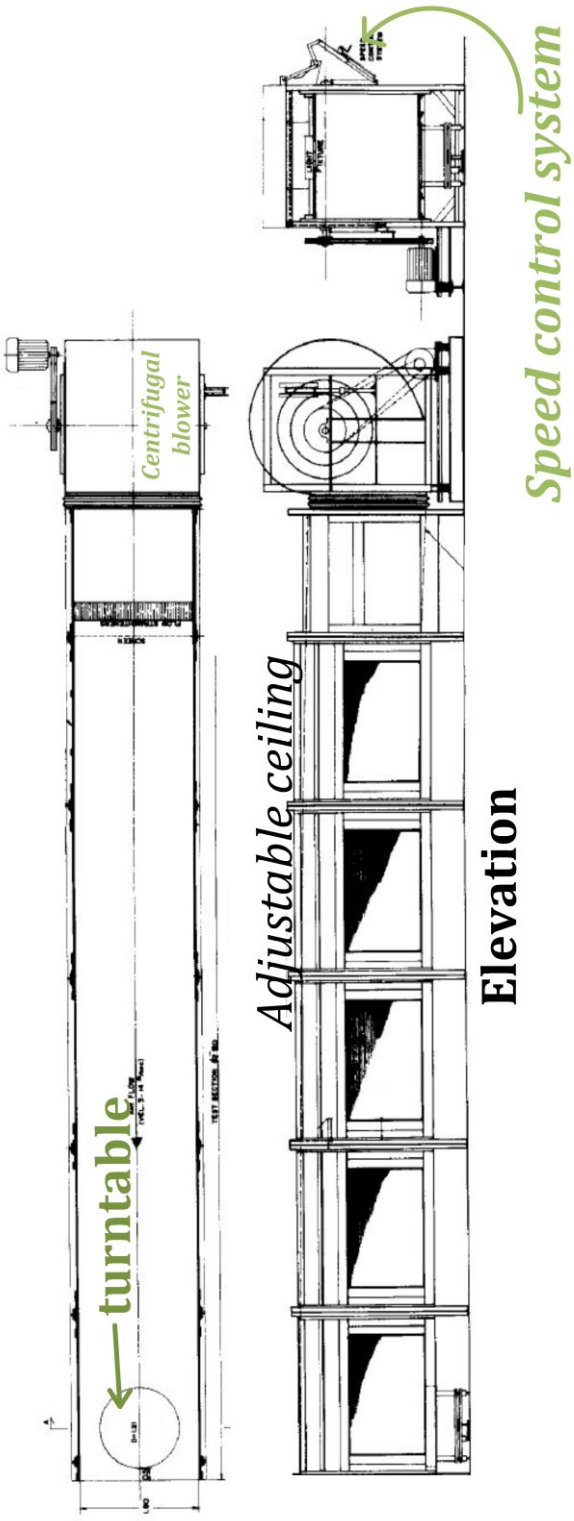

Figure 4.1: Schematic of the boundary layer wind tunnel at Concordia University (Stathopoulos, 1984); modified

The spectra of longitudinal turbulence was measured and compared with the analytical (Von Karman's) and empirical (Davenport's) representations of the spectra of natural wind, concluding to a satisfactory scale of 1:400 as it is shown in Figure 4.2.

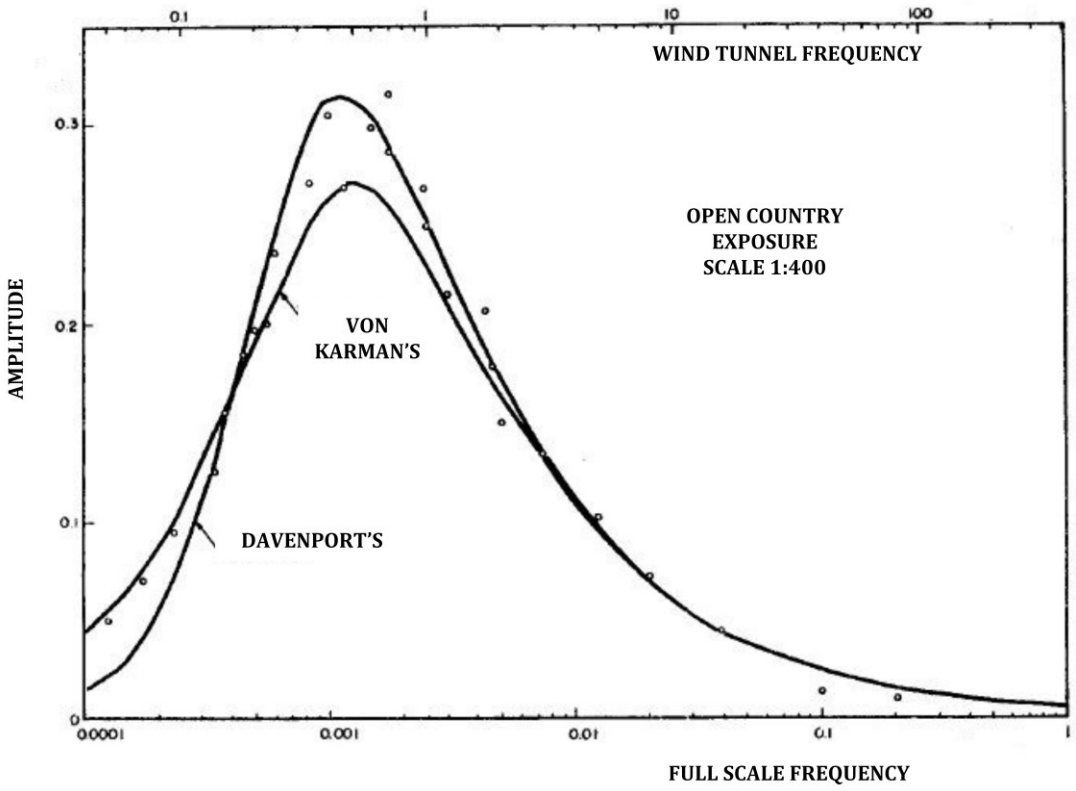

Figure 4.2: Spectra of longitudinal turbulence for 1:400 scale (Stathopoulos, 1984)

For the purposes of the study, an open terrain wind profile was simulated, therefore, no further adjustments needed to be made in the wind tunnel since the floor is covered by a carpet, by default, which simulates this specific terrain category.

The experimental velocity distribution was compared with the empirical profile obtained by the power law equation (2-1) for α = 0.130 and V_G = 12.4 m/s. Figure 4.3 illustrates the curves of the normalized velocity, as well as the turbulence intensity profile at the same heights.

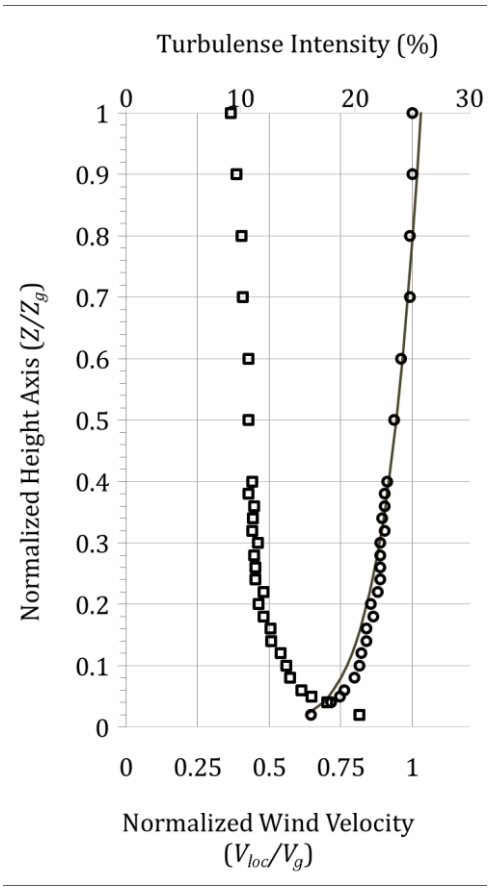

Figure 4.3: Experimental, empirical velocity profiles and turbulence intensity (α=0.130, scale 1:400)

The comparison shows relatively good agreement between the experimental and empirical profiles.

4.2. *Cobra Probe with Three-Dimensional Traversing System*

The multi-hole Cobra probe, by Turbulent Flow Instrumentation (TFI), is a flow measurement device with the capability to measure and resolve local static-pressure and all three components of velocity (*xyz*). The Cobra probe is very efficient in measuring accurately turbulent flows. The device's length is 16 cm and the diameter of the tube that houses the pressure transducers and other electronics is 1.4 cm. Finally, from the one side of the tube extends a 5 cm long stem and a 0.5 cm long head (Figure 4.4).

The Cobra probe as a self-contained unit requires only connecting to a computer with graphical user interface and data acquisition card. The instrument enables the control of the measurement process and displays the data on the computer's screen. The software enables the user to control the experimentation process and displays all data in real time. The software also stores the data in files that can be exported as spreadsheets.

The Cobra probe moves inside the wind tunnel with the help of a three-dimensional traversing system. The mechanism is situated at the wind tunnel ceiling right above the test section. The probe is fitted onto the traversing arm during experiments and moves in all three dimensions (*xyz*) inside the wind tunnel and more specifically around the model by entering Cartesian co-ordinates

of the desirable position. Therefore, the user has the capacity to perform the most accurate velocity measurements at any location nearby the model.

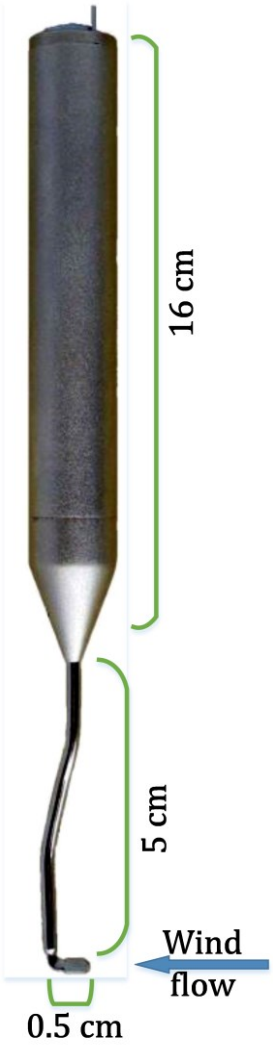

Figure 4.4: Cobra probe used for velocity measurements

4.3. *Building Model*

A geometric scale of 1:400 was selected for this study by considering the similarity parameters that must be satisfied when performing wind tunnel tests. A wooden model [25 cm (length) × 15 cm (width) × 1.5 cm (height)] was constructed in this scale - see Figure 4.5. A second roof height of 7.5 cm was also tested as a separate case.

The roof of the model was divided into 9 hypothetical "rectangles" of the same size, the centers of which are the 9 locations where the solar collector is considered to be. More specifically, locations 1-3 are located at the middle of the model from front to back and locations 4-6 and 7-9 are on the right and left of the middle locations respectively. Figure 4.6 shows the top view schematic of the building with the 9 testing positions spreaded uniformly on the roof area. In addition, equivalent full-scale dimensions are provided in the figure.

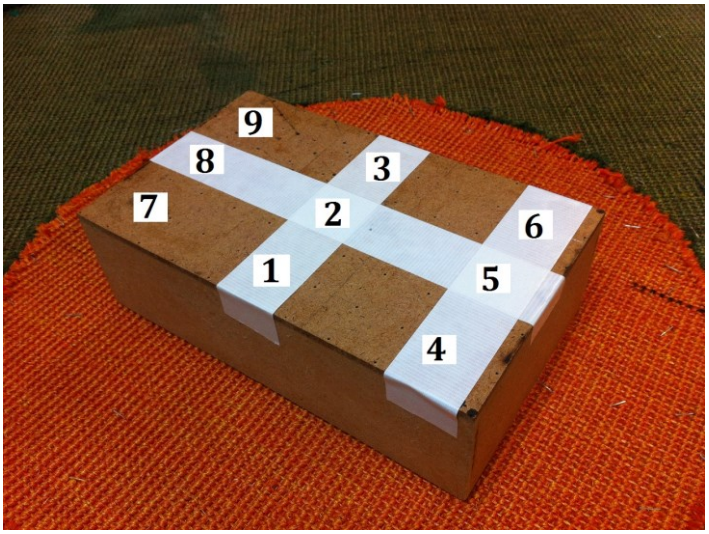

Figure 4.5: Building model at 1:400 scale

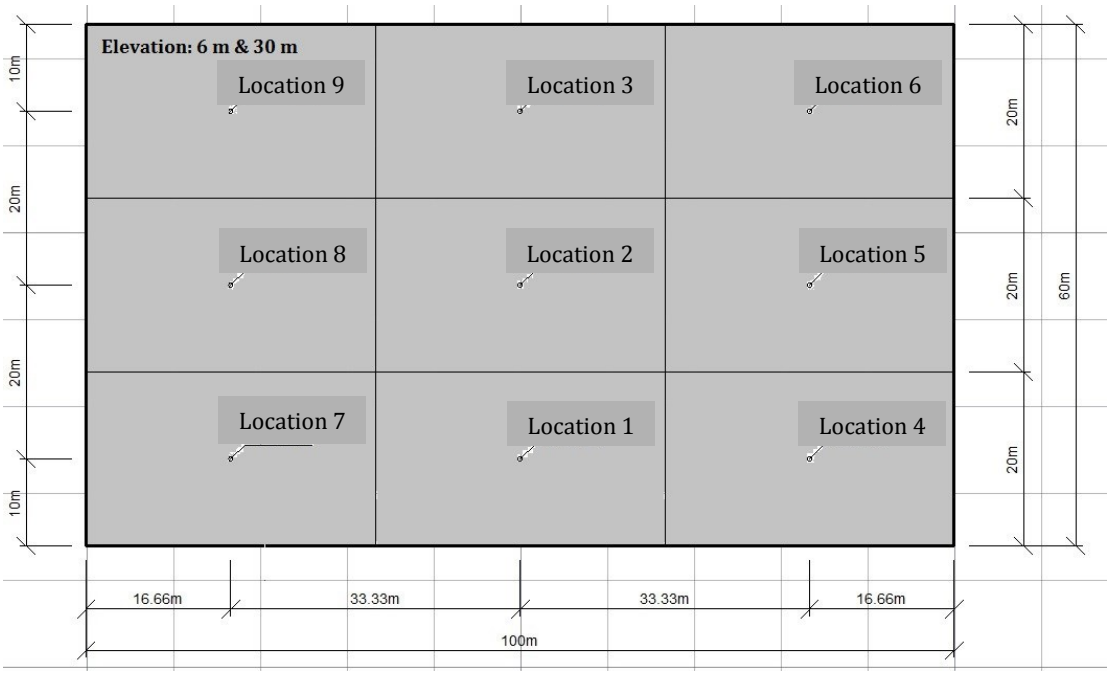

Figure 4.6: Top view of Figure 4.5 building model with full-scale equivalent dimensions

4.4. *Wind Tunnel Experiments*

In order to examine the variation of wind speed above the building roof, the building model (Figure 4.5) was placed on the turntable of the test section and oriented in the appropriate angle against the airflow. In most of the cases, different "bluff bodies" of hypothetical surrounding buildings were positioned strategically around the model. These "bluff bodies" and their purpose will be described in the equivalent section of each case. The Cobra probe was moved via the traversing system, which was presented in section 4.2, above location 1, at a height where a typical commercial solar collector would be located (0.5 cm above the model's roof, i.e. 2 m in full-scale). The gradient wind speed was 14 m/s and the flow was allowed for a couple of minutes to stabilize.

The experiments, included measurements of local wind velocity V_{loc} above locations 1-9. The velocity readings were done for 30 seconds each, at a sampling frequency of 1000 Hz. The experiments were carried out for 3 different angles of incident wind (0°, 45°, 90°) and for two different height configurations (*case 1*: 6 m roof height) (*case 2*: 30 m roof height). The model was hypothetically isolated in an open terrain setting. The schematic of the experiment is shown in Figure 4.7.

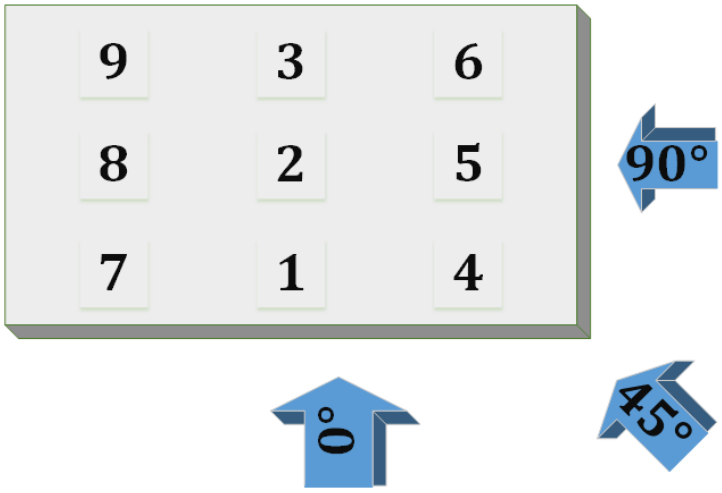

Figure 4.7: Cases 1, 2 – isolated model

❖ Cases with adjacent buildings

Since real buildings are in urban areas, it was recognized that the surroundings would have an important effect on the velocity distribution above the roof. Therefore, a series of configurations with surroundings were examined. Cases 3-17 can be categorized into groups based on the adjacent building(s) used in the experiment so that the local differences above the roof can be analyzed more explicitly. For this reason, the following sets of cases were created:

- Adjacent building height: 30 m *(Cases 3-7)*
- Adjacent building height: 178 m *(Cases 8-13)*
- Adjacent building height: 60 m & 90 m *(Cases 14-15)*
- Adjacent building height: Urban (*average building height*: 80 m) *(Cases 16-17)*

For Cases 3-7 a rectangular block (100 m × 26 m × 30 m) was used. The different setups are shown in Figure 4.8.

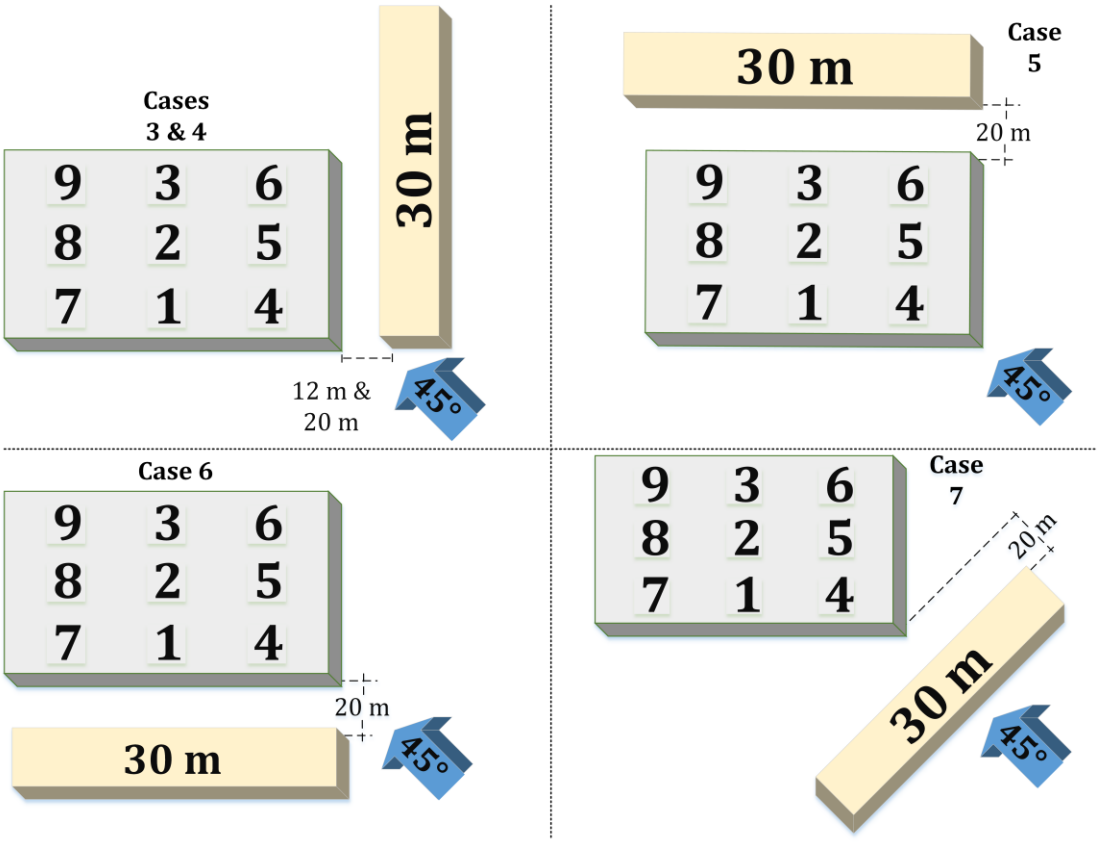

Figure 4.8: Setup configurations for Cases 3-7 with the use of a 30 m "bluff body" around the model

In cases 3 and 4 measurements were performed for the low model (6 m roof height) positioned on the turntable in such a way that the incidence angle of wind would be 45°. The rectangular block was positioned next to the right side of the model. For Case 3 the distance between the two bodies was 3 cm (12 m in full-scale, similar to an average 2-lane road with pavement on both sides. For Case 4

the size of the road was considerably larger. The distance between the two buildings was 5 cm (similar to a 4-lane road with pavement on both sides. In Case 5 the rectangular block was positioned 20 m away from the back of the low model (6 m roof height) and the wind incidence angle was 45°. In Case 6 the "bluff body" was located in the exact opposite position as in case 5 at the front of the model. Finally, in Case 7 the rectangular building model was positioned 20 m away from the front of the low model (6 m roof height) across location 4 and basically blocking the model almost completely from straight exposure to upcoming wind. The experiments were repeated for all positions.

A series of experiments was conducted (Cases 8-13) with the use of a very large "bluff body" of the following full-scale measurements: 133 m (length) × 79 m (width) × 178 m (height). The purpose of these experiments was to test the behavior of wind around a very large building, like the one that was used. The building model was positioned in key locations around the large building. For Cases 8-10 the high model was used (30 m roof height) and for Cases 11-13 the low model was used. (6 m roof height). All the different setups are shown in Figure 4.9.

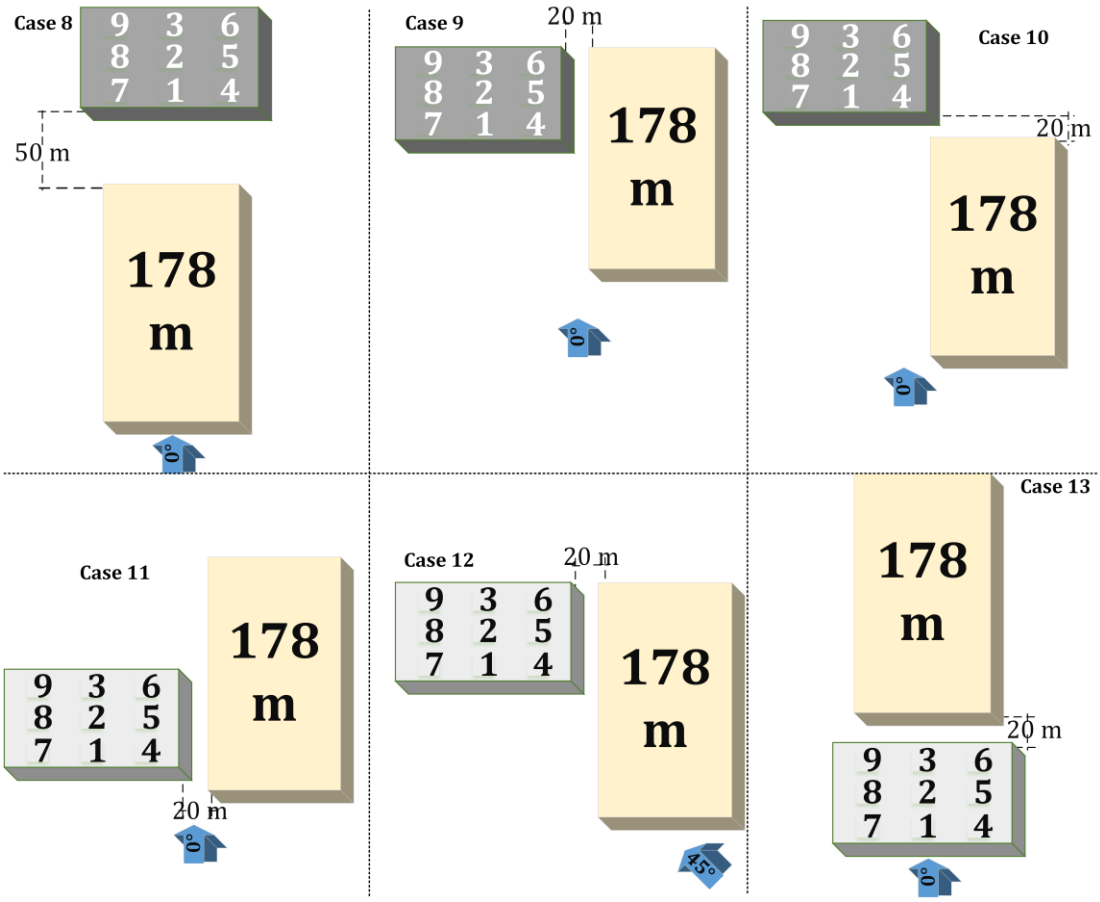

Figure 4.9: Setup configurations for Cases 8-13 with the use of a large, 178 m (height) "bluff body" around the model

More specifically, in Case 8 the high model (30 m roof height) was positioned 50 m away from the back side of the large building block and covered almost completely by it, relatively to the wind. In Case 9 the model was positioned 20 m away from the right side of the block and towards the back. In Case 10 the model was positioned at the far right back side of the large building, 20 m away. In all three cases with the high model the wind incidence angle was 0°.

As it was mentioned previously, in Cases 11-13, the low model was used. (6 m roof height). In Case 11 experiments were performed with the model placed 20 m (in full-scale) away from the large obstructing building, at its right side and towards the front. The wind incidence angle was 0°. Case 12 intended to check the formation of wind patterns on the roof of a building when a very large block is obstructing the wind flow completely. The large block was positioned 20 m (in full-scale) in front of the model and the wind incidence angle was 45°. Finally, in Case 13, the model was positioned right in front and 20 m (in full-scale) away from its larger counterpart.

Cases 14-15 was to examine the distribution of wind on the roof of the building model when the wind is obstructed by two higher buildings. For this purpose two new obstructing models were used. The first "bluff body" was (30 m × 30 m × 90 m) and the second (70 m × 60 m × 60 m). The high model (30 m roof height) was situated 40 m behind them and in between them in a 0° orientation towards the wind. In Case 15 the model was oriented in a 45° fashion towards the wind. The schematic of both these experiments is shown in Figure 4.10.

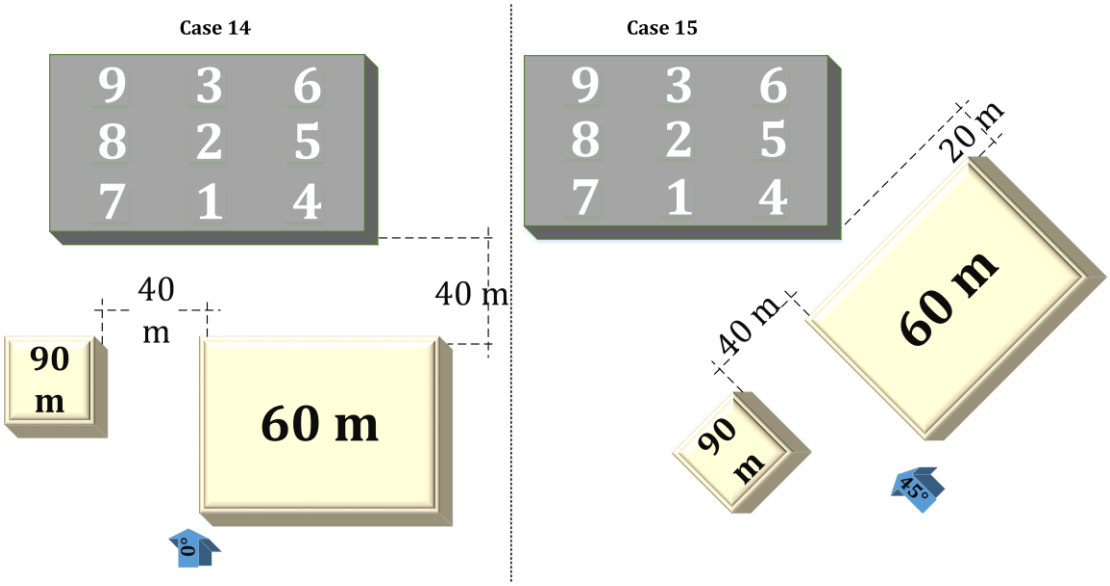

Figure 4.10: Setup configurations for Cases 14-15 with the use of two "bluff bodies" (90 m & 60 m) around the model

In addition to the previous configurations, the interaction of actual city environments to the wind distributions on the roof of the test model was examined. For this purpose, the high model (30 m roof height) was selected. In Case 16 the model is situated around buildings of similar height or slightly higher. The schematic of the experiment is shown in Figure 4.11. In the final case of this series of experiments the high model is situated inside a city with very high buildings. The schematic of the experiment is shown in Figure 4.12.

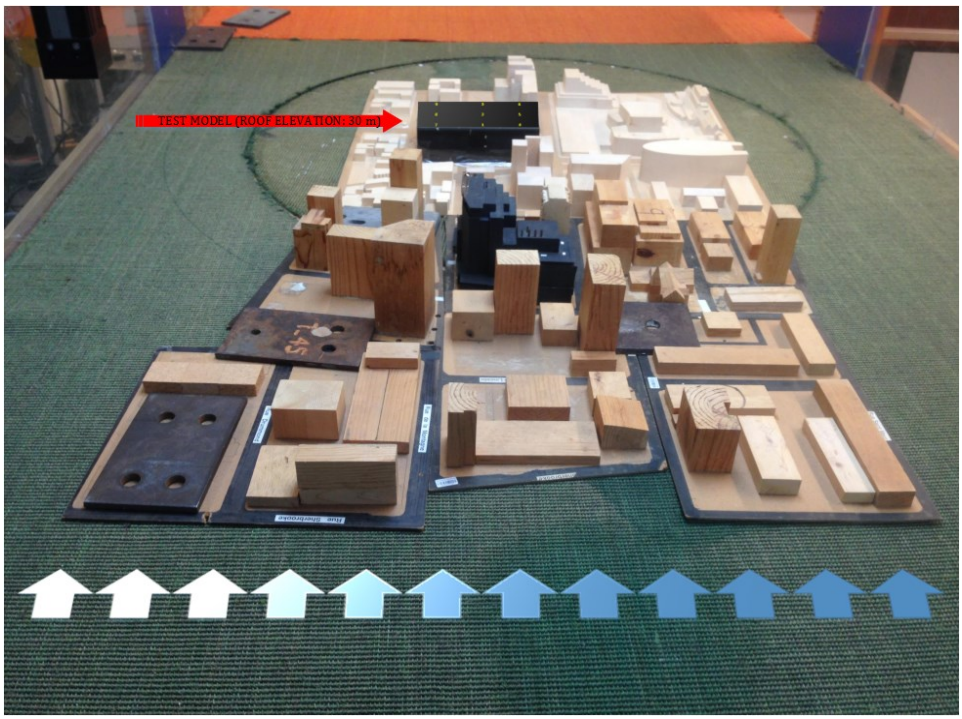

Figure 4.11: Case 16 – high model with city surroundings

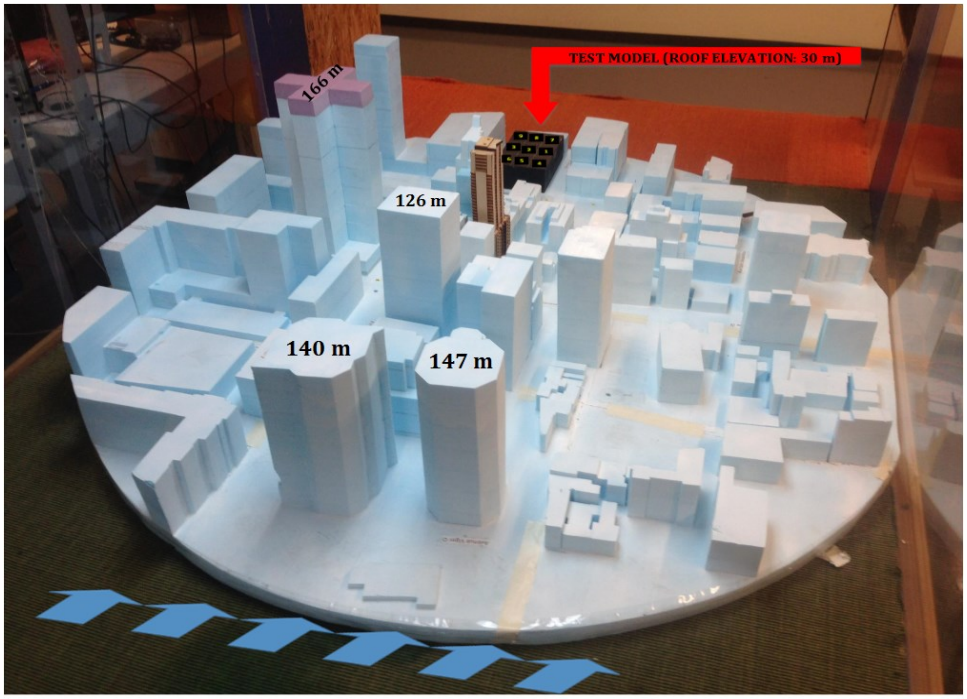

Figure 4.12: Case 17 – high model in downtown Montreal

Chapter 5 – EXPERIMENTAL RESULTS & DISCUSSION

The objective of this study was to investigate the effects of wind velocity distributions on a solar collector mounted on a building roof and to show the importance in adopting more accurate and location-specified distributions for analysis as opposed to a single, uniform wind velocity profile.

Several experiments were repeated three times to identify the error in the measurements. By normalizing the standard deviation of each measurement with the mean value above each location, the average error was calculated to be around 5.8%. Local velocities are presented in the form of contours of local velocity coefficients, defined as the ratio of the local velocity V_{loc} over the gradient wind velocity V_g.

5.1. *Isolated Building Cases*

Figure 5.1 shows the contour plots of normalized wind velocity for the three different wind directions tested for Case 1 (*building height: 6 m*).

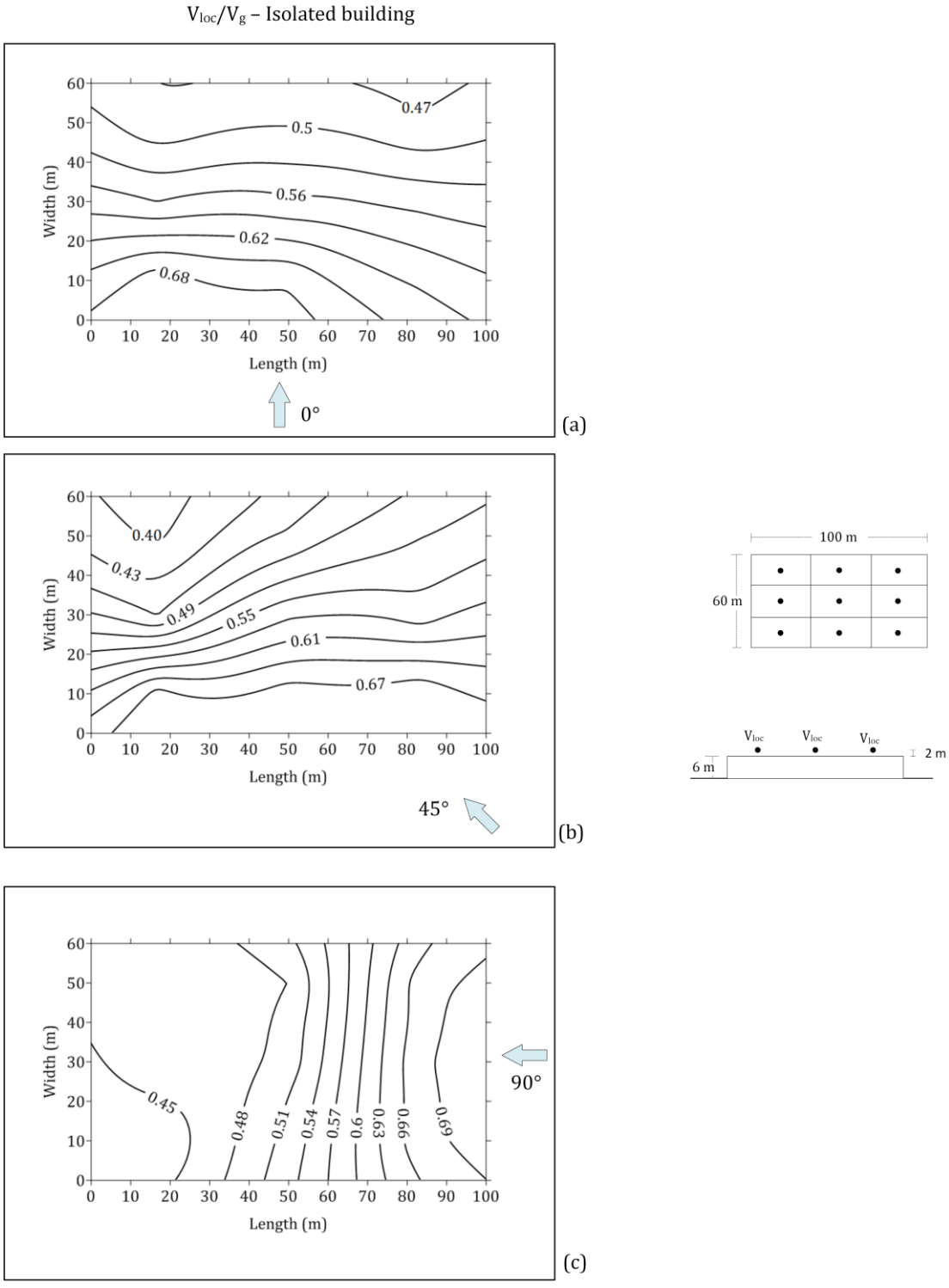

Figure 5.1: *V_{loc}/V_g* contours for: (a) 0°, (b) 45° and (c) 90° angle of attack (Case 1)

In general, wind velocities on the roof of the isolated building are higher in the windward than the leeward area. This is due to flow separation and acceleration at the front edges. The highest velocity differences between the front and back area were measured in the case of 45° wind direction. The ratio between the maximum and minimum velocities measured above the roof, for 45° angle of incidence, was 1.75. Figure 5.2 shows this ratio of maximum over minimum local velocity above the roof of the building for the three wind incidence angles tested. More specifically, the 90° incidence angle causes a ratio of about 1.6 whereas this ratio drops to 1.5 for the 0° angle of incidence.

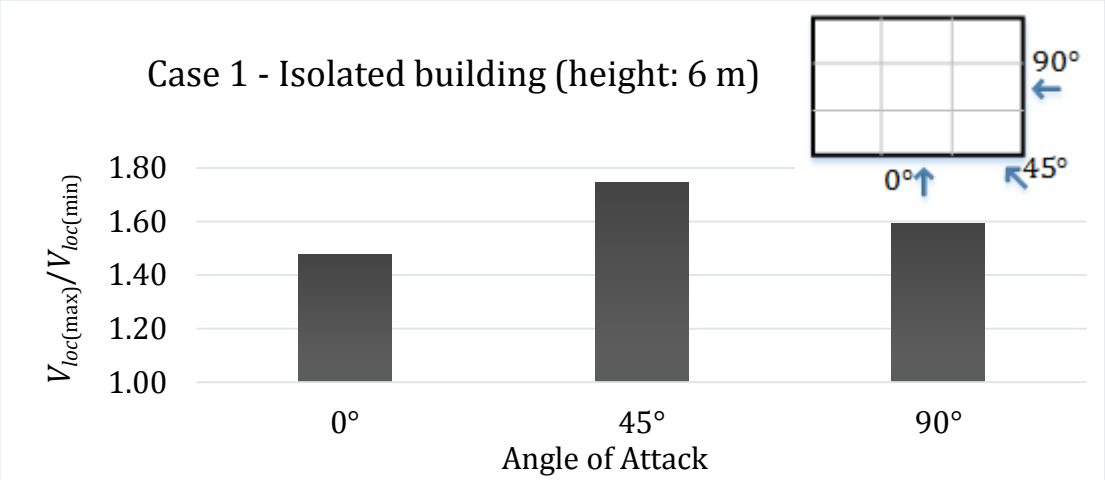

Figure 5.2: Ratio of maximum over minimum local velocity above roof for 0°, 45° and 90° angle of attack (Case 1)

Figure 5.3 shows contour plots of local velocity coefficients for the three different wind directions tested for Case 2 (*building height: 30 m*).

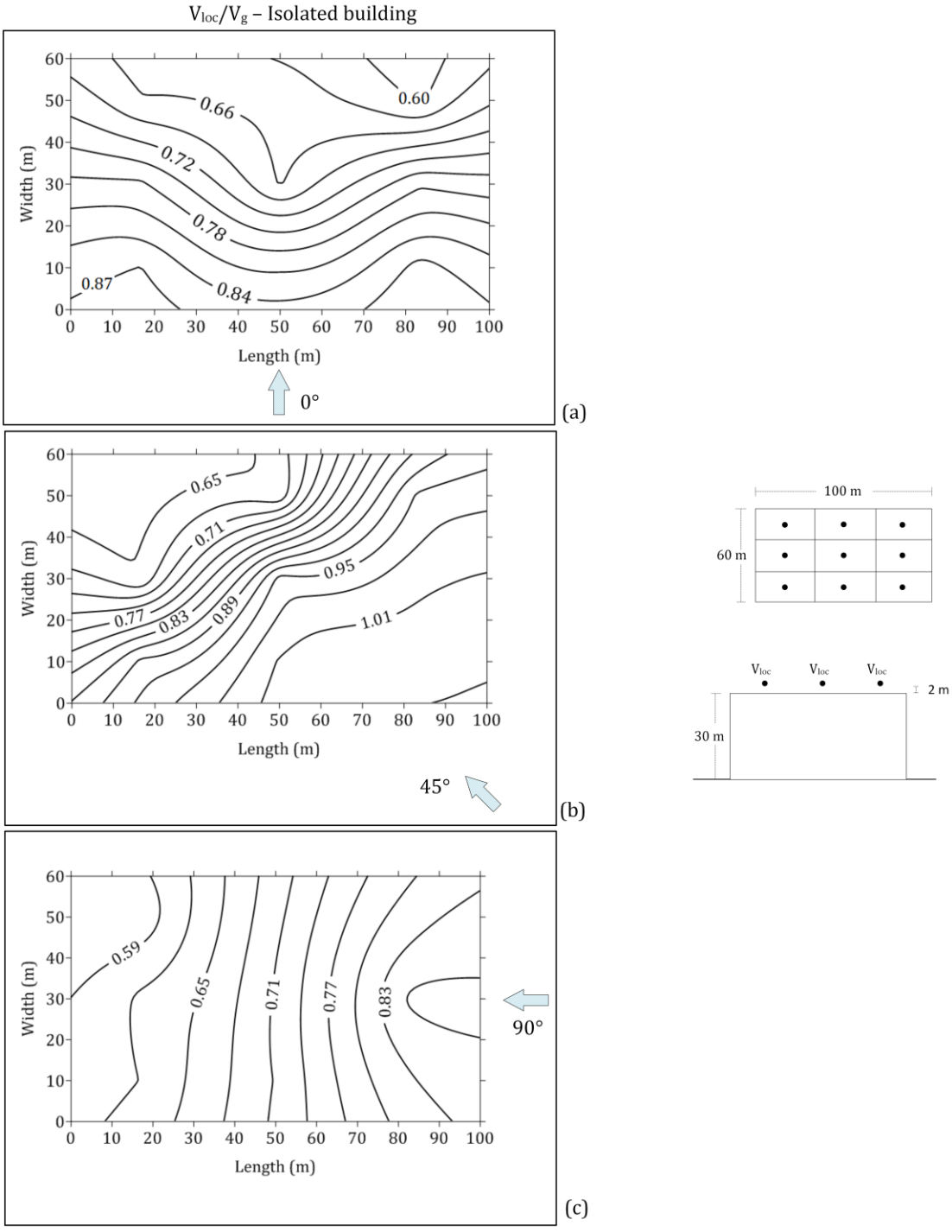

Figure 5.3: V_{loc}/V_g contours for: (a) 0°, (b) 45° and (c) 90° angle of attack (Case 2)

Similar differences are observed in this case, where the building is 5 times higher. There is a general trend on the velocity coefficients in Case 2 being, on average, about 20% to 30% higher than in Case 1. This can be explained by the fact that the measurement was performed at 32 m (whereas in Case 1 it was at 8 m) where the magnitude of the velocities is increased (Figure 2.1). In the case of 45° the velocity measured at a windward location was as high as the gradient velocity. This can be attributed to the acceleration caused at the edges of the building roof. Nonetheless, the variations between locations remain relatively similar to Case 1. Figure 5.4 shows the ratio of maximum over minimum local velocity above the roof of the building for the three angles of incidence that were

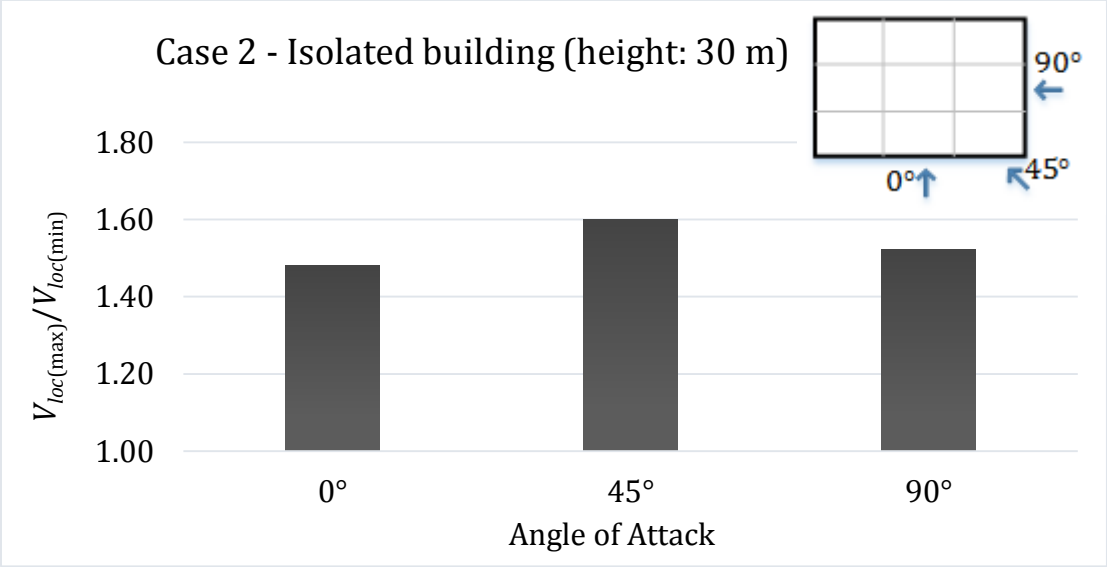

Figure 5.4: Ratio of maximum over minimum local velocity above roof for 0°, 45° and 90° angle of attack (Case 2)

tested, similar to Figure 5.2. For wind directions 0°, 45° and 90°, the local velocity ratios of maximum over minimum were 1.48, 1.60 and 1.52 respectively.

5.2. *Cases with Adjacent Buildings*

Mean wind speed that is reaching any building in a developed district is expected to be lower than what it would be if it reached an isolated building without obstacles. This phenomenon was verified during the experiments that were performed for cases of a building surrounded by different kinds of adjacent structures (Cases 3-17). However, the presence of buildings in the close vicinity of the target building could result in higher than expected local velocities in certain areas of the roof. This is due to complex phenomena such as down-washing and wind channelling that were discussed in section 2.1.

From the first group (adjacent building height: 30 m) the setup that produced the higher local differences above the roof of the building was Case 7, where the obstructing structure was positioned across the front-right corner of the building. Figure 5.5 presents the contours of the normalized velocity V_{loc}/V_g above the roof of the 6 m high building.

It is noticeable that the wind flow is blocked by the 30 m building and thus, the wind velocities at the windward area (locations 1, 4, 5) are lower than the leeward area (locations 6, 3, 9, 8). This is due to the separation of the flow that happens at the front edges of the 30 m building that is reattaching close to the leeward area of the target building, causing turbulence. The ratio of maximum over minimum local velocity above the roof of the building was found to be 2.7.

V_{loc}/V_g

- *Test building height:* 6 m
- *Adjacent buildings height:* 30 m

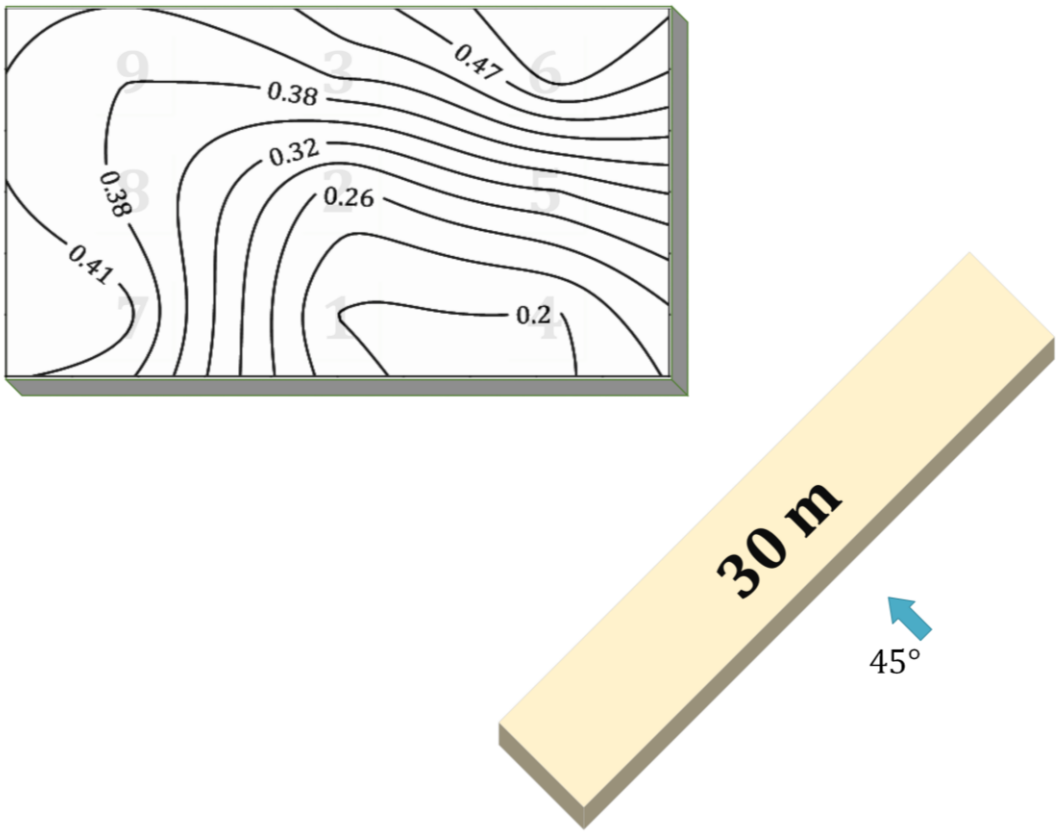

Figure 5.5: V_{loc}/V_g contours for 45° (Case 7)

From the second group (adjacent building height: 178 m) the setup that produced the higher local differences above the roof of the building was Case 13. Figure 5.6 shows the contours of the normalized velocity V_{loc}/V_g above the roof of the 6 m high building.

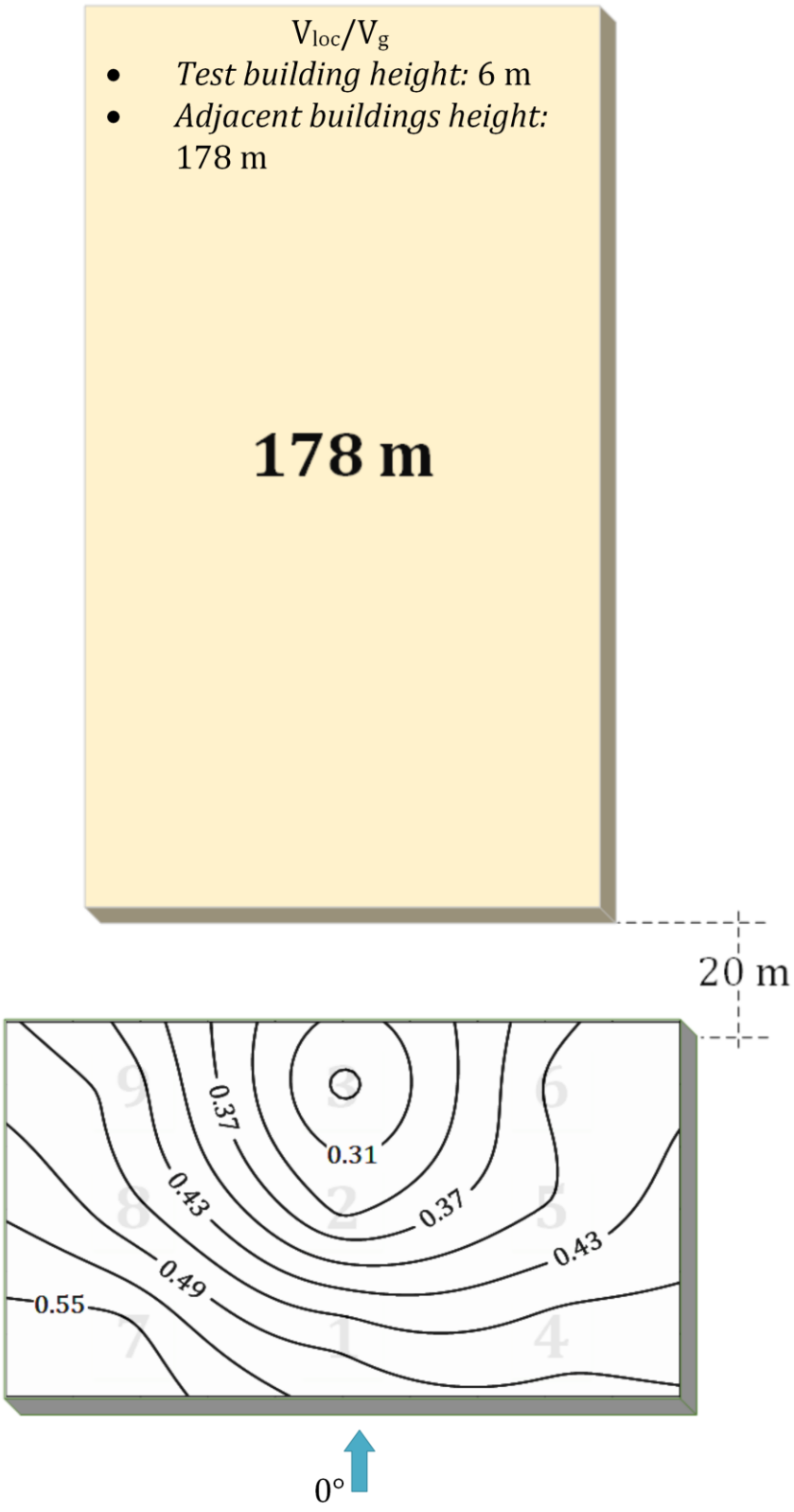

Figure 5.6: V_{loc}/V_g contours for 0° (Case 13)

In this situation, the wind flow first comes in contact with the target building but the interaction of the very high structure at the back changes the normal flow patterns on top of the roof. As explained, in section 2.3, wind is diverted by the higher structure and washed downwards onto the roof of the smaller structure. The lowest velocity coefficients were measured at the leeward area of the roof (locations 3, 6, 9), the area closer to the large building, and the highest ones were measured at the front of the building (locations 7, 1, 4). The ratio of maximum over minimum local velocity above the roof of the building was found to be 2.1.

Figure 5.7 shows the contours of the normalized velocity V_{loc}/V_g above the roof of the 30 m high building for Case 15. A 60 m obstructing structure was placed across the front-right corner of the target building and another one, 90 m high, was at a close proximity and parallel to it. The velocity coefficients above the roof of the building are considerably minimized in general due to the size of the buildings that block the flow. However, a channeling effect (section 2.4) is observed at this situation, with the highest values appearing at the locations close to the opening between the two obstructing buildings (locations 7, 8). The ratio of maximum over minimum local velocity above the roof of the building was found to be 2.3.

V_{loc}/V_g

- *Test building height:* 30 m
- *Adjacent buildings height:* 60 m & 90 m

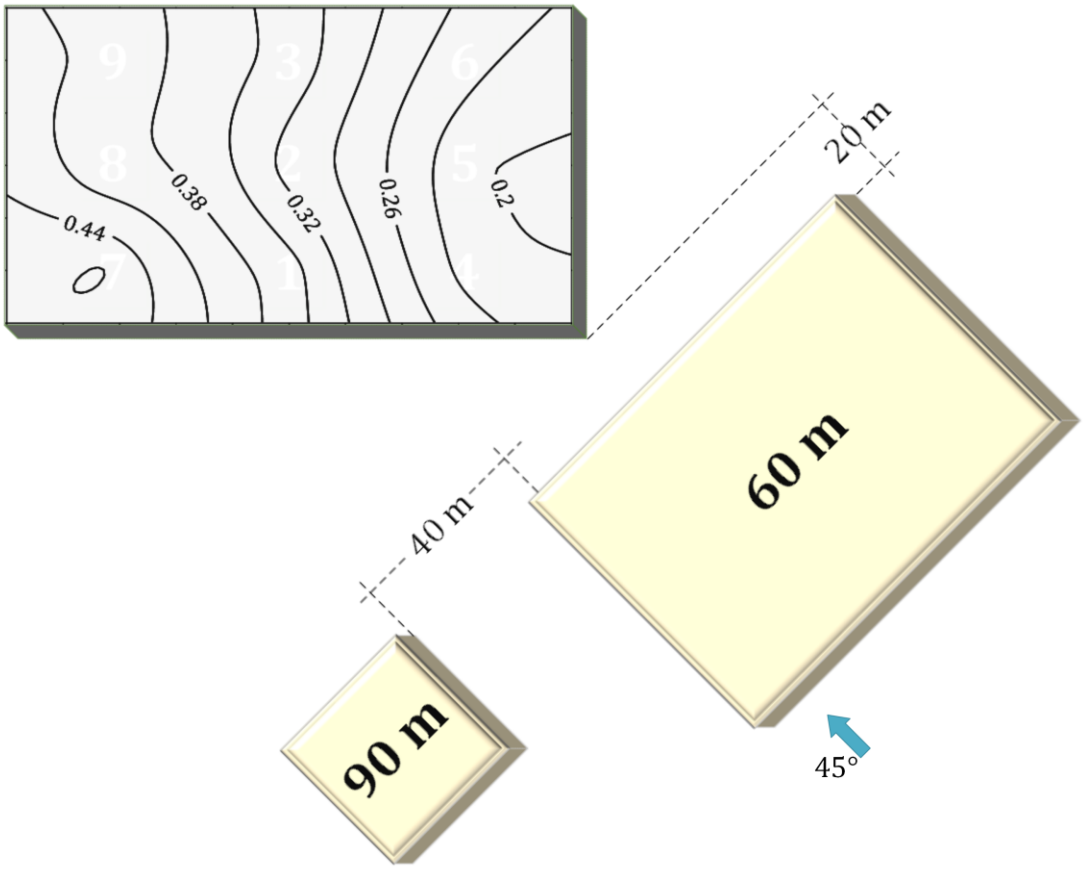

Figure 5.7: V_{loc}/V_g contours for 45° (Case 15)

Finally, regarding the urban scenarios tested, the velocities above the roof of the target building appeared to be very low compared to any other case tested. As mentioned previously, the complexity of the city creates a lot of wind phenomena resulting to lower velocity values atop a building roof located at the center of the city.

Figure 5.8 shows the contours of the normalized velocity V_{loc}/V_g above the roof of the 30 m high building for Case 17. The velocity coefficients showed smaller differences above the roof.

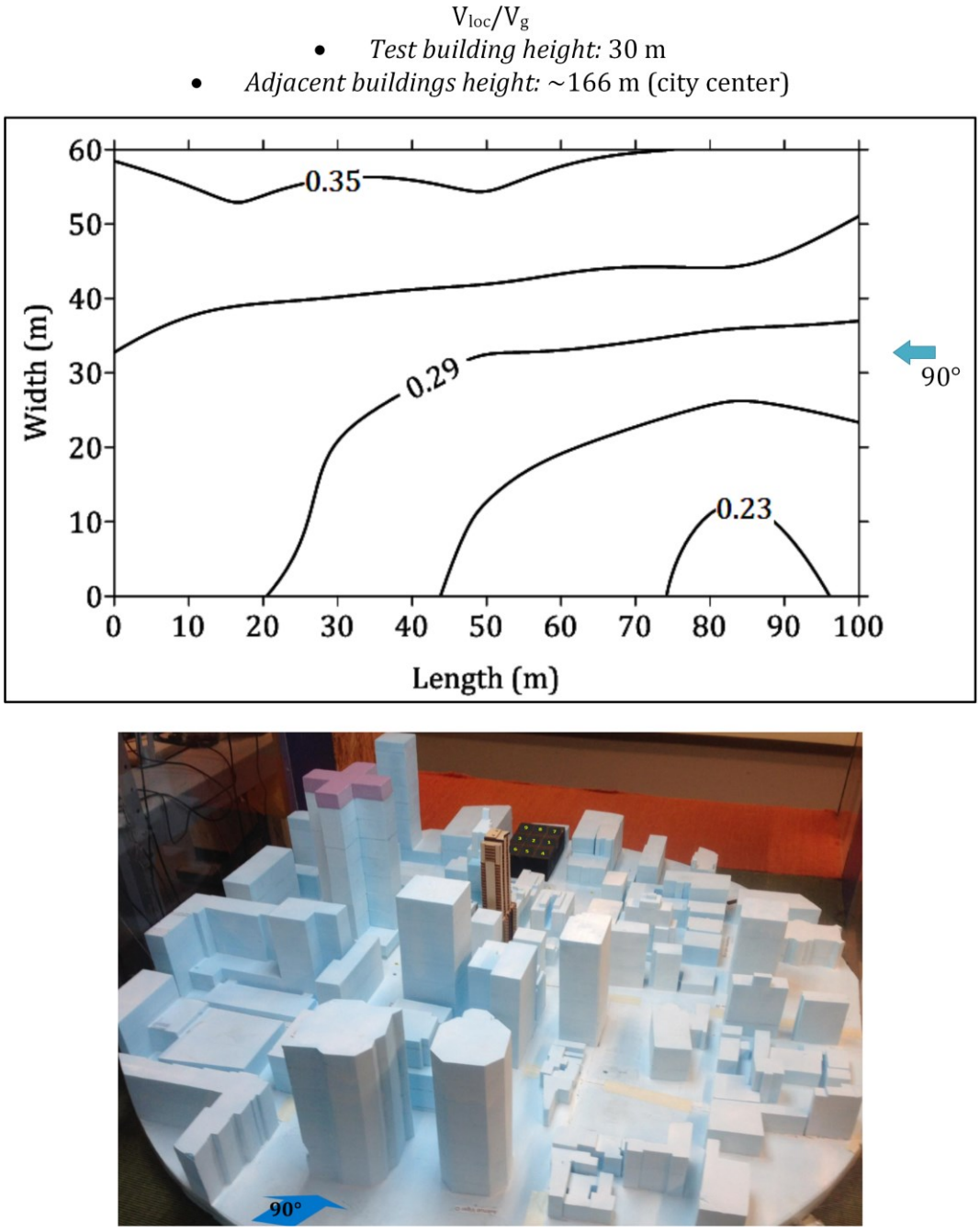

Figure 5.8: V_{loc}/V_g contours for 90° (Case 17)

The ratio of maximum over minimum local velocity above the roof of the building was found to be 1.6.

There is a trend of the velocity coefficients in the cases with the adjacent buildings being, on average, 30% to 50% lower than the cases with the isolated buildings. This quantifies the impact of adjacent buildings on the wind flow above the target building. Figure 5.9 shows the average velocities coefficients above the roof of the building for all the cases studied.

The roof locations that are the closest to the structures that block the wind flow suffer the lowest velocities of all other parts of the roof.

For analysis using full-scale velocities, the local velocity V_{loc} for any location above the roof of the building can be calculated by multiplying the corresponding velocity coefficient with the gradient velocity.

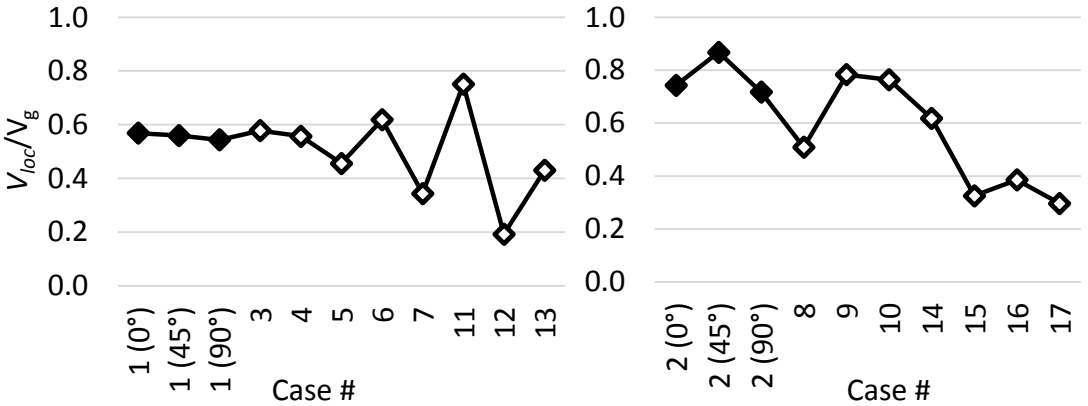

Figure 5.9: Average velocity coefficients above roof for Cases 1-17

In sections 5.1 and 5.2, a selection of the most critical cases that were created for experimentation in the wind tunnel, were presented. Additional cases are in the Appendix.

5.3. *Calculation of Wind-Induced Convective Heat Transfer Coefficients*

During the course of this study the wind-induced convective heat transfer coefficient h_w was calculated numerically. The local velocities measured above the roof of the building model were applied into analytical models in order to calculate h_w. As explained in Chapter 3, there is a variety of equations for the numerical calculation of h_w. This creates dilemmas for design professionals prior to selecting the most appropriate model. In the present study, the model developed with experimental parameters similar to those used in the present study was selected. Sharples and Charlesworth (1998) and Emmel, et al. (2007) provide direction specific h_w-V_{loc} equations. These are plotted and compared in Figure 5.10. As mentioned in section 3.3, the CFD study by Emmel, et al. (2007) clearly underestimates the wind-induced convective heat transfer coefficient compared to the other studies that were described in Chapter 3. Furthermore, it is known by previous studies (Sharples, 1984) that when the wind velocity is zero, natural convection phenomena are dominant. This is not mirrored in the power

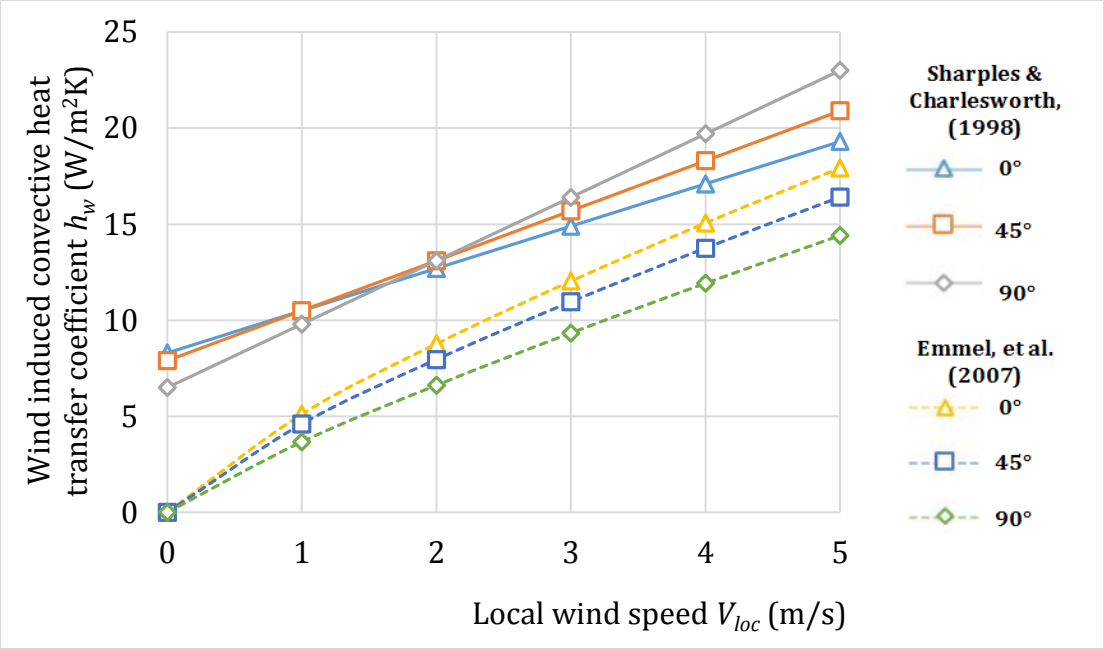

Figure 5.10: Comparison of direction specific h_w-V_{loc} equations from (Emmel, et al., 2007) and (Sharples & Charlesworth, 1998)

relations of Emmel, et al. (2007). Equations (3-7)-(3-14) by Sharples and Charlesworth (1998) produce results that lie in between the range over which the results of other studies vary. These equations were developed for a solar collector tilted at 45° on top of a building with similar height dimensions with the building of this study and exposed in open terrain. Since they are functions of wind incidence, it is expected to provide the most accurate results. Also they are the most detailed and specific to different wind directions, making them more accurate than a single global equation for all directions. For these reasons, these equations were found to be the most practical to adopt for the current study. For all 9 locations above the roof (as designated in section 4.3) h_w was calculated by using the respective value of V_{loc} in equations (3-7)-(3-14) according to the different wind directions.

Chapter 6 – SOLAR COLLECTOR PERFORMANCE

The purpose of this chapter is to examine the effects of wind velocity distributions on a flat-plate solar collector mounted on a building roof and to illustrate the differences in thermal energy gains between possible installing locations.

A detailed analytical model of the solar collector's performance is used to calculate the thermal energy gains and efficiency for all nine locations above the roof. The computations are performed for hypothetical windy days with different gradient velocities and for a typical day in Montreal.

6.1. *Thermal Modelling*

Energy balance equations can be employed to estimate the thermal performance of an N-glazed solar collector. The process used in this study is based on the detailed computation of Duffie and Beckman (2006). In this section, a heat transfer model of a solar-thermal, single glazed (N = 1), water-based collector is presented. Similar equations can be used for any additional glass covers.

Figure 6.1 shows the cross section of a single-glazed flat-plate solar water collector. A number of assumptions were made for the numerical solution of the model: The amount of solar energy absorbed by the glass cover of the collector is negligible. Additionally, the glass cover is opaque to infrared radiation and the heat flow through it is one-dimensional. Finally, it is assumed that the ambient temperature is the same at the front and the back of the collector.

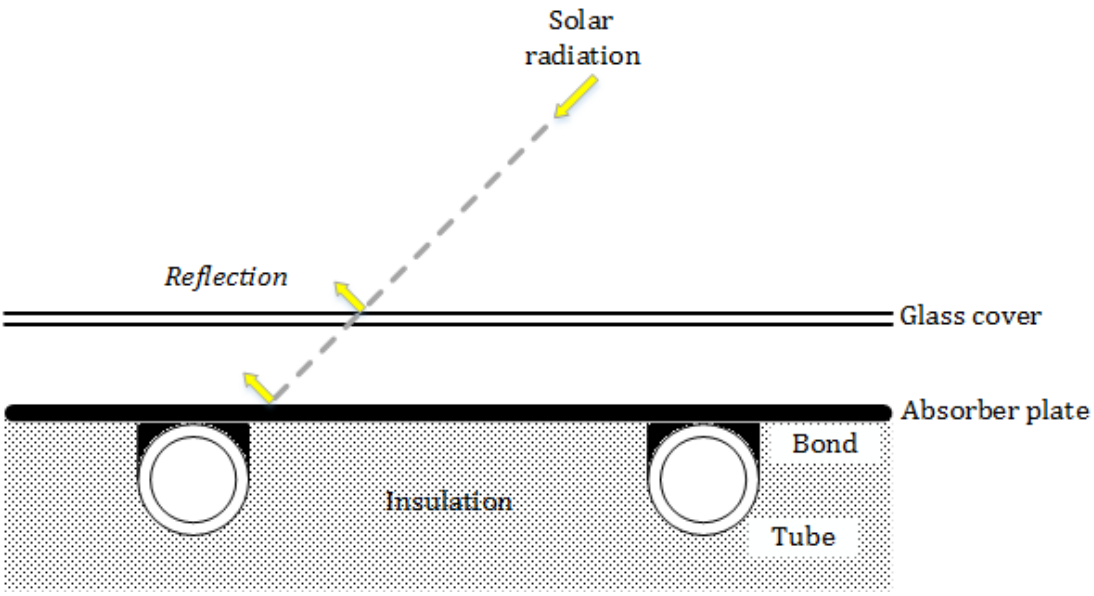

Figure 6.1: Cross section of a flat-plate solar collector (single-glazed)

The thermal performance of the solar collector can be expressed as the thermal energy gain q_u (W/m^2) per collector area A_c:

$$q_u = F_R[S - U_L(T_i - T_a)] \quad \textbf{(6-1)}$$

where T_i and T_a are the inlet fluid and ambient temperatures respectively (K); F_R is the collector heat removal factor; S is the solar radiation absorbed by the collector plate and finally U_L is the overall collector loss coefficient. The calculation of these three variables will be carried out in this section.

Furthermore, the efficiency of the collector η, which has been evaluated for the various cases examined, is defined as the ratio of the thermal energy gains over the total incident solar radiation:

$$\eta = \frac{q_u}{I_T} \quad \textbf{(6-2)}$$

The overall loss coefficient for a solar collector U_L consists of all the losses that take place during the solar collector's use; namely the top-loss coefficient U_t, the bottom-loss coefficient U_b and the edge-loss coefficient U_e.

$$U_L = U_t + U_b + U_e \quad \textbf{(6-3)}$$

❖ *Top-loss coefficient U_t*

The top-loss coefficient expresses the energy lost through the top cover of the solar collector due to convection and radiation between the glazing and the absorber plate. In this model, an empirical equation developed by Klein (1979) is used:

$$U_t = \left(\frac{N}{\frac{C}{T_{pm}}\left[\frac{(T_{pm}-T_a)}{(N+f)}\right]^e} + \frac{1}{h_w}\right)^{-1} + \frac{\sigma(T_{pm}+T_\alpha)({T_{pm}}^2+{T_\alpha}^2)}{\frac{1}{\varepsilon_p+0.00591Nh_w}+\frac{2N+f-1+0.133\varepsilon_p}{\varepsilon_g}-N} \quad \textbf{(6-4)}$$

where:

- N is number of glass covers;
- ε_g is the glass emittance;
- ε_p the plate emittance;
- T_{pm} is the mean-plate temperature (K);
- h_w the wind-induced convective heat transfer coefficient (calculated with the methods of section 5.3)(W/m^{2}K);
- $f = (1 + 0.089h_w - 0.1166h_w\varepsilon_p)(1 + 0.07866N)$ the wind factor (W/m^{2}K);
- $C = 520(1 - 0.000051\beta_w^2)$ the collector tilt factor (deg);
- β_w the collector tilt (deg);

- $e = 0.430(1 - \frac{100}{T_{pm}})$ the mean-plate temperature factor (K)
- $\sigma = 5.67 * 10^{-8}\, W/_{m^2 K^4}$ the Stefan-Boltzmann constant.

❖ *Bottom-loss coefficient U_b*

The bottom loss coefficient expresses the energy lost from the back of the collector and it is a function of the collector's back insulation thermal conductivity k_i (W/m*K) and the back insulation thickness L_t (m):

$$U_b = \frac{k_i}{L_t} \qquad \textbf{(6-5)}$$

❖ *Edge-loss coefficient U_e*

The edge-loss coefficient is the energy lost from the edges of the collector. It is safe to assume that edge insulation has the same thickness as bottom insulation and therefore the losses from the edges can be measured by using one-dimensional heat flow around the perimeter of the whole system. The coefficient is then a function of the edge insulation thickness e_t (m) and the collector thickness C_t (m):

$$U_e = \frac{C_t \left(\frac{k_i}{e_t}\right) P}{A_c} \qquad \textbf{(6-6)}$$

where:

- P is the collector perimeter (m);
- A_c the collector area (m^2)

The collector's heat removal factor F_R is equivalent to the effectiveness of a conventional heat exchanger defined as the ratio of the heat transfer that is actually taking place over the maximum possible heat transfer that would happen only if the whole collector surface were at the fluid inlet temperature T_i. The heat removal factor is a function of the collector efficiency factor F'_c and collector flow factor F''_c.

$$F_R = F'_c F''_c \qquad \textbf{(6-7)}$$

❖ *Collector efficiency factor F'_c*

It is essentially a constant for any collector design and fluid flow rate. The collector efficiency factor represents the importance of bond conductance in the accurate description of a collector's performance:

$$F'_c = \frac{\frac{1}{U_L}}{W_p\left[\frac{1}{C_b} + \frac{1}{\pi D_p h_{fi}} + \frac{1}{U_L\left[D_p + \left(W_p - D_p\right)F_c\right]}\right]} \qquad \textbf{(6-8)}$$

where:

- C_b is the bond conductance (W/m*K);
- h_{fi} the heat-transfer coefficient inside the tubes (W/m^2K);

- F_c is the fin efficiency factor:

  In order to calculate the temperature distribution between two tubes it can be assumed that the temperature gradient in the direction of the flow is not significant. Then the area between the middle boundary that separates the tubes and their base can be considered a fin problem:

$$F_c = \frac{\tanh[(\frac{U_L}{k_p \delta_p})^{0.5} \frac{(W_p - D_p)}{2}]}{(\frac{U_L}{k_p \delta_p})^{0.5} \frac{(W_p - D_p)}{2}} \quad \textbf{(6-9)}$$

  where:

  - δ_p is the plate thickness (m);
  - k_p the plate thermal conductivity (W/m*K);
  - W_p the tube spacing (m);
  - D_p the tube inside diameter (m).

❖ *Collector flow factor F''$_c$*

$$F''_c = \frac{m_w C_p}{A_c U_L F'_c} [1 - \exp\left(\frac{-A_c U_L F'_c}{m_w C_p}\right)] \quad \textbf{(6-10)}$$

where:

- C_p is the specific heat of water (kJ/kg*K);

- m_w the water flow rate (kg/s).

The solar energy S that is absorbed by the collector absorber plate is given by:

$$S = I_b R_b (\tau\alpha)_b + I_d (\tau\alpha)_d \left(\frac{1+\cos\beta_w}{2}\right) + \rho_g I_g (\tau\alpha)_g \frac{1-\cos\beta_w}{2} \qquad \textbf{(6-11)}$$

where:

- I_b is the beam solar radiation (W/m^2);
- I_d the diffuse solar radiation (W/m^2);
- I_g the ground-reflected solar radiation (W/m^2);
- $\frac{1+\cos\beta_w}{2}$ and $\frac{1-\cos\beta_w}{2}$ the view factors from the collector to the sky and the ground respectively;
- $(\tau\alpha)_n$ the angular dependence of $(\tau\alpha)$. It can be found from the properties of the cover and the absorber (Duffie & Beckman, 2006);
- τ is the solar transmittance of the cover;
- α the solar absorptance of the plate.

With the help of equations (6-3), (6-7) and (6-11) the useful energy gain q_u per collector area A_c can be calculated through equation (6-1).

The parameters mentioned above that were used and remained constant throughout the calculations are provided in Table 6.1:

Table 6.1: Constant parameters for solar collector performance modelling

Perimeter: $P = 6.92\ m$	Back insulation thickness: $L_t = 0.05\ m$
Area of collector: $A_c = 2.72\ m^2$	Edge insulation thickness: $e_t = 0.05\ m$
Number of glass covers: $N = 1$	Collector thickness: $C_t = 0.1\ m$
Plate emittance: $\varepsilon_p = 0.95$	Plate thermal conductivity (copper): $\varepsilon_g = 385\ {}^{W}/_{m*K}$
Plate thickness: $\delta_p = 0.88\ m$	Mean-plate temperature: $T_{pm} = 373.15\ K$
Glass emittance: $\varepsilon_g = 0.88$	Inlet fluid temperature: $T_i = 303.15\ K$
Collector tilt: $\beta_w = 45°$	Insulation thermal conductivity: $k_i = 0.045\ {}^{W}/_{m*K}$
Tube spacing: $W_p = 0.15\ m$	Inside tube diameter: $D_p = 0.01\ m$
Heat-transfer coefficient inside tubes: $h_{fi} = 300\ {}^{W}/_{m^2K}$	Bond conductance: $C_b = \infty$
Water flow rate: $m_w = 0.03\ {}^{kg}/_{s}$	Specific heat of water: $C_p = 4190\ {}^{kJ}/_{kg*K}$

6.2. *Thermal Performance of the Solar Collector*

Location-depending convective heat transfer coefficient h_w (see section 5.3) calculated for different local velocities V_{loc} and directional distributions were applied to the thermal model (described by section 6.1). Daily thermal energy gains q_u (W/m^2) and efficiency η of the solar collector (for each of the nine locations -see section 4.3-), were evaluated by using the model in order to quantify the effects of wind convection above different parts of the roof. The performance of the solar collector was calculated for all the cases that were described in section 4.4. However, in this section only the most important cases in terms of differences calculated above roof locations will be presented.

The solar conditions selected were those of a typical sunny day with total solar radiation (I_T) peaking at 1:00 pm at $I_{T(max)}$ = 850 W/m^2. The values of solar radiation were calculated with the use of a typical meteorological weather file for Montreal in EnergyPlus Simulation Software (U.S. Department of Energy, 2014). The ambient temperature was assumed to be T_a = 20 °C, typical Montreal summer conditions. These conditions remain the same throughout this study for all the cases that will be presented. The wind velocity, and as a result the wind-induced convective heat transfer coefficient, are the only parameters changing in every given time-step.

Figure 6.2 presents the total daily thermal energy gains of the collector and Figure 6.3 the equivalent daily efficiency for a very windy day. It is assumed that the incident angle of the wind velocity is 0° and that the gradient velocity is V_g = 40 m/s.

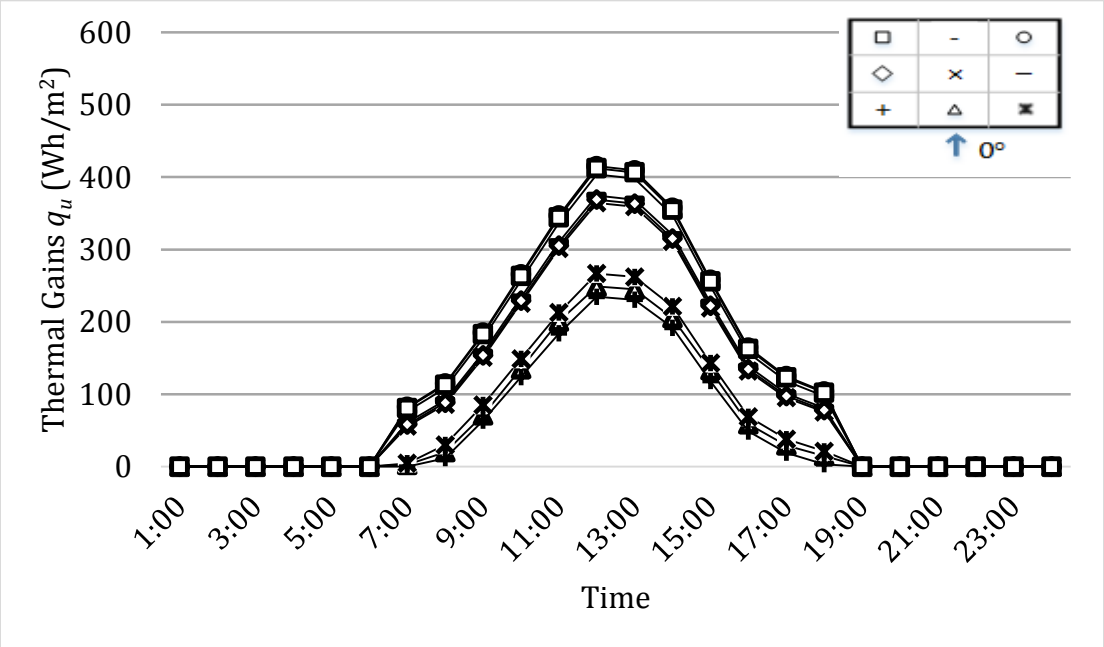

Figure 6.2: Thermal energy gains during a very windy day (Case 1 / 0°)

With this gradient velocity, the local wind velocities at full-scale above the building roof average around 13-14 m/s, values that very often occur in windy days in Montreal (e.g.: November 1st 2013). In Figure 6.2 the thermal gains above all nine locations are depicted. However, starting from Figure 6.3 only data for the two critical locations are presented for reasons of clarity.

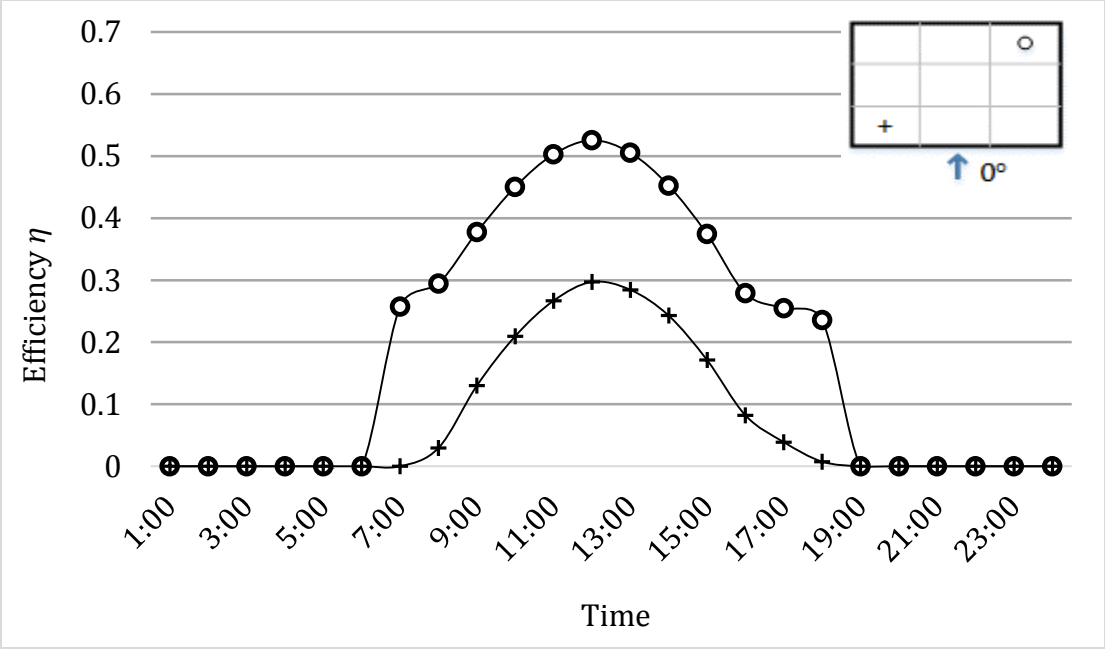

Figure 6.3: Solar collector efficiency during a very windy day (Case 1 / 0°)

As seen in Figure 6.2, the windward areas above the roof are places where the largest amount of cooling occurs. However, the best locations to install a solar collector are the leeward areas, i.e. the locations at the back of the roof. This agrees with the projection of section 5.1 that highlighted these areas as "high-wind" and "low-wind" locations. More specifically, the ratio of maximum (location 6) over minimum (location 7) daily thermal energy gains (or efficiency) for a solar collector is 2.30. Similar results are visible in the 45° angle of attack in Figure 6.4 and Figure 6.5. The ratio of maximum (location 9) over minimum (location 4) daily thermal energy gains (or efficiency) for a solar collector is 2.36.

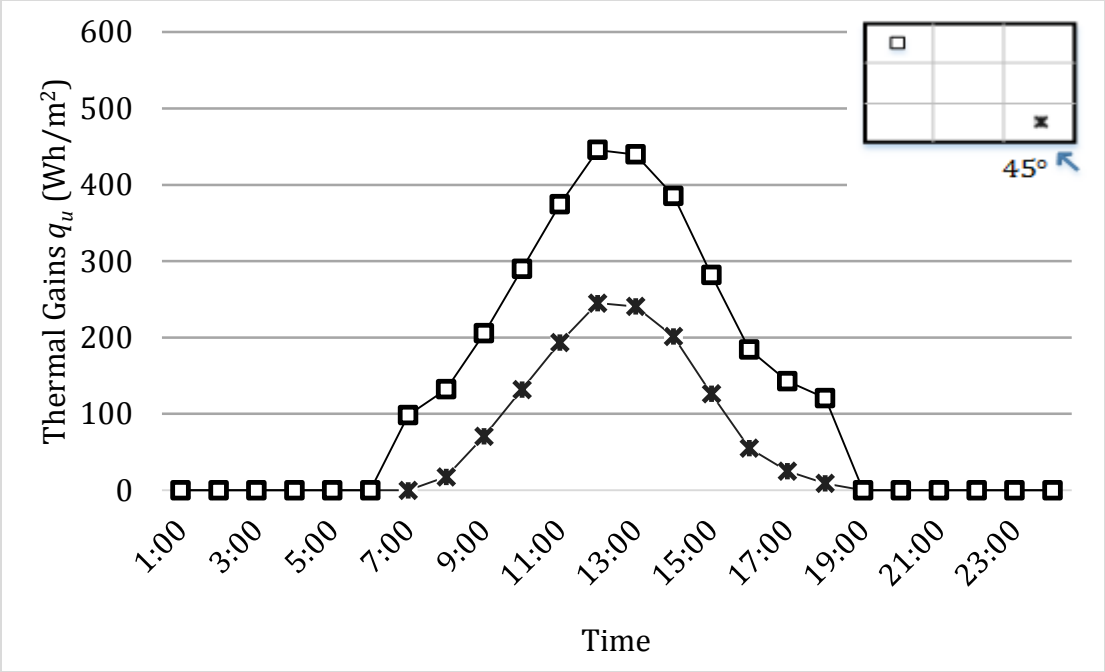

Figure 6.4: Thermal energy gains during a very windy day (Case 1 / 45°)

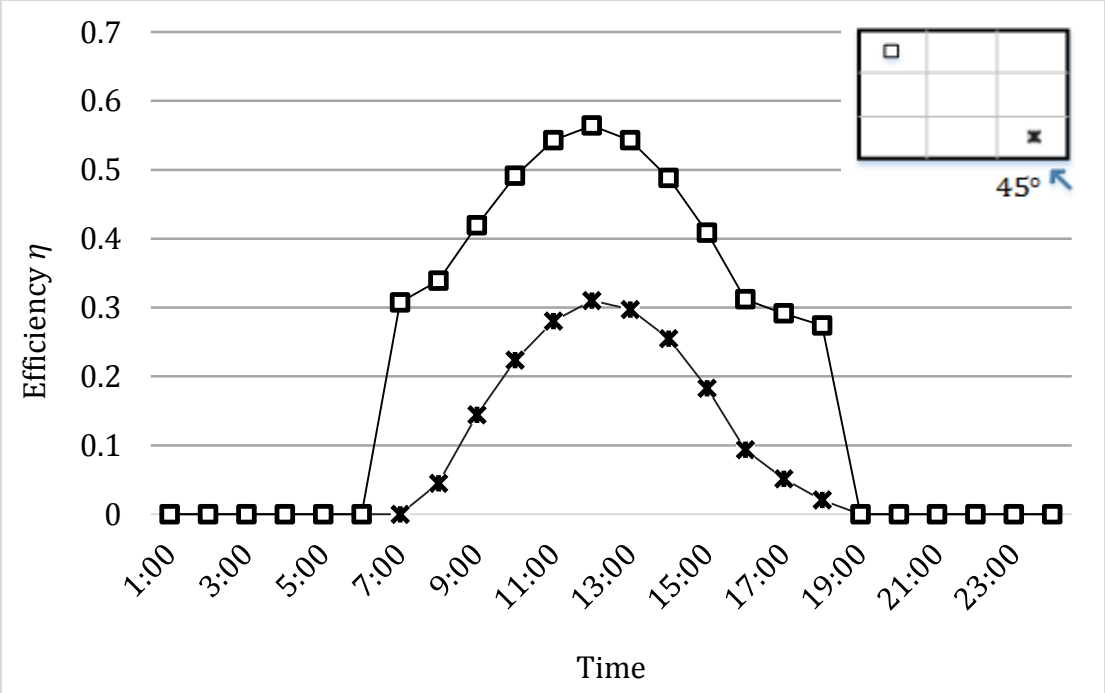

Figure 6.5: Solar collector efficiency during a very windy day (Case 1 / 45°)

Figure 6.6 shows the ratio of potential maximum over potential minimum daily thermal energy gains for a solar collector mounted above the roof of that specific building. The results are presented based on wind gradient velocity.

As the wind velocity decreases, the differences between locations are reduced. However, in the case of V_g = 30 m/s the difference is still significant. The ratio of maximum over minimum daily thermal energy gains (or efficiency) for a solar collector is 1.24 for 0° (and 1.28 for 45°) angle of attack. Even for V_g = 20 m/s the ratios are around 1.1. When the gradient velocities are of that magnitude, the velocities measured above the roof are those of a typical day in Montreal. Very similar differences were found for Case 2 (building height: 30 m).

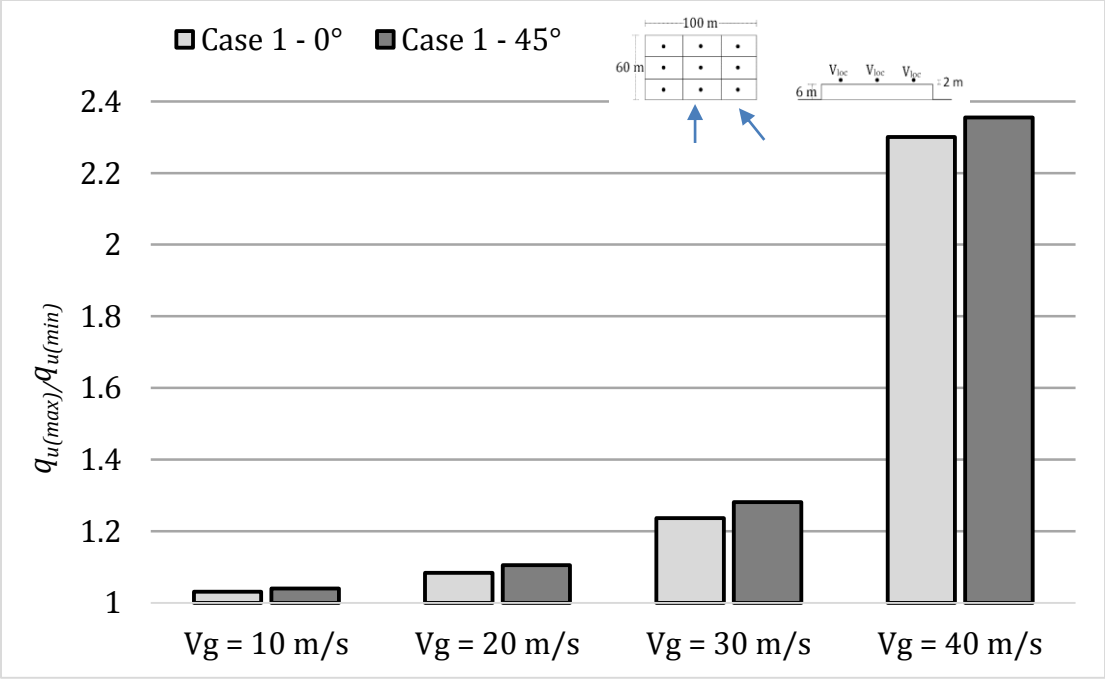

Figure 6.6: Ratio of maximum over minimum daily thermal energy gains on roof for an isolated building for two angles of attack, 0° and 45°

Figure 6.7 shows the ratio of maximum over minimum potential daily thermal energy gains for a solar collector mounted above the roof for cases with surrounding buildings. It is noticeable that the cases with the highest potential thermal energy differences are not all of the time the ones that showed the highest velocity differences between roof locations. This is more evident in the urban cases (Case 16 and 17) where the wind velocities above the roof were not big enough to create large differences in the thermal gains between roof locations. On the other hand, in Case 14, the wind velocities and their variances between roof locations, were both relatively high. This led to large differences in potential thermal energy gains.

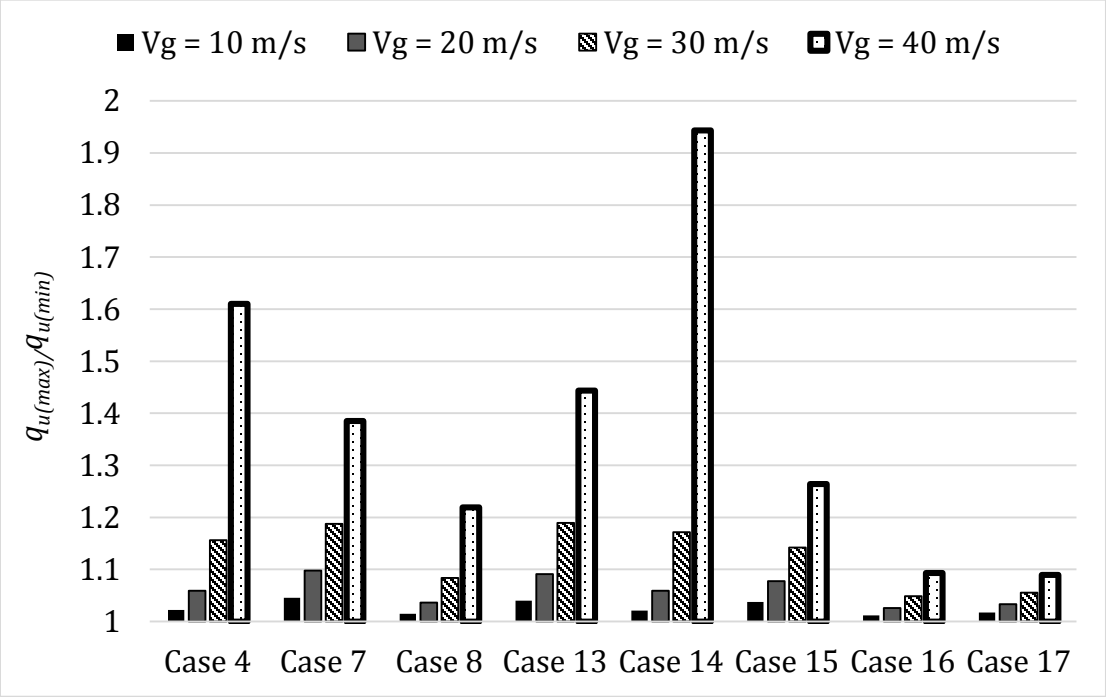

Figure 6.7: Ratio of maximum over minimum daily thermal energy gains on roof for cases with surrounding buildings

The potential energy differences of a solar collector, in different locations on a roof, are therefore enlarged in two situations: when velocities above the roof are high and when the differences between the locations are substantial.

It is of course understood that the conditions assumed so far for analysis purposes may not be realistic. For instance, the wind would not blow from the same direction throughout an entire day. If a typical day in Montreal is considered with different wind velocities and directions, taken from the hourly weather data found in Government of Canada (2013), the results will be different. Indeed, Figure 6.8 shows the thermal energy gains of a solar collector mounted at the best and worst locations of the roof during a typical sunny day in Montreal (September 18th, 2013). The wind velocities averaged between 4 m/s – 7 m/s during the day and the predominant wind direction was south and southwest. These wind velocities are near the statistical average of normal wind velocities of the year for Montreal, Canada. Appendix A2 includes a sample calculation for the thermal gains evaluated at 13:00 at location 6.

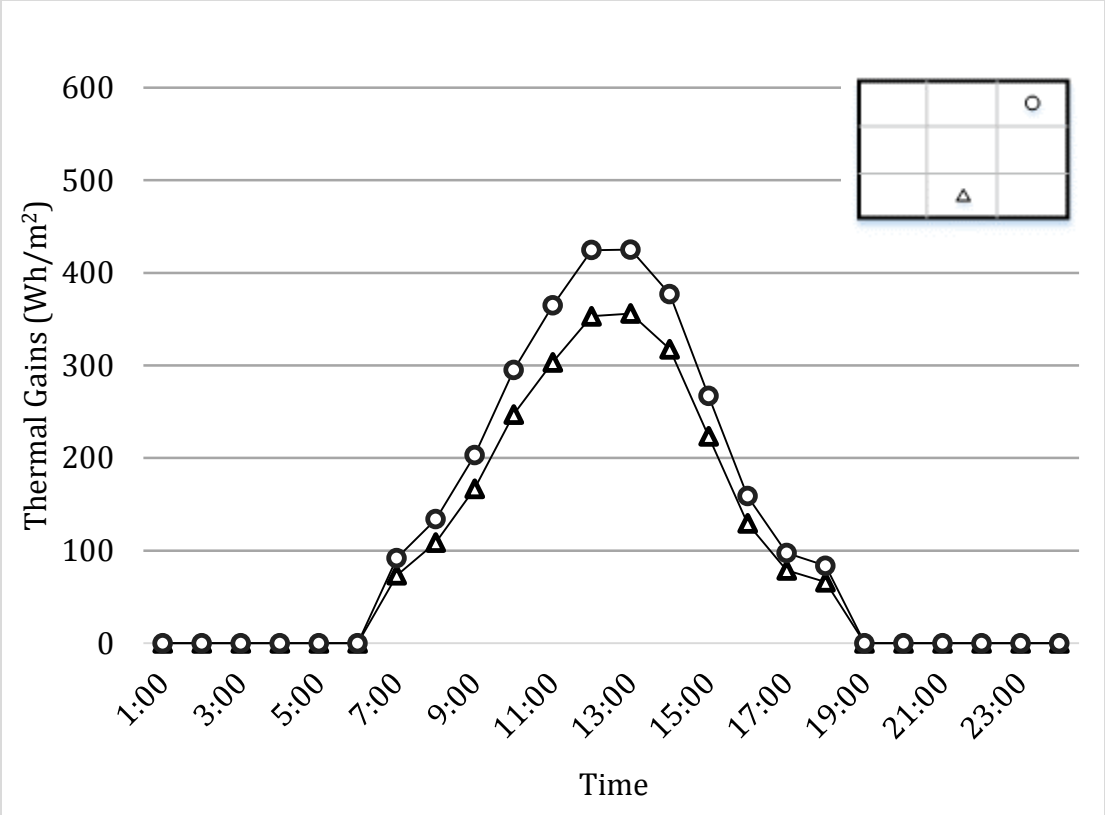

Figure 6.8: Thermal energy gains during a typical day -all wind directions-

The data shows that even for these regular conditions there is a significant difference in mounting a solar collector on different locations on the roof. More specifically, the ratio of maximum (location 6) over minimum (location 1) daily thermal energy gains (or efficiency) for a solar collector is 1.21.

6.3. *Practical Implications*

In this chapter, the thermal performance of a flat-plate solar collector installed in different locations above the roof of a building was simulated. As discussed previously, the most critical effect wind can have on a flat-plate solar collector is the removal of useful heat that leads to reduced thermal production. Wind has indeed various characteristics above different locations of a building roof. Results showed, that for a typical sunny day, the ratio of the thermal energy yield of the collector between the best and worst locations is 1.21. This is equivalent to 17% in energy differences between the critical installation locations.

Most research studies of the past that investigated the wind distribution on horizontal roofs, used "bluff bodies" with little or no obstruction to the flow. This is rarely the case in reality; wind velocity distributions are affected by the surroundings of the surface that is studied (i.e. the roof of the building in this study) and the upstream terrain conditions as well. Consequently, current correlations for wind-induced convective coefficients, although generally accepted for use with conditions comparable to those they were developed in, cannot be generalized. Because these correlations were created for very specific cases, it is prudent to use scaled models of the buildings and their surroundings when simulating the wind flow. This will allow for the engineer to have more accurate wind velocity data to examine the thermal gains of the solar collector.

Chapter 7 – CONCLUSIONS & RECOMMENDATIONS FOR FURTHER WORK

The purpose of this study was to highlight the significance of using actual wind velocity distributions, rather than a single velocity value, to study the performance of solar-thermal collectors mounted on building roofs. In previous studies, wind was not regarded as a critical parameter for the performance of solar collectors. However, this experimental study demonstrated that differences in wind velocities on various roof locations may be substantial and have an effect on the thermal performance of solar collectors. Convective heat losses may not be the most important parameter in a solar collector's performance; regardless, it was considered interesting to assess the wind-induced performance improvement of solar collectors by placing them on the most appropriate location on the roof.

Wind velocity distributions above the roof of a building model were measured experimentally in a wind tunnel. The measurements were performed under various wind angles of incidence, for an isolated building model and for fifteen additional configurations of adjacent buildings. The experimental results

were used for a parametric analysis utilizing a numerical model of a solar-thermal collector. The main conclusions of this study can be summarized as follows:

1. Measured wind velocity distributions on building roofs showed that local velocities in different parts of a roof can vary up to 62% due to flow phenomena that are driven by the geometry of the building and by its relative position to adjacent structures.
2. In the cases of isolated buildings, the experimental measurements revealed that local velocities are significantly higher (32% - 43%) at the windward parts of the roof. The 45° angle of attack was found to produce the largest differences with wind speeds at the windward side being up to 43% higher than the leeward side.
3. In the cases of a building with surrounding structures, the differences in local roof velocities can vary between 20% - 62%, while local flow patterns are governed by the geometry and relative location of neighbor buildings.
4. In general, the average wind velocities on the roof can be 45% - 55% lower for a building with surrounding structures when compared to an isolated building. Nevertheless, the existence of a very high building next to the building of interest can cause 20% - 30% higher winds on the rooftop compared to the isolated case, due to high suction near the ground level.
5. The wind-induced convective heat transfer coefficient was found to be an important parameter in the calculation of the thermal energy gains and thermal efficiency of a solar-thermal collector.

6. A numerical model of a roof mounted, water-based solar collector, utilizing energy balance equations, was used; for the case of an isolated building, it was estimated that the thermal energy gains are 17% higher in the windward areas compared to the leeward sections of the roof, during a typical sunny day.

Even though this study was performed on one particular building model, the results are anticipated to be relevant to similar buildings and similar conditions.

There have not been any studies in the past that aimed to develop location specific correlations between the performance of a solar collector on a building roof and local wind speeds. All existing studies and correlations were based on wind-induced convective coefficients measured in a single location above a roof.

In this study the effect of several different parameters was examined, however, more experimental work in the wind tunnel could offer the opportunity to investigate the effect of additional important factors. Some of these, could be the effect of the building shape (building geometry, pitched roofs etc.), the effect of much more surrounding buildings, as well as the effect of roughness of upstream exposure. It is expected that these issues will introduce additional variability and uncertainty in the results. Further investigation through full-scale and CFD modelling would also provide detailed insights into the wind effects on solar collectors on roofs.

REFERENCES

CISM (International Centre for Mechanical Sciences), 2007. Introduction to Wind Engineering, Wind Structure, Wind-Building Interaction. In: T. Stathopoulos & C. C. Baniotopoulos, eds. *Wind effects on buildings and design of wind-sensitive structures.* s.l.:Springer Wien New York, pp. 1-30.

Dalgliesh, W. A. & Boyd, D. W., 1962. *Wind on Buildings.* [Online] Available at: http://archive.nrc-cnrc.gc.ca/eng/ibp/irc/cbd/building-digest-28.html

Davenport, A. G., 1967. *The Dependence of Wind Loads on Meteorological Parameters.* Ottawa, University of Toronto Press, pp. 19-82.

Duffie, J. & Beckman, W., 2006. *Solar Engineering of Thermal Processes.* 3rd ed. New York: Wiley Interscience.

Emmel, M. G., Abadie, M. O. & Mendes, N., 2007. New External Convective Heat-Transfer Coefficient Correlations for Isolated Low-Rise Buildings. *Energy and Buildings,* Volume 39, pp. 335-342.

Gao, Y. & Chow, W. K., 2005. Numerical Studies on Air Flow Around a Cube. *Journal of Wind Engineering and Industrial Aerodynamics,* Volume 93, pp. 115-135.

Government of Canada, 2013. *Canadian Weather - Environment Canada.* [Online] Available at: http://climate.weather.gc.ca/ [Accessed 12 December 2013].

Hagishima, A. & Tanimoto, J., 2003. Field Measurements for Estimating the Convective Heat-Transfer Coefficient at Building Surfaces. *Building and Environment,* Volume 38, pp. 873-881.

IBPSA-USA, 2012. *Adjacent Buildings - Bembook,* s.l.: s.n.

Incropera, F. P. & deWitt, D. P., 1985. *Fundamentals of Heat and Mass Transfer.* New York: John Wiley and Sons.

Jetson Green, 2011. [Online] Available at: http://www.jetsongreen.com/2011/03/sunnovations-geyser-pump-solar-heating.html [Accessed 16 September 2013].

Jürges, W., 1924. Der Wärmeübergang an Einer Ebenen Wand. *Beihefte zum Gesundheits-Ingenieur,* pp. 1227-1249.

Kalogirou, S., 2004. Solar-Thermal Collectors and Applications. *Progress in Energy and Combustion Science,* Volume 30, pp. 231-295.

Karava, P., Jubayer, C. M. & Savory, E., 2011. Numerical Modelling of Forced Convective Heat Transfer from the Inclined Windward Woof of an Isolated Low-Rise Building with Application to Photovoltaic/Thermal Systems. *Applied Thermal Engineering,* Volume 31, pp. 1950-1963.

Kim, K. C., Ji, H. S. & Seong, S. H., 2003. Flow Structure Around a 3-D Rectangular Prism in a Turbulent Boundary Layer. *Journal of Wind Engineering and Industrial Aerodynamics,* Volume 91, p. 653–669.

Kind, R. J., Gladstone, D. H. & Moizer, A. D., 1983. Convective Heat Losses From Flat-Plate Solar Collectors in Turbulent Winds. *Transactions of the ASME, Journal of Solar Engineering,* February, Volume 105, pp. 80-85.

Klein, S. A., 1979. Calculation of Flat-Plate Loss Coefficients. *Solar Energy,* 17(79).

Kumar, S. & Mullick, S. C., 2010. Wind Heat-Transfer Coefficient in Solar Collectors in Outdoor Conditions. *Solar Energy,* Volume 84, pp. 956-963.

Kumar, S., Sharma, V. B., Kandpal, T. & Mullick, S. C., 1997. Wind-Induced Heat Losses from Outer Cover of Solar Collectors. *Renewable Energy,* 10(4), pp. 613-616.

Lim, H. & Castro, I. P., 2009. Flow Around a Cube in a Turbulent Boundary Layer: LES and Experiment. *Journal of Wind Engineering and Industrial Aerodynamics,* Volume 97, pp. 96-109.

McAdams, W., 1954. *Heat Transmission.* New York: McGraw Hill.

Morrison, G. L., Budihardjo, I. & Behnia, M., 2005. Measurement and Simulation of Flow Rate in a Water-in-Glass Evacuated-Tube Solar Water Heater. *Solar Energy,* Volume 78, pp. 257-267.

National Bureau of Standards, 1978. *Results and Analysis of a Round-Robin Test Program for Liquid-Heating Flat-Plate Solar Collectors,* Washington D.C., TN: s.n.

NovaLynx, 2013. *200-27005 Gill UVW Anemometer.* [Online] Available at: http://www.novalynx.com/pdf/200-27005.pdf [Accessed 17 July 2013].

NRCan, 2013. [Online] Available at: http://canmetenergy.nrcan.gc.ca/renewables/2449 [Accessed 07 May 2013].

REN21, 2012. *Renewables 2012 Global Status Report,* s.l.: s.n.

Rommel, M., Kovacs, P. & Kramer, K., 2010. Solar-Thermal Technologie Update. *Renewable Energy Focus,* pp. 36-38.

Sartori, E., 2006. Convection Coefficient for Forced Air Flow over Flat Surfaces. *Solar Energy,* Volume 80, pp. 1063-1071.

Shakerin, S., 1987. Wind-Related Heat-Transfer Coefficient for Flat-Plate Solar Collectors. *Transactions of the ASME, Journal of Solar Engineering,* May, Volume 109, pp. 108-110.

Sharples, S., 1984. Full-Scale Measurements of Convective Energy Losses from Exterior Building Surfaces. *Building and Environment,* 19(1), pp. 31-39.

Sharples, S. & Charlesworth, P. S., 1998. Full-Scale Measurements of Wind-Induced Convective Heat Transfer from a Roof-Mounted Flat-Plate Solar Collector. *Solar Energy,* 62(2), pp. 69-77.

Simiu, E., 1981. Modern Developments in Wind Engineering: Part 1. *Engineering Structures,* 3(4), pp. 233-241.

Solarworks, 2007. [Online]
Available at: http://www.solarworks.co.uk/category/type/pools/
[Accessed 19 February 2013].

Sparrow, E. M., Ramsey, J. W. & Mass, E. A., 1979. Effect of Finite Width on Heat Transfer and Fluid Flow about an Inclined Rectangular Plate. *Transactions of the ASME, Journal of Heat Transfer,* May, Volume 101, pp. 199-204.

Sparrow, E. M., Samie, F. & Lau, S. C., 1981. Heat Transfer from a Plate Elevated Above a Host Surface and Washed by a Separated Flow Induced by the Elevation Step. *Journal of Heat Transfer,* pp. 441-447.

Stathopoulos, T., 1984. Design and fabrication of a wind tunnel for building aerodynamics. *Journal of Wind Engineering and Industrial Aerodynamics,* Volume 16, pp. 361-376.

Sturrock, N. S., 1971. *Localised Boundary Layer Heat Transfer from External Building Surfaces. Ph.D. Thesis.* University of Liverpool: s.n.

Test, F. L., Lessmann, R. C. & Johary, A., 1981. Heat Transfer During Wind Flow over Rectangular Bodies in the Natural Environment. *Transactions of the ASME, Journal of Heat Transfer,* May, Volume 103, pp. 262-267.

U.S. Department of Energy, 2014. *EnergyPlus Energy Simulation Software.* [Online]
Available at: http://apps1.eere.energy.gov/buildings/energyplus/
[Accessed 02 December 2013].

Watmuff, J. H., Charters, W. W. S. & Proctor, D., 1977. Solar and Wind-induced External Coefficients for Solar Collectors. *Int. Revue d' Hellio-technique,* Volume 2, p. 56.

Woo, H. G. C., Peterka, J. A. & Cermak, J. E., 1977. *Wind Tunnel Measurements in the Wakes of Structrures,* s.l.: NASA Contractor Rep. NASA CR~2806.

Yakhot, A., Liu, H. & Nikitin, N., 2006. Turbulent Flow Around a Wall-Mounted Cube: A Direct Numerical Simulation. *International Journal of Heat and Fluid Flow,* Volume 27, pp. 994-1009.

APPENDIX A1

This Appendix includes contour plots of wind velocity coefficients (V_{loc}/V_g) for cases of section 4.4 not included in Chapter 5.

Case 3

V_{loc}/V_g

- *Test building height:* 6 m
- *Adjacent buildings height:* 30 m

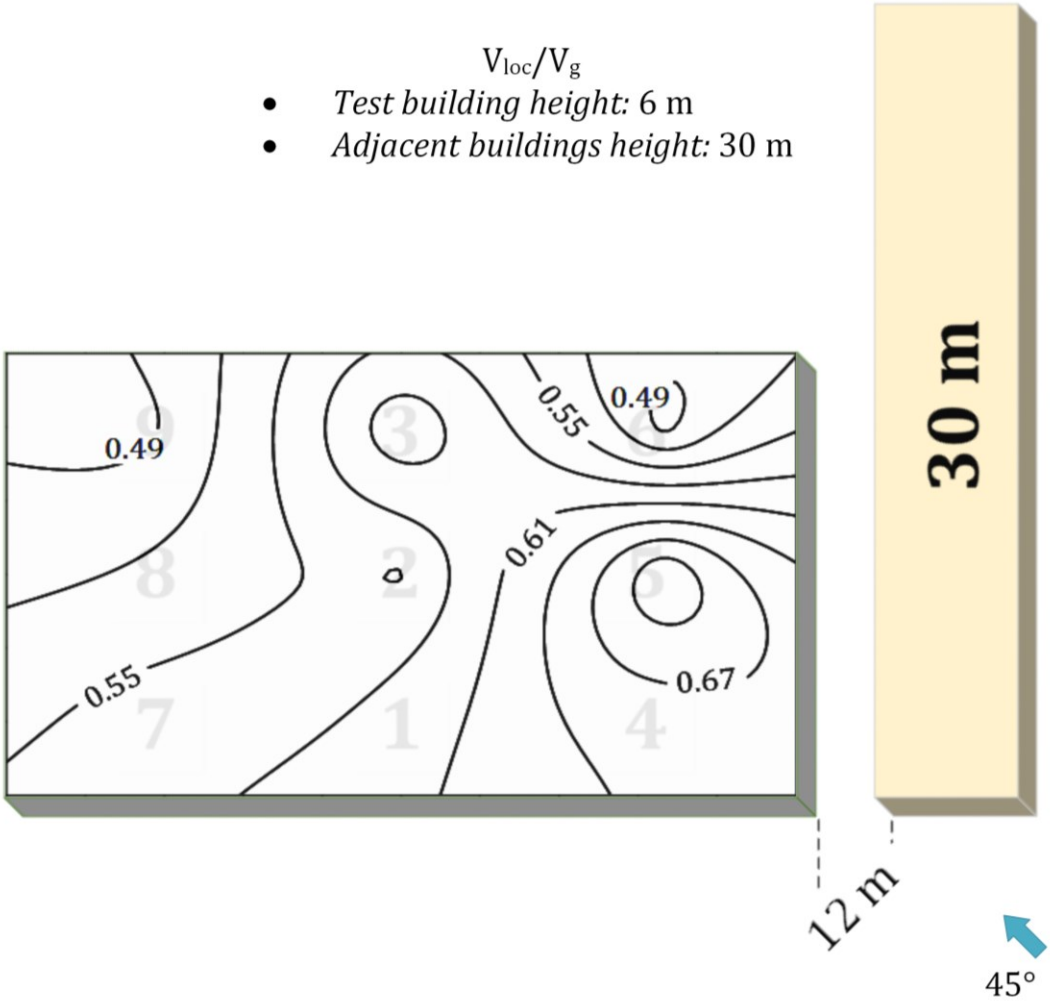

Case 4

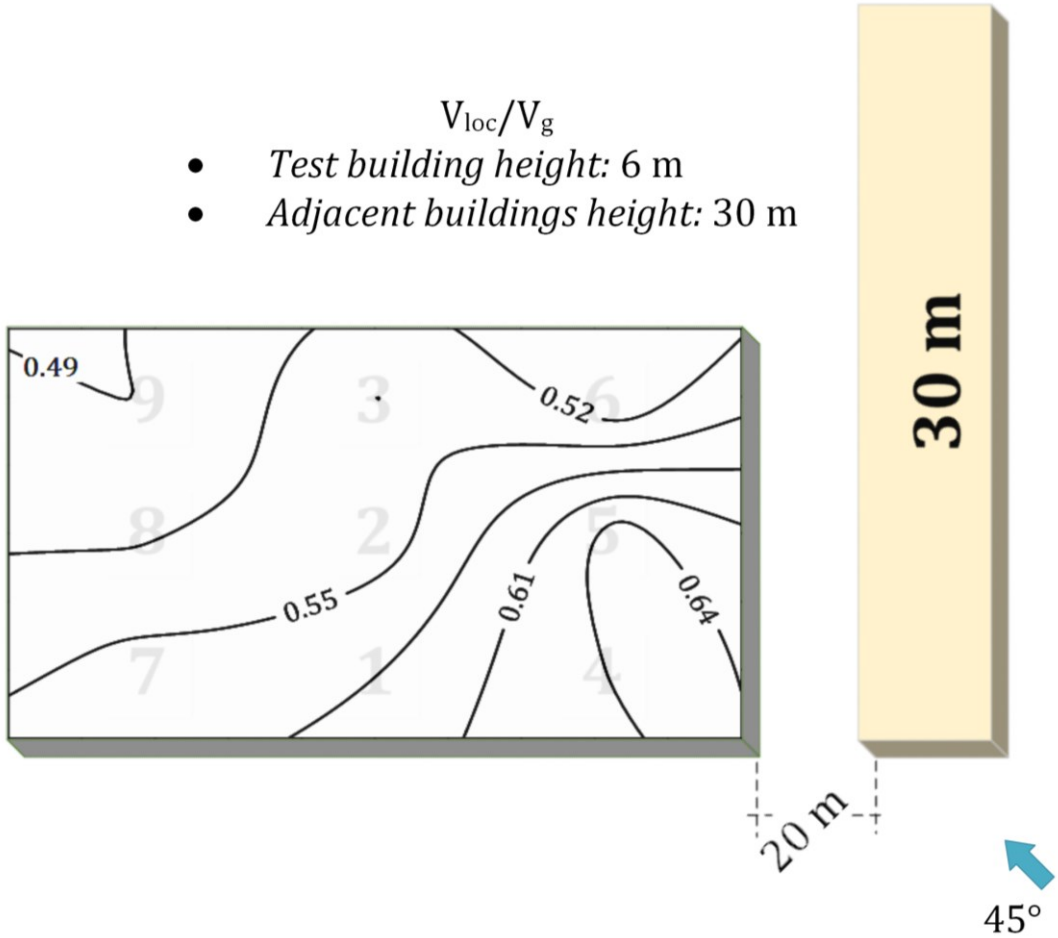
V_{loc}/V_g
• *Test building height:* 6 m
• *Adjacent buildings height:* 30 m
0.49
0.52
0.55
0.61
0.64
30 m
20 m
45°

Case 5

V_{loc}/V_g

- *Test building height:* 6 m
- *Adjacent buildings height:* 30 m

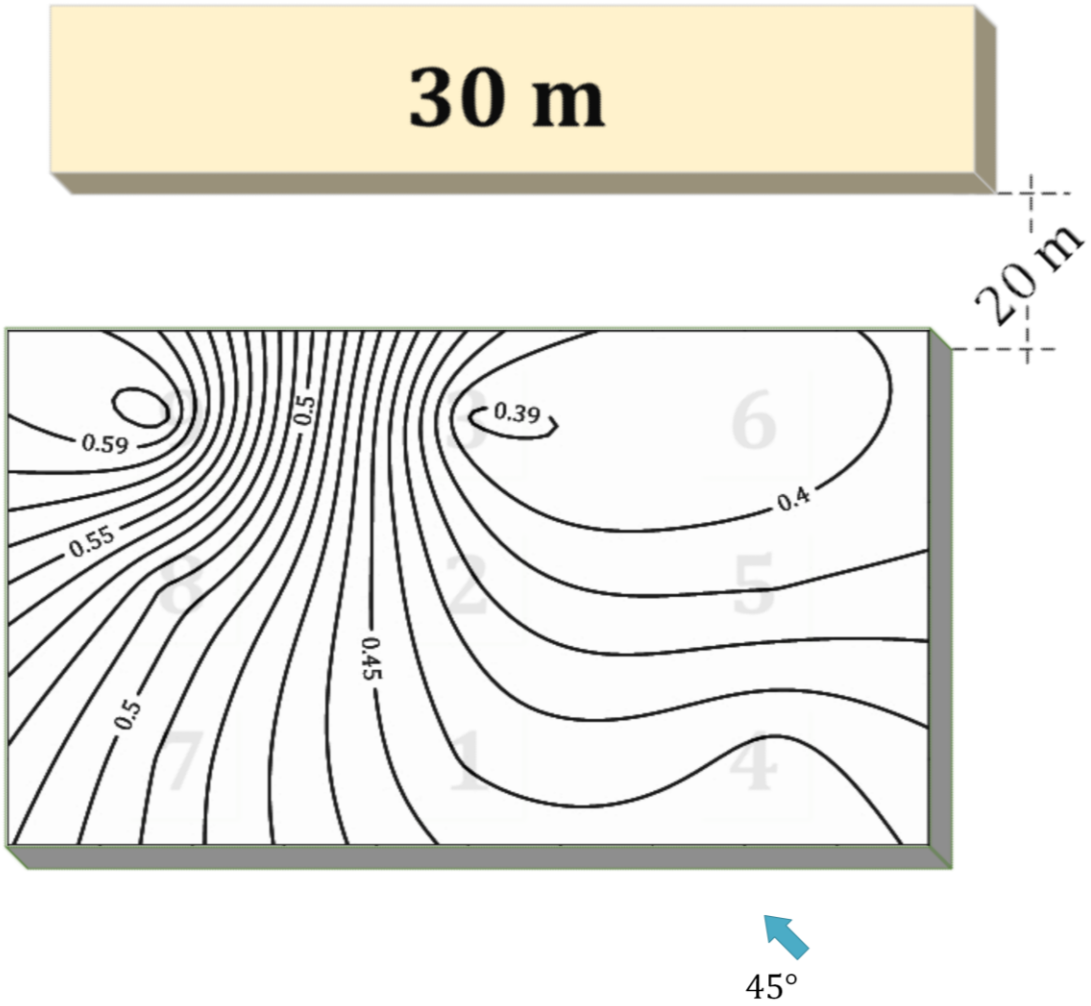

Case 6

V_{loc}/V_g

- *Test building height:* 6 m
- *Adjacent buildings height:* 30 m

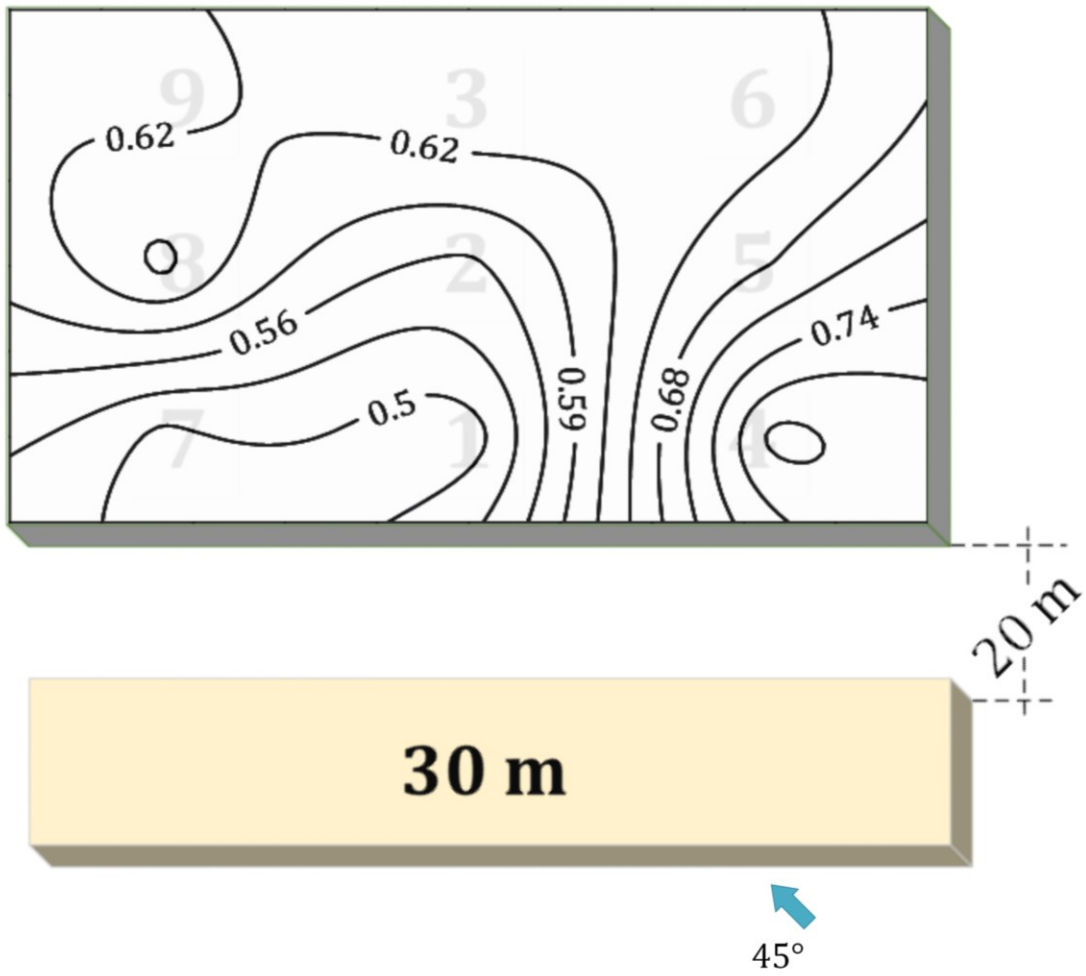

Case 8

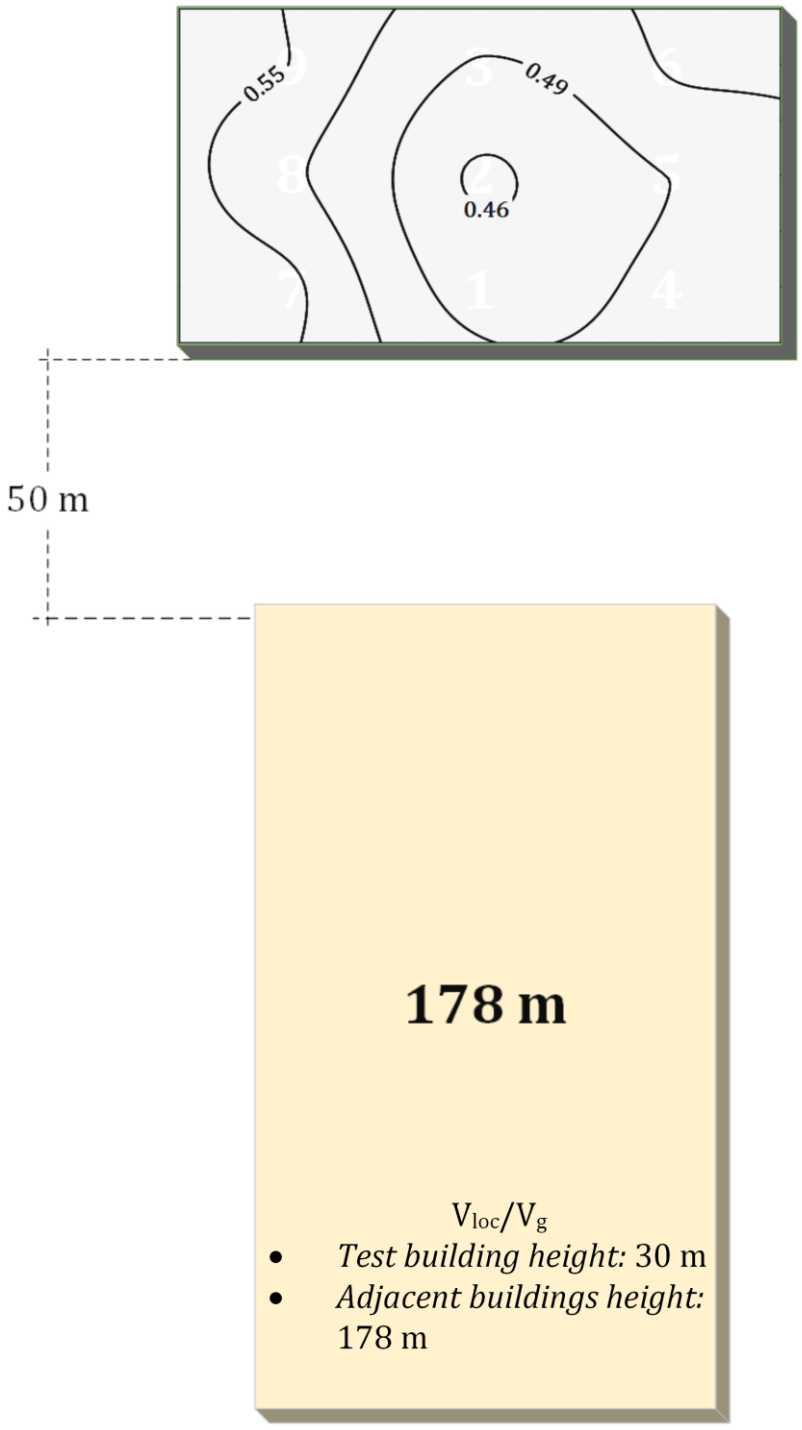
0.55
0.49
0.46
50 m
178 m
V_{loc}/V_g
• *Test building height:* 30 m
• *Adjacent buildings height:* 178 m
0°

Case 9

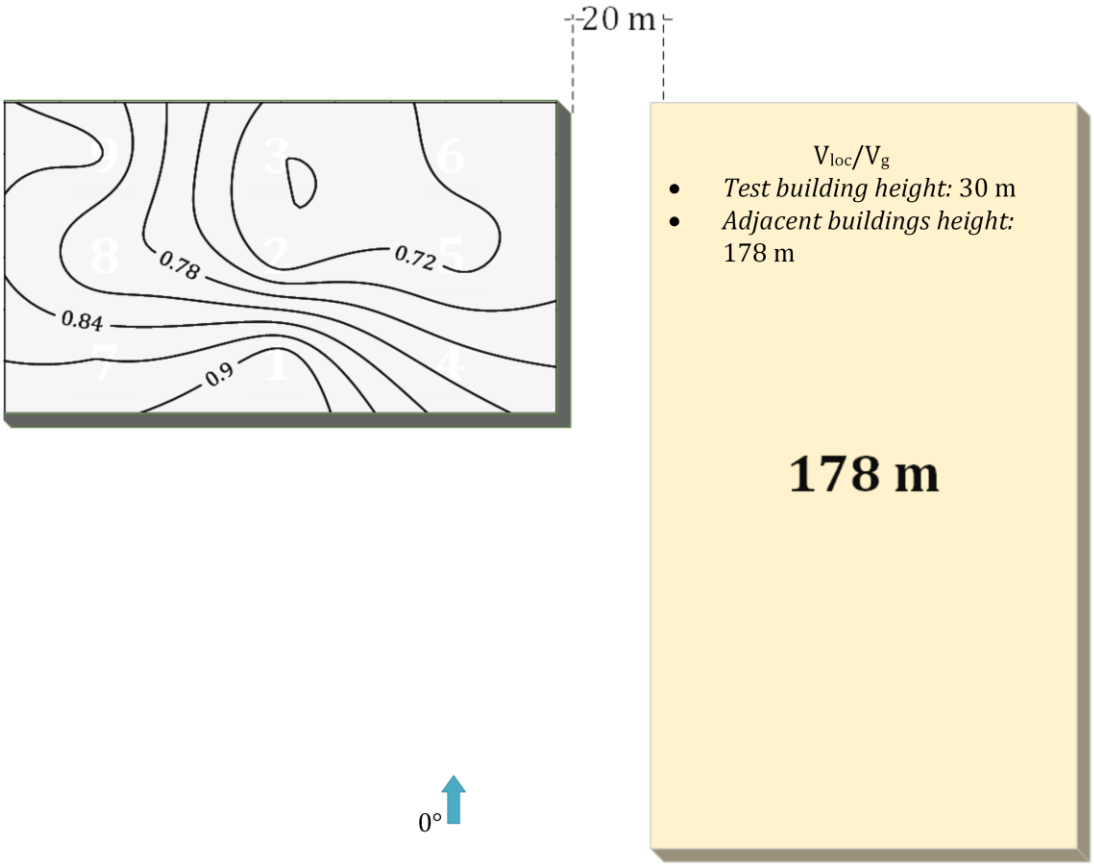
20 m
2
3
6
8
0.78
0.72
5
0.84
7
0.9
1
4
V_{loc}/V_g
• *Test building height:* 30 m
• *Adjacent buildings height:* 178 m
178 m
0°

Case 10

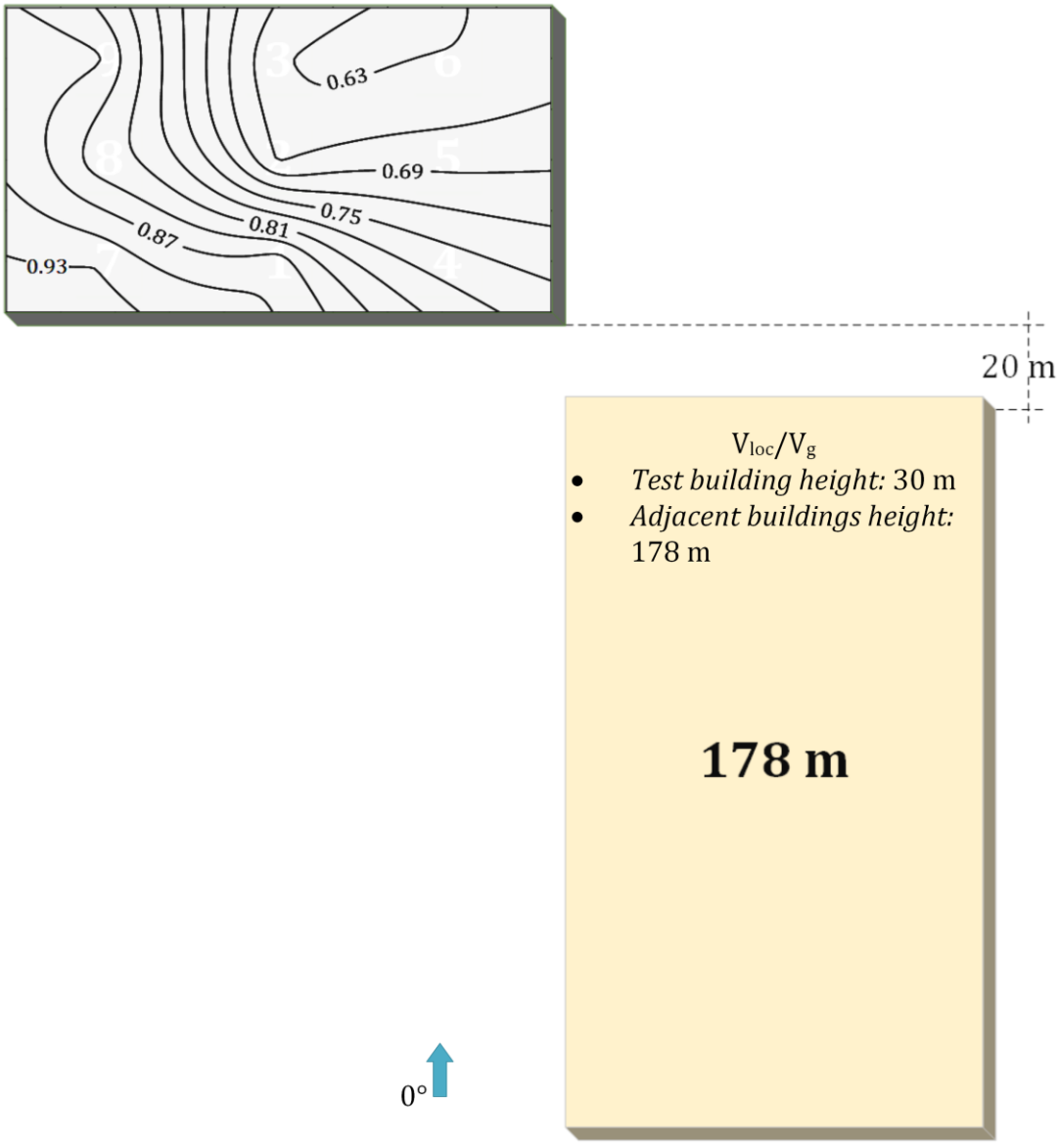
0.63
0.69
0.75
0.81
0.87
0.93
20 m
V_{loc}/V_g
• *Test building height:* 30 m
• *Adjacent buildings height:* 178 m
178 m
0°

Case 11

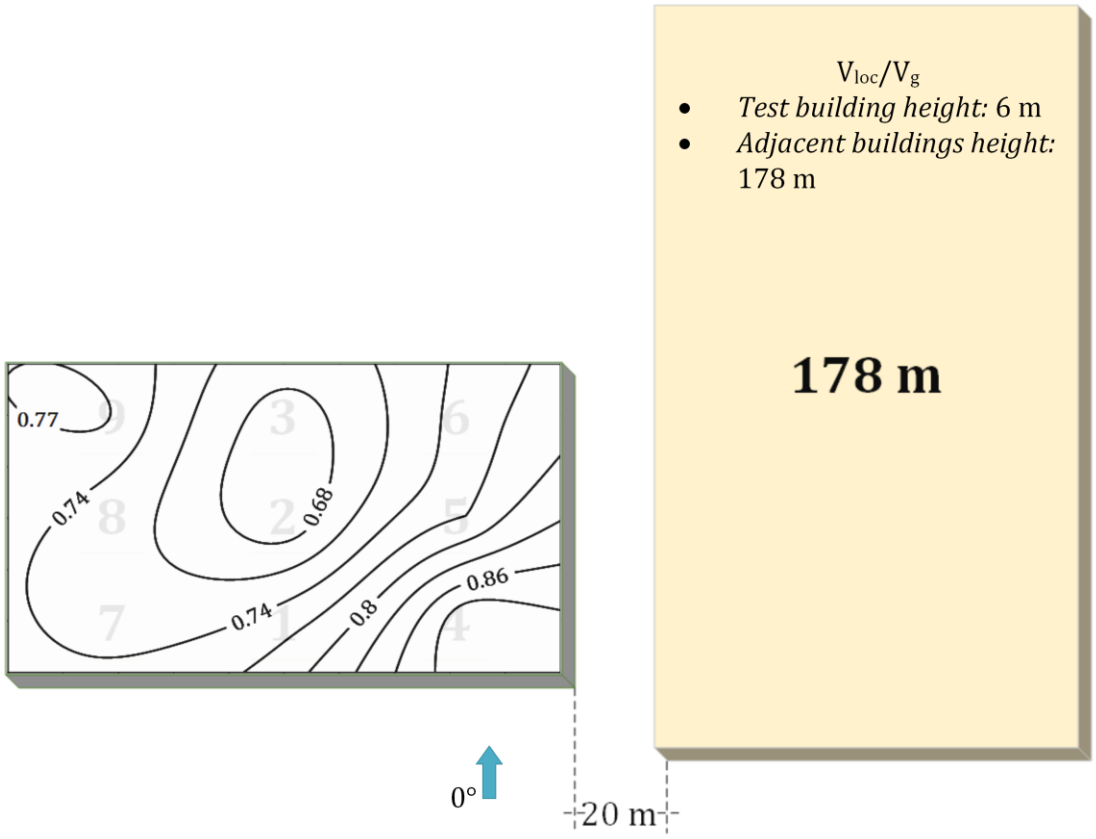
V_{loc}/V_g
Test building height: 6 m
Adjacent buildings height: 178 m
178 m
0.77
0.74
0.68
0.74
0.8
0.86
0°
20 m

Case 12

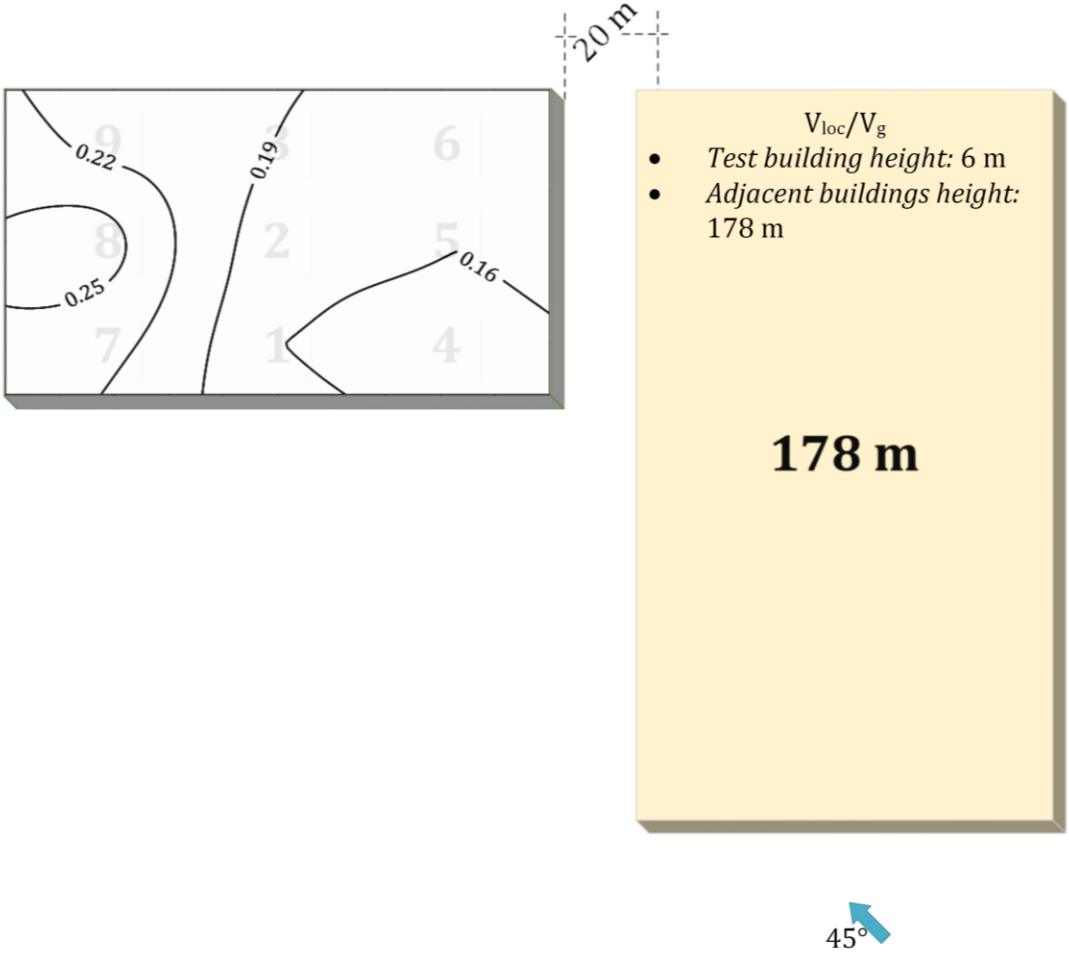
20 m
0.22
0.19
0.25
0.16
V_{loc}/V_g
• *Test building height:* 6 m
• *Adjacent buildings height:* 178 m
178 m
45°

Case 14

V_{loc}/V_g

- *Test building height:* 30 m
- *Adjacent buildings height:* 60 m & 90 m

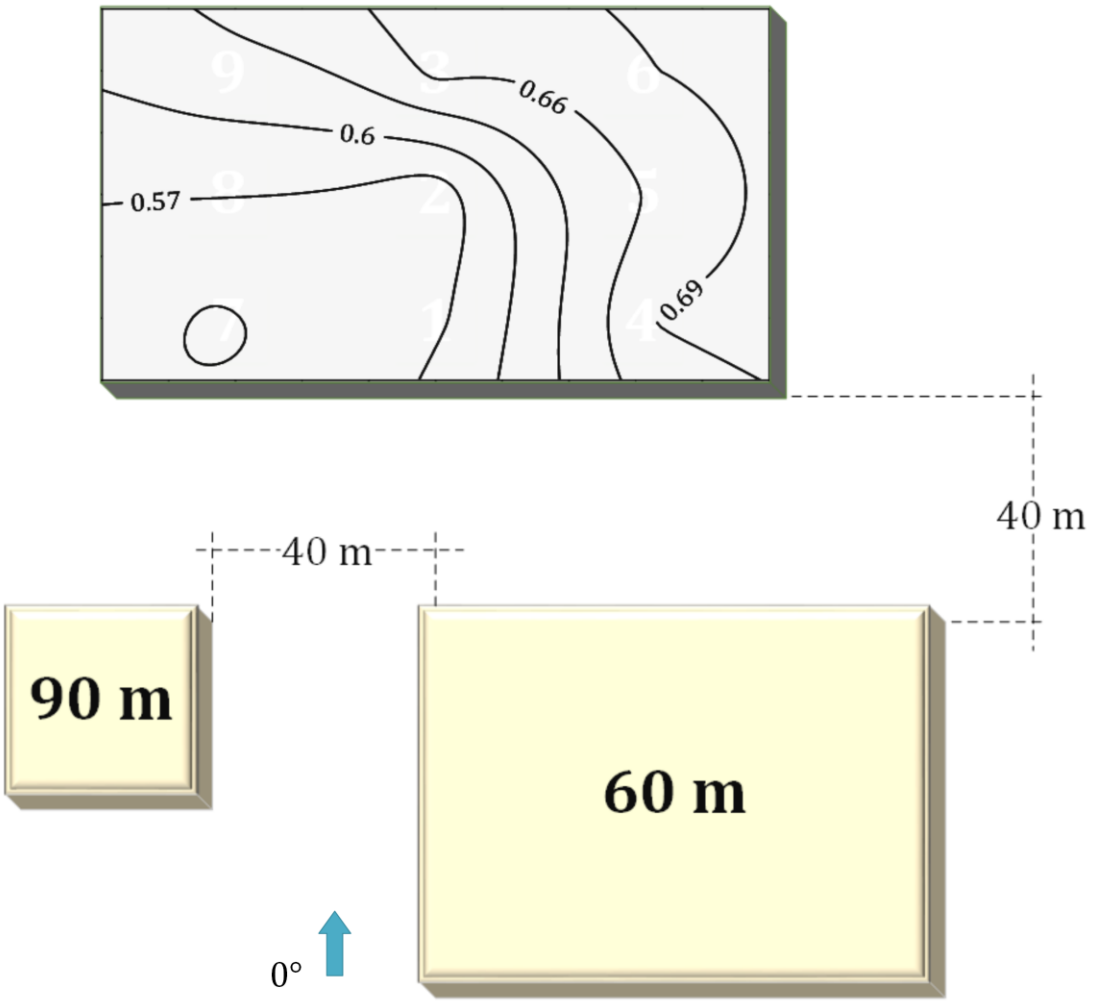

Case 16

V_{loc}/V_g

- *Test building height:* 30 m
- *Adjacent buildings height:* ~30 m (city center)

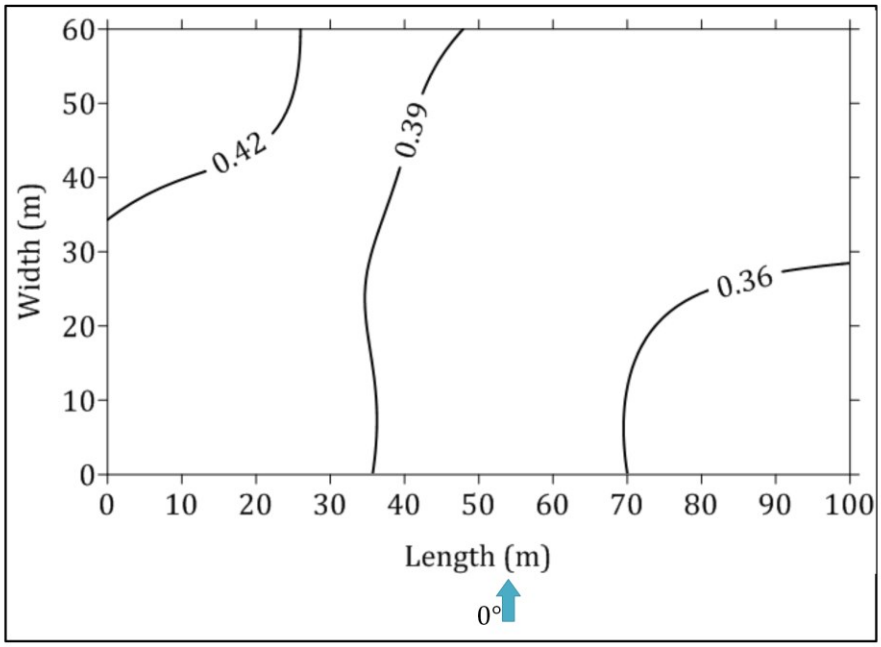

APPENDIX A2

This Appendix, introduced in section 6.2, includes a sample calculation of the thermal energy gains q_u of the flat-plate, single-glazed solar collector used in this study at 13:00 during a typical windy sunny day in Montreal. The collector was hypothetically located above location 6 of the model (Figure 4.5).

Velocity measured at Z = 10 m at the Montreal International Airport:

V_{10} = 44 km/h or 12.22 m/s

(*wind direction*: 0°)

(Ambient temperature:$T_a = 293.15\ K$)

Using the power law (equation (2-1)) the velocity at roof height (30 m) is measured:

V_{30} = 14.10 m/s

Also the gradient velocity at Z = 200 m is calculated:

V_g = 18.10 m/s

V_{30} is the velocity approaching the model. However, the velocity above each location on the roof is different as it was shown in the previous chapters. Based on the wind tunnel experiments that were conducted it was shown that wind velocity distributions vary based on different parameters such as the building geometry, the surroundings and the terrain.

The wind velocity above location 6 is the product of the dimensionless ratio V_{loc}/V_g measured at the wind tunnel (at location 6, for another gradient velocity V_g = 12.4 m/s), shown in Figure 5.1, and the actual gradient velocity V_g = 18.1 m/s:

$V_{loc(6)}$ = 8.54 m/s

Using equation (3-7) from Sharples & Charlesworth (1998) the wind-induced convective heat transfer coefficient is then calculated as:

$$h_w = 27.10 \text{ W/m}^2\text{K}$$

Now that h_w is calculated and the rest of the parameters are set in Table 6.1, the model of section 0 can be used to calculate the thermal energy gains q_u per collector area A_c as expressed in equation (6-1):

The overall-loss coefficient for a solar collector U_L is calculated from equation (6-3) as:

$$U_L = U_t + U_b + U_e$$

The top-loss coefficient U_t is calculated from equation (6-4) as:

$$U_t = 10.03$$

The bottom-loss coefficient U_b is calculated from equation (6-5) as:

$$U_b = 0.90$$

The edge-loss coefficient U_e is calculated from equation (6-6) as:

$$U_e = 0.46$$

Therefore, the overall-loss coefficient will be $\underline{U_L = 11.38}$

The heat removal factor is calculated is calculated from equation (6-7) as:

$$F_R = F'_c F''_c$$

The collector efficiency factor F'_c is calculated from equation (6-8) as:

$$F'_c = 0.79$$

The fin efficiency factor F_c, which is a variable in the F'_c equation, is calculated from equation (6-9) as:

$$F_c = 0.91$$

The collector flow factor F''_c is calculated from equation (6-10) as:

$$F''_c = 0.91$$

Therefore, the heat removal factor will be $\underline{F_R = 0.72}$

The solar energy S that is absorbed by the collector absorber plate is given by equation (6-11):

$$S = 707.41 \text{ W/m}^2$$

- Solar beam radiation: $I_b = 620 \ {}^{W}/_{m^2}$
- Solar diffuse radiation: $I_d = 170 \ {}^{W}/_{m^2}$
- Ground reflected solar radiation: $I_g = 20 \ {}^{W}/_{m^2}$

Finally, the thermal energy gains q_u per collector area A_c as expressed in equation (6-1) will be:

$$\underline{\underline{q_u = 425\ \mathrm{W/m^2}}}$$

This value is visible in Figure 6.8. All other values were calculated in a similar fashion.